

Thermal Conductivity of Hygroscopic Foams Based on Cellulose Nanomaterials

Varvara Apostolopoulou-Kalkavoura



Thermal Conductivity of Hygroscopic Foams Based on Cellulose Nanomaterials

Varvara Apostolopoulou-Kalkavoura

Academic dissertation for the Degree of Doctor of Philosophy in Materials Chemistry at Stockholm University to be publicly defended on Friday 26 March 2021 at 13.00 digitally via Zoom, public link will be made available at <https://www.mmk.su.se/>

Abstract

Biobased super-insulating materials could mitigate climate change by minimizing the use of petroleum-based materials, creating artificial carbon sinks and minimizing the energy needed to maintain pleasant interior conditions. Cellulose nanomaterials (CNM) produced from abundantly available cellulose sources constitute versatile, highly anisotropic raw materials with tunable surface chemistry and high strength. This thesis includes the evaluation of the thermal conductivity of isotropic and anisotropic CNM-based foams and aerogels and analysis of the dominant heat transfer mechanisms.

We have developed a customized measurement cell for hygroscopic materials in which the humidity and temperature are carefully controlled while the thermal conductivity is measured. Anisotropic cellulose nanofibrils (CNF) foams with varying diameters showed a super-insulating behavior perpendicular (radial) to the nanofibril direction, that depended non-linearly on the relative humidity (RH) and foam density. Molecular simulations revealed that the very low thermal conductivity is related to phonon scattering due to the increase of the inter-fibrillar gap with increasing RH that resulted in a 6-fold decrease of the thermal boundary conductance. The moisture-induced swelling exceeds the thermal conductivity increase due to water uptake at low and intermediate RH and resulted in a minimum thermal conductivity of $14 \text{ mW m}^{-1} \text{ K}^{-1}$ at 35% RH and 295 K for the foams based on the thinnest CNF.

The density-dependency of the thermal conductivity of cellulose nanocrystal (CNC) foams with densities of 25 to 129 kg m^{-3} was investigated and a volume-weighted modelling of the solid and gas thermal conductivity contributions suggested that phonon scattering was essential to explain the low radial thermal conductivity, whereas the replacement of air with water and the Knudsen effect related to the nanoporosity in the foam walls had a small effect. Intermediate-density CNC foams (34 kg m^{-3}) exhibited a radial thermal conductivity of $24 \text{ mW m}^{-1} \text{ K}^{-1}$ at 295 K and 20% RH , which is below the value for air.

The moisture uptake of foams based on CNMs with different degree of crystallinity and surface modifications decreased significantly with increasing crystallinity and temperature. Molecular simulations showed that the narrow pore size distribution of the amorphous cellulose film, and the relatively low water adsorption in the hydration cell around the oxygen of the carboxyl group play an important role for the moisture uptake of amorphous and crystalline CNM-based materials.

Isotropic CNF- and polyoxamer based foams as well as CNF-AL-MIL-53 (an aluminum-based metal-organic framework) foams were both moderately insulating ($>40 \text{ mW m}^{-1} \text{ K}^{-1}$) and comparable with commercial expanded polystyrene. The thermal conductivity of CNF and polyoxamer foams displayed a very strong RH dependency that was modelled with a modified Künzel's model. The presence of hydrophobic AL-MIL-53 decreased the moisture uptake of CNF-AL-MIL-53 aerogels by 42% compared to CNF-polyoxamer foams.

Solid and gas conduction are the main heat transfer mechanisms in hygroscopic nanofibrillar foams and aerogels that depend on the interfacial phonon scattering, Knudsen effect and water uptake. It is essential that the thermal conductivity measurements of hygroscopic CNM-based foams and aerogels are determined at controlled RH and that parameters such as the temperature, density, nanoporosity, fibril dimensions and alignment are characterized and controlled for systematic development and upscaling of biobased foams for applications in building insulation and packaging.

Keywords: *thermal conductivity, cellulose nanomaterials, foams, hygroscopic, super-insulating, phonon scattering, moisture uptake, heat transport.*

Stockholm 2021

<http://urn.kb.se/resolve?urn=urn:nbn:se:su:diva-190212>

ISBN 978-91-7911-406-0
ISBN 978-91-7911-407-7

Department of Materials and Environmental
Chemistry (MMK)

Stockholm University, 106 91 Stockholm



Stockholm
University

THERMAL CONDUCTIVITY OF HYGROSCOPIC FOAMS BASED
ON CELLULOSE NANOMATERIALS

Varvara Apostolopoulou-Kalkavoura

Thermal Conductivity of Hygroscopic Foams Based on Cellulose Nanomaterials

Varvara Apostolopoulou-Kalkavoura

©Varvara Apostolopoulou-Kalkavoura, Stockholm University 2021

ISBN print 978-91-7911-406-0

ISBN PDF 978-91-7911-407-7

The cover image is a photo of an igloo Church close to Kiruna taken by me in 2009.

Printed in Sweden by Universitetsservice US-AB, Stockholm 2021

To Harry, Panos, my
brother and my parents

Abstract

Biobased super-insulating materials could mitigate climate change by minimizing the use of petroleum-based materials, creating artificial carbon sinks and minimizing the energy needed to maintain pleasant interior conditions. Cellulose nanomaterials (CNM) produced from abundantly available cellulose sources constitute versatile, highly anisotropic raw materials with tunable surface chemistry and high strength. This thesis includes the evaluation of the thermal conductivity of isotropic and anisotropic CNM-based foams and aerogels and analysis of the dominant heat transfer mechanisms.

We have developed a customized measurement cell for hygroscopic materials in which the humidity and temperature are carefully controlled while the thermal conductivity is measured. Anisotropic cellulose nanofibrils (CNF) foams with varying diameters showed a super-insulating behavior perpendicular (radial) to the nanofibril direction, that depended non-linearly on the relative humidity (RH) and foam density. Molecular simulations revealed that the very low thermal conductivity is related to phonon scattering due to the increase of the inter-fibrillar gap with increasing RH that resulted in a 6-fold decrease of the thermal boundary conductance. The moisture-induced swelling exceeds the thermal conductivity increase due to water uptake at low and intermediate RH and resulted in a minimum thermal conductivity of $14 \text{ mW m}^{-1} \text{ K}^{-1}$ at 35% RH and 295 K for the foams based on the thinnest CNF.

The density-dependency of the thermal conductivity of cellulose nanocrystal (CNC) foams with densities of 25 to 129 kg m^{-3} was investigated and a volume-weighted modelling of the solid and gas thermal conductivity contributions suggested that phonon scattering was essential to explain the low radial thermal conductivity, whereas the replacement of air with water and the Knudsen effect related to the nanoporosity in the foam walls had a small effect. Intermediate-density CNC foams (34 kg m^{-3}) exhibited a radial thermal conductivity of $24 \text{ mW m}^{-1} \text{ K}^{-1}$ at 295 K and 20% RH , which is below the value for air.

The moisture uptake of foams based on CNMs with different degree of crystallinity and surface modifications decreased significantly with increasing crystallinity and temperature. Molecular simulations showed that the narrow

pore size distribution of the amorphous cellulose film, and the relatively low water adsorption in the hydration cell around the oxygen of the carboxyl group play an important role for the moisture uptake of amorphous and crystalline CNM-based materials.

Isotropic CNF- and polyoxamer based foams as well as CNF–AL-MIL-53 (an aluminum-based metal–organic framework) foams were both moderately insulating ($>40 \text{ mW m}^{-1} \text{ K}^{-1}$) and comparable with commercial expanded polystyrene. The thermal conductivity of CNF and polyoxamer foams displayed a very strong RH dependency that was modelled with a modified Künzel’s model. The presence of hydrophobic AL-MIL-53 decreased the moisture uptake of CNF–AL-MIL-53 aerogels by 42% compared to CNF-polyoxamer foams.

Solid and gas conduction are the main heat transfer mechanisms in hygroscopic nanofibrillar foams and aerogels that depend on the interfacial phonon scattering, Knudsen effect and water uptake. It is essential that the thermal conductivity measurements of hygroscopic CNM-based foams and aerogels are determined at controlled RH and that parameters such as the temperature, density, nanoporosity, fibril dimensions and alignment are characterized and controlled for systematic development and upscaling of biobased foams for applications in building insulation and packaging.

List of Publications

Publications included in the thesis

I. Humidity-Dependent Thermal Boundary Conductance Controls Heat Transport of Super-Insulating Nanofibrillar Foams

Varvara Apostolopoulou-Kalkavoura, Shiqian Hu, Nathalie Lavoine, Mohit Garg, Mathieu Linares, Pierre Munier, Igor Zozoulenko, Junichiro Shiomi, Lennart Bergström

Matter, **2021**, 4, 1-14

I participated in conceptualizing the research idea and planning of the study. I prepared the foams and performed the experiments and data analyses related to thermal conductivity, moisture uptake, DSC, AFM, nitrogen sorption and SEM. I participated in the experiments related to the TEMPO-mediated oxidation, aspect ratio sedimentation, XRD and conductometric titration. I did not perform the molecular simulations or HRSEM imaging. I wrote the first version of the manuscript and I wrote the final version with inputs from all authors.

II. Effect of Density, Phonon Scattering and Nanoporosity on the Thermal Conductivity of Anisotropic Cellulose Nanocrystal Foams

Varvara Apostolopoulou-Kalkavoura[†], Pierre Munier[†], Lukasz Dlugozima, Veit-Lorenz Heuthe and Lennart Bergström

Manuscript Submitted to *Scientific Reports* on 2021-02-18

I participated in conceptualizing the research idea and planning of the study. I performed the experiments and data analyses related to the thermal conductivity, moisture uptake and DSC. I performed the modelling. I participated in the preparation of the foams and the nitrogen sorption, SEM and AFM characterization. I did not perform the XRD or mechanical compression experiments. I co-wrote the first version of the manuscript and I co-wrote the final version with inputs from all authors.

III. Moisture Uptake in Nanocellulose: The Effect of Relative Humidity, Temperature and Degree of Crystallinity

[†] Indicates shared first authorship

Mohit Garg[†], Varvara Apostolopoulou-Kalkavoura[†], Mathieu Linares, Tahani Kaldéus, Eva Malmström, Lennart Bergström and Igor Zozoulenko
Manuscript Submitted to *Cellulose* on 2021-01-17

I participated in conceptualizing the research idea and planning of the study. I performed the experimental moisture uptake measurements and the related data analysis. I prepared and characterized the cellulose nanofibrils and cellulose nanocrystals. I did not perform the molecular simulations and I did not prepare the carboxymethylated cellulose nanofibrils. I wrote the part of the manuscript related to the experimental data and contributed to the finalization of the manuscript.

IV. Thermal Conductivity of Hygroscopic Foams Based on Cellulose Nanofibrils and a Nonionic Polyoxamer

Varvara Apostolopoulou-Kalkavoura, Korneliya Gordeyeva, Nathalie Lavoine and Lennart Bergström
Cellulose, **2018**, 25 (2), 1117–1126

I participated in conceptualizing the research idea and planning of the study. I performed the experiments related to thermal conductivity, moisture uptake, water vapor permeability, SEM and relevant data analyses. I participated in the experiments related to the AFM, conductometric titration and TEMPO-mediated oxidation. I did not prepare the CNF-polyoxamer foams. I wrote the first version of the manuscript and I wrote the final version with inputs from all authors.

V. Elastic Aerogels of Cellulose Nanofibers@Metal–Organic Frameworks for Thermal Insulation and Fire Retardancy

Shengyang Zhou, Varvara Apostolopoulou-Kalkavoura, Marcus Vinícius Tavares da Costa, Lennart Bergström, Maria Strømme, Chao Xu
Nano-Micro Letters, **2020**, 12 (1), 1–13

I performed the thermal conductivity experiments and related data analysis. I did not prepare the foams and I did not participate in the other characterization techniques. I wrote the corresponding manuscript part in the results and materials and methods, participated in scientific discussions and revised the final version of the manuscript.

VI. Thermally Insulating Nanocellulose-based Materials

Varvara Apostolopoulou-Kalkavoura, Pierre Munier, and Lennart Bergström
Advanced Materials, **2020**, 2001839, 1–17

[†] Indicates shared first authorship

I performed the majority of the literature review. I participated in the writing of the final version of the manuscript with a focus on sections 4 to 6, and I wrote the first version of all the sections. I did not design the Figures, but I participated in scientific discussions for designing them. I co-wrote and revised the manuscript.

Publications not included in the thesis

VII. Fire-retardant and Thermally Insulating Phenolic-silica Aerogels

Zhi-Long Yu, Ning Yang, Varvara Apostolopoulou-Kalkavoura, Bing Qin, Zhi-Yuan Ma, Wei-Yi Xing, Chan Qiao, Lennart Bergström, Markus Antonietti, Shu-Hong Yu

Angewandte Chemie, **2018**, 57 (17), 4538–4542

VIII. Analysis of the Porous Architecture and Properties of Anisotropic Nanocellulose Foams: a Novel Approach to Assess the Quality of Cellulose Nanofibrils (CNFs)

Konstantin Kriechbaum, Pierre Munier, Varvara Apostolopoulou-Kalkavoura, Nathalie Lavoine

ACS Sustainable Chemistry & Engineering, **2018**, 6 (9), 11959–11967

IX. Strong Silica-Nanocellulose Anisotropic Composite Foams Combine Low Thermal Conductivity and Low Moisture Uptake

Pierre Munier, Varvara Apostolopoulou-Kalkavoura, Michael Persson, Lennart Bergström

Cellulose, **2020**, 27, 10825–10836

X. Sclerotization-Inspired Aminoquinone Cross-Linking of Thermally Insulating and Moisture-Resilient Biobased Foams

Konstantin Kriechbaum, Varvara Apostolopoulou-Kalkavoura, Pierre Munier, and Lennart Bergström

ACS Sustainable Chemistry & Engineering, **2020**, 8 (47), 17408–17416

Contents

Abstract.....	i
List of Publications	iii
List of Abbreviations	1
1 Introduction.....	3
1.1 Heat Transfer within a Porous Material.....	3
1.1.1 Conduction.....	4
1.1.1.1 Solid Conduction.....	5
1.1.1.2 Gas Conduction	6
1.1.2 Convection.....	8
1.1.3 Radiation.....	8
1.2 Insulation Materials	9
1.3 Aerogels and Foams.....	10
1.3.1 Processing Routes to Obtain Porous CNM Foams and Aerogels	10
1.3.1.1 Supercritical Drying (SCD).....	11
1.3.1.2 Freeze-Drying (FD) and Freeze-Casting	11
1.3.1.3 Evaporative (Oven/Ambient) Drying (ED)	13
1.3.2 Thermal Conductivity of Aerogels and Foams	14
1.4 Thermal Conductivity Measurement Techniques: Benefits and Drawbacks	16
1.5 Cellulose: Structure and Intrinsic Anisotropy.....	17
1.5.1 Cellulose Nanomaterials (CNM)	18
1.5.2 Cellulose Nanofibrils (CNF).....	19
1.5.3 Cellulose Nanocrystals (CNC).....	20
1.6 Thermal Conductivity of Wood and Cellulose	20
1.7 Scope of the Thesis	22
2 Preparation of Materials.....	23
2.1 Preparation of Mechanically-ground CNF and TEMPO-mediated Oxidized CNF (TCNF).....	23
2.2 Preparation of CNC and TEMPO-mediated Oxidized CNC (TCNC)	25
2.3 Preparation of Carboxymethylated CNF (CMCNF).....	25

2.4	Preparation of the CNF@Al-MIL-53 Nanofibers	26
2.5	Preparation of Anisotropic Foams by Freeze-Casting	26
2.6	Preparation of Isotropic foams	26
3	Characterization of Dispersions and Foams	28
3.1	Thermal Conductivity	28
3.2	Differential Scanning Calorimetry (DSC)	31
3.3	Gravimetric Moisture Uptake	33
3.4	Water Vapor Permeability	34
3.5	Nitrogen Adsorption	34
3.6	Foam Density and Porosity	35
3.7	Scanning Electron Microscopy (SEM)	36
3.8	Conductometric Titration	38
3.9	Atomic Force Microscopy (AFM)	39
3.10	Other Characterization Techniques	40
3.10.1	Aspect Ratio by Sedimentation Experiments	40
3.10.2	X-ray Diffraction (XRD)	42
3.10.3	Mechanical Compression	43
4	Heat Transfer and Moisture Transport of Anisotropic CNM Foams (Papers I, II and III)	45
4.1	Thermal Conductivity of CNF Foams as a Function of the Fibril Diameter and RH (Paper I)	45
4.2	Moisture Uptake and Swelling of CNF and TCNF Foams (Paper I)	49
4.3	Thermal Boundary Conductance of CNM Materials (Paper I)	51
4.4	Density-dependent Thermal Conductivity of CNF Foams	53
4.5	Density-dependent Thermal Conductivity of CNC Foams (Paper II)	54
4.6	Moisture Uptake as a Function of RH, Temperature and Crystallinity (Paper III)	62
4.7	Conclusions	65
5	Thermal Conductivity of Isotropic Foams (Papers IV and V)	67
5.1	Thermal Conductivity and Moisture Transport Properties of Isotropic CNF-Nonionic Polyoxamer Foams (Paper IV)	67
5.2	Modelling of the Thermal Conductivity of Hygroscopic Foams (Paper IV)	69

5.3 Thermal Conductivity and Moisture Resistance of CNF and Al-MIL-53 Aerogels (Paper V)	71
5.4 Conclusions.....	73
6 Outlook (Paper VI)	75
Sammanfattning	77
Περίληψη	79
Acknowledgements.....	81
References.....	85

List of Abbreviations

AFM: Atomic Force Microscopy
BET: Brunauer–Emmett–Teller
CAM: Cellulose Nanofibrils – AL-MIL-53 aerogel
CI: Crystallinity Index
CNC: Cellulose Nanocrystals
CNF: Cellulose Nanofibrils
CMCNF: Carboxymethylated Cellulose Nanofibrils
CNM: Cellulose Nanomaterials
DSC: Differential Scanning Calorimetry
ED: Evaporative Drying
EPS: Expanded Polystyrene
FD: Freeze-Drying
HRSEM: High-resolution Scanning Electron Microscopy
MOF: Metal–Organic Framework
NEMD: Non-equilibrium Molecular Dynamics
RH: Relative Humidity
SCD: Supercritical Drying
SEM: Scanning Electron Microscopy
TBC: Thermal Boundary Conductance
TCNF: TEMPO Cellulose Nanofibrils
TCNC: TEMPO Cellulose Nanocrystals
TEMPO: 2,2,6,6-tetramethylpiperidine-1-oxyl radical
TPS: Transient Plane Source
VIP: Vacuum Insulation Panels
WVP: Water Vapor Permeability
XPS: Extruded Polystyrene
XRD: X-ray Diffraction

1 Introduction

The energy used to preserve a pleasant interior environment year round accounts for 30% of the total energy use in buildings (up to 50% in the cold countries) and 10% of global energy use, while CO₂ emissions from buildings (including construction) represent the 28% of global CO₂ emissions¹⁻⁴. CO₂ emissions associated with buildings are expected to rise even more as the increasing global population drives urbanization⁵. The depletion of fossil fuels due to their extensive use since the industrial revolution, as well as the increasing CO₂ emissions, demand that alternative biobased materials are developed for thermal insulation⁵. Buildings made of biobased materials can additionally act as human-made carbon sinks that contribute to mitigating climate change⁶. However, there are several challenges to consider while focusing on biobased materials such as their moisture sensitivity, their cost and their mechanical robustness⁷.

Thermal conductivity expresses the ability of a material to conduct heat. Materials with thermal conductivity below the conductivity of air (=25.7 mW m⁻¹ K⁻¹ at 295 K) are commonly described as super-insulating materials^{8,9}. To maintain a pleasant interior environment and simultaneously reduce the energy use for space heating and cooling, there is an imperative need to develop biobased insulation materials with low thermal conductivities. Furthermore, retrofitting old buildings require as well high-performance thermal insulation materials with super-insulating thermal conductivities to ensure that the living area is not significantly reduced^{9,10}.

1.1 Heat Transfer within a Porous Material

Porous materials are commonly used as insulation materials due to their very low density and high gas fraction which result in very low thermal conductivity. The effective thermal conductivity, λ_{eff} , of a porous material is usually described as a sum of conduction, convection and radiation contributions (Equation 1)^{8,11-15}.

$$\lambda_{eff} = \lambda_{cond} + \lambda_{conv} + \lambda_{rad} \quad (1)$$

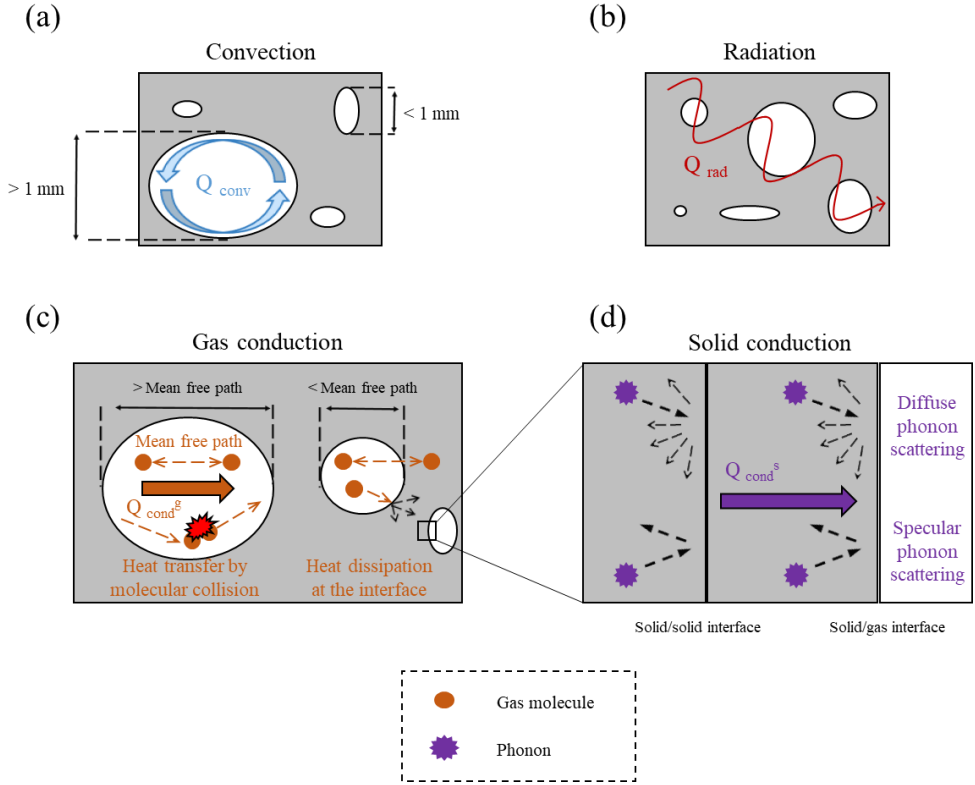


Figure 1. The modes of heat transport in porous materials. Heat transfer by: a) Convection; b) Radiation; c) Gas conduction, including the coupling effects at the gas–solid interface and d) Solid conduction, highlighting diffuse and specular phonon scattering at interfaces. Taken from Apostolopoulou et al. 2020¹⁶.

1.1.1 Conduction

The conductive heat flux, \vec{q} , through a material is generally described by Fourier's Law (Equation 2)^{17–19}.

$$\vec{q} = -\lambda \nabla T \quad (2)$$

where λ is the material's thermal conductivity and ∇T is the temperature gradient. The conduction contribution to thermal conductivity is then classified into solid (λ_s) and gas (λ_g) contributions.

1.1.1.1 Solid Conduction

Heat in solids is transferred by electrons, mostly in metals, and phonons, predominantly in insulators and semiconductors²⁰. Phonons are defined as energy quanta that cause atomic lattice vibrations^{20–22}. Stronger bonds (i.e. covalent) favor heat transfer and phonon propagation more than weaker ones (i.e. hydrogen bonds, van der Waals interactions)^{21,23–26}. There is no universal equation to calculate the contribution of thermal solid conduction to thermal conductivity; however, one way is to apply the basic kinetic theory (Equation 3)^{18,22,24,27–29}.

$$\lambda_{s,o} = \frac{1}{3} C_V v l \quad (3)$$

where C_V is the specific heat capacity at constant volume, v is the velocity of phonons which equals the speed of sound and l is the phonon mean free path. The mean free path of phonons is not always easy or possible to estimate, especially in systems with defects. There have been numerous computational attempts to improve the kinetic theory by incorporating defects, interfaces, grain boundaries or bonding strength^{22,28}.

To determine the solid thermal conductivity in a porous material, several studies have used a variety of geometrical or density-related approaches^{11,12,15,30,31}, as well as approaches that take into consideration the sound velocity through the porous material (Equation 4)^{28,32}.

$$\lambda_s = \lambda_{s,0} \frac{\rho_a}{\rho_{s,0}} \frac{v_a}{v_{s,0}} \quad (4)$$

where $\lambda_{s,0}$ is the bulk solid thermal conductivity, ρ_a is the aerogel density, $\rho_{s,0}$ is the bulk density, v_a is the speed of sound in the aerogel and $v_{s,0}$ is the speed of sound in the solid.

Nanomaterials, consisting of nanosized particles, usually have a high number of interfaces which can serve as phonon scattering points^{22,30,33–35}. When phonons meet a boundary or an interface, they are either transmitted or scattered, the latter as specular or diffuse scattering^{24,33}. Diffuse scattering significantly influences heat flow, resulting in a lower thermal conductivity compared to specular scattering incidents. Diffuse phonon scattering due to a higher number of interfaces and grain boundaries is enhanced in nanomaterials compared to their bulk equivalent, resulting in higher interfacial thermal resistance and lower thermal conductivity^{22,30,33–35}. In porous nanostructured

materials, solid conduction can be minimized not only because of phonon scattering at the solid–solid interfaces but also at the solid–gas interfaces^{27,30,36}. Specifically, Coquard et al. showed that, in materials having pores smaller than the phonon mean free path, diffuse phonon scattering at the solid boundary is significantly enhanced³⁷.

The Kapitza resistance (Equation 5),^{22,38–40} which stands for the inverse of the conductance, represents the resistance between grain boundaries and interfaces in a material. The influence of interfaces on the solid conductance can be expressed as:

$$\lambda_s = \frac{\lambda_{s,0}}{1 + \lambda_{s,0} \frac{R_K}{d}} \quad (5)$$

where $\lambda_{s,0}$ is the bulk solid thermal conductivity, d is the particle size and R_K is the Kapitza resistance. Interfaces between two different solid materials with large differences in the phonon velocity and density can result in large Kapitza resistances³³.

To determine the solid conduction contribution of a porous material experimentally, one can measure the effective thermal conductivity under vacuum and low temperature, to minimize both the gaseous and radiative heat transfer contributions²⁸. Coquard et al., for instance, performed Monte Carlo simulations to predict the solid thermal conductivity contribution of an open Kelvin cell model of a porous insulation material based on a cellulosic matrix in vacuum³⁷.

1.1.1.2 Gas Conduction

The gas conduction is mainly described by collisions between gas molecules and it is usually the main contribution (more than 60%) to the effective thermal conductivity of porous materials due to their high gas fraction^{14,41}. The main parameter influencing the gas conduction in a porous material is the pore size. The pore size controls the occurrence and frequency of the molecular collisions observing the so-called Knudsen effect for nanosized pores, usually below 50 nm. The mean free path of air molecules is bigger than the pore size which significantly reduces the molecular collisions between the gas particles and therefore the gaseous thermal conductivity contribution. The Knudsen diffusion then occurs as the particles are more

likely to collide with the foam or aerogel walls than with each other^{42,43}. In general, having a porous material with small pores can both reduce the gaseous thermal conductivity contribution due to the Knudsen⁴³ effect, and lead to lower solid conduction contribution³⁷. Xie et al. prepared a graphene aerogel which exhibited a thermal conductivity of 5–6 mW m⁻¹ K⁻¹ at room temperature under vacuum due to extensive phonon scattering within the graphene flakes and between them, even though graphene is a very good conductor³⁶. One way to determine the gaseous thermal conductivity contribution experimentally is to subtract the effective thermal conductivity under vacuum from the effective thermal conductivity under ambient pressure conditions^{14,28}. The most common equation^{15,31,38,44–46} used to calculate the gaseous thermal conductivity was first developed by Kaganer et al.⁴⁷ and later extended by Zeng et al.⁴³ (Equation 6) to consider the specific surface area and the aerogel density.

$$\lambda_g = \frac{\lambda_{g,0}}{1+2\beta Kn} \quad (6)$$

where $\lambda_{g,0}$ is the thermal conductivity of air in free space, β is a characteristic number equal to 2 for foams and aerogels, and Kn is the Knudsen number. The Knudsen number is the mean free path (Equation 7) of air molecules divided by the pore size⁴³.

$$I = \frac{1}{\sqrt{2} \times \frac{P \times \pi \times d_g^2}{k_B \times T} + \frac{S \times \rho}{\Pi}} \quad (7)$$

where P is the pressure, d_g is the diameter of a gas molecule, k_B is Boltzmann's constant, T is the temperature, S is the specific surface area, ρ is the density of the porous material and Π is the porosity. However, there are several recent studies which discuss the addition of one parameter to the gaseous conduction contribution, called the solid–gas coupling effects^{14,28,46,48}. The solid–gas coupling effects represent the molecular collisions occurring at the solid–gas interface and are dependent on the solid particle size as well as the pore size, and there have been attempts calculate their contribution^{14,28}.

1.1.2 Convection

Convection is the natural or forced movement of a fluid which transports heat according to the fluid's own velocity⁴⁹. During natural convection, buoyancy forces caused by temperature differences and thermal expansion are the main driving forces of the fluid's motion. For forced convection, an external force is always required⁵⁰. The Nusselt number expresses the ratio between the convective and the conductive heat transfer contributions and has a value of 1 when only conduction occurs in the system (Equation 8)^{50,51}.

$$Nu_L = \frac{hL}{\lambda_g} \quad (8)$$

where h is the Nusselt number, L is the characteristic length and λ_g is the gas conduction contribution to thermal conductivity. However, in porous materials used for thermal insulation, the pore size is usually below the convective threshold of 1–4 mm, resulting in negligible convection^{12,14,30}.

1.1.3 Radiation

The radiation contribution to thermal conductivity depends on the experimental temperature, as well as on the thickness, density, and pore size of the tested material¹¹. The most common equation used in the literature includes a dependence on the ambient temperature to the third power (Equation 9) confirming that at low temperatures the radiative heat transfer becomes negligible.

$$\lambda_{rad} = \frac{16\sigma T^3}{3E_R} \quad (9)$$

where σ is the Stefan–Boltzmann constant, T is the temperature and E_R is the Rosseland mean extinction coefficient. Obori et al. constructed a parametric open-pore model for CNF aerogels which described very well the experimental thermal conductivity for 0.3–1.4 v/v% solid CNF content³⁰. The model showed that the radiative heat transfer was comparable to or even higher than the solid conduction contribution at solid CNF concentrations below 0.6 wt%, while the gaseous heat transfer was the highest of all three. Under vacuum, the radiation contribution increased due to heat preferably travelling through the solid. However, at ambient temperature and pressure

conditions and as the solid content increased up to 1.4 wt% the radiation contribution was significantly lower since it varied linearly with T^3 ³⁷ and is more dominant under vacuum¹⁴.

1.2 Insulation Materials

Polyurethane and polystyrene are fossil-based thermal insulation materials that are extensively used in buildings⁵². Polyurethane foams are produced by a reaction between isocyanates and polyols and filled with an expansion gas (i.e. hydrofluorocarbon, CO₂ or C₆H₁₂), and usually exhibit thermal conductivities between 20 and 30 mW m⁻¹ K⁻¹⁵²⁻⁵⁴. Expanded (EPS) and extruded (XPS) polystyrene are made from small polystyrene spheres and melted polystyrene, respectively. Both EPS and XPS exhibit thermal conductivities usually between 30 and 40 mW m⁻¹ K⁻¹ and sometimes up to 45 mW m⁻¹ K⁻¹ for high-density insulation materials^{52,55}. Both polyurethane and polystyrene are hydrophobic, exhibiting good thermal insulation performance even at high moisture conditions^{52,54,56}. Specifically, the thermal conductivity of EPS with density of 16.5 kg m⁻³ increases from 37 to 51 mW m⁻¹ K⁻¹ from dry to moisture-saturated conditions⁵⁶.

Other common insulation materials used today include mineral wool, wood chips, and cork, which exhibit higher thermal conductivities and moisture sensitivities than polyurethane and polystyrene^{52,56}. The thermal conductivity for instance of mineral wool escalates significantly at high moisture contents, reaching even the high thermal conductivity value of 900 mW m⁻¹ K⁻¹ at moisture-saturated conditions, which is 24 times greater than the value at dry conditions (=37 mW m⁻¹ K⁻¹)⁵⁶. Wood-derived insulation materials, such as wood chips and cellulose fibers, that are usually used in cavities are well-known hygroscopic materials as well, having thermal conductivities above 40 mW m⁻¹ K⁻¹^{52,57}.

The most recent development in the field of thermal insulation materials for buildings is the vacuum insulation panels (VIP) made of several metallized polymer laminate films entrapping fumed silica^{7,57,58}. The thermal conductivity of VIP can be as low as 3–4 mW m⁻¹ K⁻¹ but it degrades gradually with time due to air diffusion within the layers. Furthermore, the installation of such materials is difficult, and it can impose irreversible damage

to the VIP, which can result in significantly higher thermal conductivity. The high cost and the difficulty to handle and install the VIP makes them challenging and unattractive to use⁷. Other materials are the phase-change materials, which provide a thermal insulation capacity via cycles of endothermic and exothermic melting and solidification. The phase change materials are rather uncommon, and they have to be adjusted according to the specific climatic conditions and temperature ranges⁷.

1.3 Aerogels and Foams

In the literature there is a confusion between the definition of foams and aerogels. Lavoine et al. suggested that lightweight porous materials should be called aerogels if the pore size is less than 50 nm and foams if the pore size is larger than 50 nm⁵⁹. However, the terms in literature are used many times interchangeably which makes it difficult to compare different studies.

1.3.1 Processing Routes to Obtain Porous CNM Foams and Aerogels

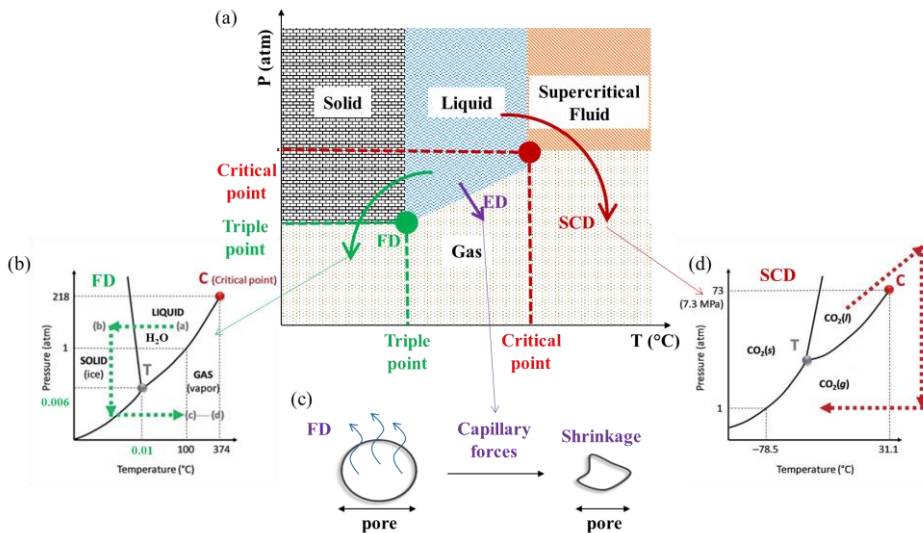


Figure 2. Common processing routes to obtain porous foams and aerogels. (a) Sketch of freeze-drying (FD), evaporative drying (ED) and supercritical

drying (SCD). (b) Phase diagram of water, the most common solvent used for sublimation. (c) Capillary forces during ED induce structural shrinkage. (d) Phase diagram of CO₂, the most common supercritical fluid used. (b) and (d) are adapted from Lavoine and Bergström, 2017⁶¹.

The method used to remove the solvent from a dispersion to obtain a solid foam or aerogel defines the final structure. The most common ways to produce solid foams and aerogels (Figure 2a-d) are supercritical drying (SCD), freeze-drying (FD) and evaporative drying (ED) (oven/ambient)^{8,60}. To produce isotropic aerogels and foams, SCD, FD or ED have been used, whereas anisotropic aerogels are mostly produced by freeze-casting and FD.

1.3.1.1 Supercritical Drying (SCD)

During SCD (Figure 2a), the solvent (usually water) is substituted by a supercritical fluid to minimise the capillary pressure-induced stresses, present at a liquid/vapor interface, during the solvent removal, as these can lead to the collapse of the porous structure^{8,59,60}. Carbon dioxide (CO₂) constitutes the most common supercritical fluid (Figure 2d) used due to the low and accessible temperature and pressure conditions (31.3 °C and 72.9 atm). In most cases, an intermediate solvent exchange to ethanol is required as the supercritical fluid is immiscible with the original solvent. Some disadvantages of supercritical drying include its high cost and energy use, as well as its complexity. However, using SCD usually results in aerogels with small pore sizes (mesopore range, 2–50 nm), which reduces significantly the gaseous thermal conductivity contribution due to the Knudsen effect^{8,62–64}.

1.3.1.2 Freeze-Drying (FD) and Freeze-Casting

The most common way to prepare solid foams and aerogels, especially from cellulose/CNF-based dispersions, is by FD^{62,65–70}. FD involves the sublimation of the frozen solvent which is usually water (Figure 2b). The sublimation reduces the capillary forces by inhibiting the formation of a liquid/vapor interface^{8,59,60,70}. The freezing and solidification of a dispersion is

typically done by immersion in cold medium such as liquid nitrogen (Figure 3a). The rapid freezing includes homogenous freezing of the dispersion from all sides keeping the original dispersion structure intact, resulting in materials with 3D pore structure.

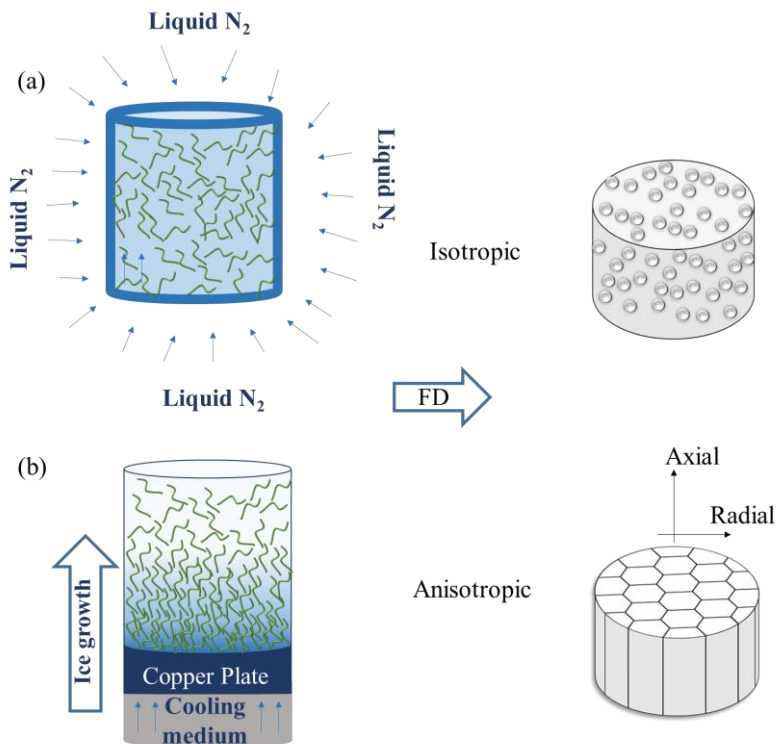


Figure 3. Freeze-drying of foams and aerogels. (a) Graphic illustration of homogeneous freezing resulting in isotropic structures. (b) Graphic illustration of unidirectional freezing resulting in anisotropic structures modified from Apostolopoulou-Kalkavoura et al., 2021⁷¹.

Instead of rapid solidification, one can use freeze-casting (Figure 3b) or ice-templating to slow-freeze the dispersions. In freeze-casting, the dispersion is unidirectionally frozen, which allows the ice growth to push the solid particles along the direction of the temperature gradient, yielding anisotropic structures with a honeycomb of tubular pores. The process conditions such as the freezing temperature and cooling rate determine the foam structure as well

as the pore size, with the latter being smaller as the cooling rate increases^{59,70}. Therefore, depending on the process conditions, it is possible to obtain aerogels with small pore sizes (<50 nm) or foams with larger pore sizes and even hierarchical pore structures (at least two main pore length scales; i.e. mesopores and macropores). One advantage of the freeze-casting compared to rapid solidification is that the final porous structure is reproducible by controlling the process conditions, making it an excellent foam production procedure both in lab but also in industrial scale⁵⁹. However, freezing and freeze-drying are expensive and energy consuming, though less complex than SCD as no solvent exchange cycles are required.

1.3.1.3 Evaporative (Oven/Ambient) Drying (ED)

Compared to SCD and FD, ED in an oven or under ambient conditions is potentially a less expensive and energy-intensive route to solid porous materials. The main limiting factor of ED is that capillary-induced deformation (Figure 2c), cracks or even collapse of the porous structure can occur during evaporation of the solvent; these issues are greatly inhibited during SCD and FD. Therefore, the wet foam needs to have a robust structure which will withstand capillary forces, avoiding collapse. The most common ways to prepare wet foams include vigorous stirring, shaking, pouring, sparging or desorption in order to introduce gas bubbles in a dispersion^{72–74}. To avoid the coalescence of the gas bubbles several compounds are used to stabilize the air–solvent interface such as surfactants or particles (i.e. Pickering foams)^{59,75–77}. Other ways to reduce cracking, shrinkage and collapse during evaporative drying are to allow crosslinking between the solid particles, use a solvent other than water (i.e. ethanol) or to modify the particle surfaces^{59,64,75,78,79}. Apart from the high shrinkage risk during ED, the need for foam stabilization might entail a long process including the extensive use of chemicals, thus reducing the renewability and environmentally friendly character of for instance a cellulose/CNM foam. Furthermore, due to capillary forces, the pore sizes of the materials obtained by ED are larger than those obtained by SCD or FD, resulting in higher gaseous conduction contribution to, and overall higher, effective thermal conductivity. The solid conduction contribution is also enhanced in case of stronger bonding due to crosslinking, increasing once again the effective thermal conductivity.

1.3.2 Thermal Conductivity of Aerogels and Foams

Aerogels are a promising class of low-thermal-conductivity materials. The lowest thermal conductivity has been so far observed for isotropic silica aerogels, which can exhibit values as low as $12\text{--}15\text{ mW m}^{-1}\text{ K}^{-1}$ under ambient conditions^{8,9}. Silica aerogels usually display mesopores, minimizing the gaseous thermal conduction contribution significantly. However, silica aerogels are in general brittle, difficult to apply, and expensive; therefore they are not widely used despite their extraordinary thermal properties⁸. In numerous studies, cellulose or CNMs have been added to silica aerogels in order to reduce their brittleness while maintaining their monolithic shape^{64,78,80–86}. In most of those studies the thermal conductivity of the final aerogels remained lower than that of air, or the so-called super-insulating level. However, it is worth noting that the temperature (T) and RH conditions are not always mentioned or controlled, making it difficult to compare the studies.

Interestingly, freeze-dried isotropic hybrid silylated silica/CNF aerogels with a CNF content of less than 10 wt% and a density of 130 kg m^{-3} displayed a thermal conductivity as low as $13.8\text{ mW m}^{-1}\text{ K}^{-1}$, which was only $1\text{--}2\text{ mW m}^{-1}\text{ K}^{-1}$ larger than the silica-only aerogel⁸⁶. It is worth noting that isotropic silica aerogels reinforced with 15 wt% short cellulose fibers exhibited thermal a conductivity of $15\text{--}16\text{ mW m}^{-1}\text{ K}^{-1}$ after supercritical drying and $17\text{ mW m}^{-1}\text{ K}^{-1}$ after ED ambiently, whereas the pure silica aerogel had a thermal conductivity of $14\text{ mW m}^{-1}\text{ K}^{-1}$ ^{64,78}.

During the past decade, there have been many attempts to prepare cellulose-only/CNM aerogels and foams, as cellulose offers great potential in the thermal insulation field due to its low thermal conductivity, low density, tunable surface chemistry and renewability. The best-performing isotropic aerogels or foams are made from TEMPO-oxidized CNF (TCNF) and have been reported by Kobayashi et al.⁶³, Sakai et al.⁶², Jiménez-Saelices et al.⁸⁷ and Chen et al.⁸⁸ Kobayashi et al.⁶³ prepared aerogels by SCD, whereas Sakai et al.⁶² prepared both aerogels by SCD and foams by FD, and Jiménez-Saelices et al.⁸⁷ used only FD, achieving a thermal conductivity as low as $18\text{ mW m}^{-1}\text{ K}^{-1}$ at $295\text{--}296\text{ K}$ and $50\%\text{ RH}$. Chen et al. prepared aerogels by FD and reported a thermal conductivity of $16\text{ mW m}^{-1}\text{ K}^{-1}$, but at unspecified measurement conditions which makes it hard to compare this study with the

others⁸⁸. All these high-performing aerogels had a 3D porous network with mostly small nanosized pores, while the foams had closed micro-sized pores.

Furthermore, some studies have investigated the effect of mixing various CNMs and cellulose fibers⁶⁵ or adding other non-cellulosic components^{68,77} in the CNF/cellulose aerogels or foams. For instance, Pickering TCNF–hexadecane (20 kg/m³ at 295 and 50% *RH*) and CNF–10% nanozeolite aerogels exhibited thermal conductivities of 18 mW m⁻¹ K⁻¹, the same value as for the best-performing TCNF-only aerogels. Furthermore, a multiscale study mixed CNF with bleached cellulose fibers, achieving a thermal conductivity as low as 22 mW m⁻¹ K⁻¹.

Wicklein et al. and Kriechbaum et al. reported the lowest radial (perpendicular to the fiber direction) thermal conductivities for anisotropic CNF- and TCNF-only foams respectively, which were as low as 18 mW m⁻¹ K⁻¹ while the corresponding axial (along the fiber direction) value was as high as 150 mW m⁻¹ K⁻¹ at 296 K and 50% *RH*^{38,89}. Interestingly, Wicklein et al. also prepared also composites of TCNF, graphene oxide (GO), boric acid (BA) and sepiolite (SEP), which exhibited a radial thermal conductivity of 15 mW m⁻¹ K⁻¹ and an axial one of 170 mW m⁻¹ K⁻¹³⁸. Furthermore, Li et al. prepared anisotropic nanowood and the radial thermal conductivity dropped from 107 mW m⁻¹ K⁻¹ for basswood to 32 mW m⁻¹ K⁻¹ for nanowood and the axial dropped from 347 mW m⁻¹ K⁻¹ for basswood to 56 mW m⁻¹ K⁻¹ for nanowood at 298 K and 20% *RH*⁹⁰.

The major challenge for the future market of thermal insulation materials is then to keep the low super-insulating thermal conductivities of silica aerogels but also to reduce the cost and increase the robustness of the future aerogels^{8,52}. Despite the recent developments in the field of thermal insulation and the studies on cellulose and CNMs, most of the studies disregard the effect of moisture on the thermal conductivity and fail to accurately report the experimental conditions used for the measurements. As cellulose is highly hygroscopic, it is crucial to investigate the impact of moisture uptake on the thermal insulation performance. Furthermore, comparing the variations in thermal conductivity between studies, there is a need to understand the heat transfer mechanism and the parameters which play important roles in tuning and controlling thermal transport both on the nano- and the macroscales.

1.4 Thermal Conductivity Measurement Techniques: Benefits and Drawbacks

Thermal conductivity can be experimentally measured either by steady-state or transient techniques⁹¹. The steady-state techniques require a large steady-state temperature gradient and measure heat flow across a sample of known thickness^{18,49,92,93}. The guarded hot plate (Figure 4a)^{10,28,46,56,81,86,94–98} and the heat flow meter apparatus^{30,64,78,80,83,84,99–101} are both steady-state techniques that are commonly used to determine the thermal conductivity of thermally insulating materials. The steady-state techniques are very accurate and require simple experimental calculations but obtaining a steady-state temperature gradient across the sample requires a long wait. Furthermore, large samples are usually required and the contact between the thermocouple and the sample can sometimes create errors.

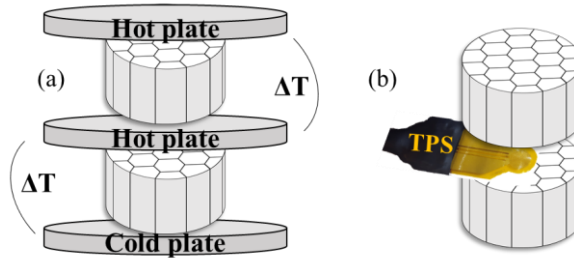


Figure 4. Common thermal conductivity steady state and transient techniques. (a) Guarded hot plate and (b) Hot Disk showing the disk-like transient plane sensor (TPS). (b) Taken from Apostolopoulou-Kalkavoura et al. 2021⁷¹.

The transient techniques measure the heat dissipation when a heat pulse hits the sample. They usually require shorter times and can measure smaller samples than steady-state techniques^{18,92,93}. The hot wire method^{15,31,37,43,48,49,82,102–105} and the hot strip method^{29,66,67,77,106,107} are both very common transient techniques used to determine the thermal conductivity of porous thermally insulating materials using a linear and a planar heat source. The transient plane source (TPS) or hot disk (Figure 4b)^{40,69,75,89,108–117}, using a spiral disk sensor between two identical sample pieces, is the most recent development of the hot wire and hot strip techniques^{92,118}. In general,

the effect of the contact between the sensor and the sample can be corrected for the transient techniques compared to the steady state but a good contact is prerequisite for a reliable measurement. The laser flash^{46,90,95,119,120} is also a transient technique but it measures the thermal diffusivity resulting in an indirect determination of the thermal conductivity^{49,92}. However, the laser flash minimizes the thermal contact issues as it uses a non-invasive laser beam. For thin films one can also use either the 3ω technique^{20,121–123} or the time-domain thermoreflectance (TDTR)^{124,125} which are both transient methods⁹³.

1.5 Cellulose: Structure and Intrinsic Anisotropy

Cellulose, being the dominating component of wood (Figure 5a-b), algae, tunicates, and cotton, is an abundant and renewable raw material with great potential for thermal insulation since it exhibits low thermal conductivity and tunable surface chemistry^{126–130}. The cellulose molecule is a linear-chain biopolymer consisting of glucose molecules and the repeating unit consists of two anhydroglucose rings linked through a covalent bond from the oxygen on C1 of one glucose ring to C4 of the other of glucose ring (1–4 glycosidic bond)¹³¹. Cellulose naturally exists in two crystalline forms: cellulose I _{α} , which has a one-chain triclinic unit cell, and cellulose I _{β} , which has a two-chain monoclinic unit cell^{126,132–134}.

Natural cellulose can be converted via various chemical treatments to cellulose II, III and IV, which can be used in other applications such as textiles and cellophane^{134–136}. Interestingly, cellulose possesses an intrinsic anisotropy (Figure 5c) which features covalent bonds and intramolecular hydrogen bonds along the *c*-axis and weaker interactions such as van der Waals and intermolecular hydrogen bonds along the *a* and *b* axes^{126,129,135,137}. The intrinsic anisotropy of cellulose crystals has been also confirmed by examining their thermal expansion coefficient, which is much higher along the *a*-axis than along the covalently bonded *c*-axis¹²⁶. Along the *c*-axis the covalent bonds restrain the thermal expansion while the less tightly fixed interfibrillar hydrogen bonds in the radial direction are more sensitive to temperature variations^{129,138}. Wada and Altaner et al. observed from X-ray diffraction and Fourier-transform infrared spectroscopy experiments respectively that the interfibrillar hydrogen bonds of cellulose become weaker upon increasing

temperature, resulting in an anisotropic thermal expansion along the three axes of cellulose^{129,138}.

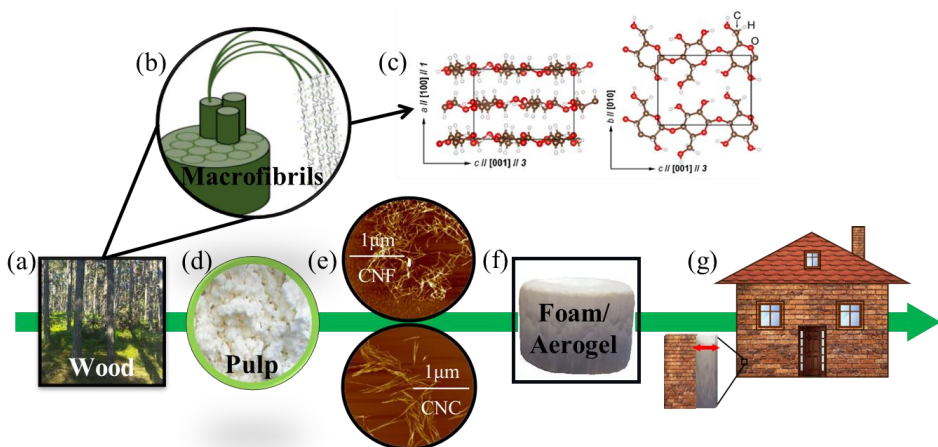


Figure 5. Wood cellulose for thermal insulation applications. (a) Wood: the major cellulose source. (b) The hierarchical structure of wood fibers. (c) The anisotropic structure of cellulose I β . (d) Wood pulp after processing. (e) Characteristic AFM pictures of cellulose nanomaterials (CNF and CNC). (f) CNM based foams or aerogels. (g) Thermal super-insulation applications. (c) is adapted from Apostolopoulou et al. 2020¹⁶.

1.5.1 Cellulose Nanomaterials (CNM)

The CNMs can be distinguished into CNF and CNC and can be produced through different mechanical and treatment pathways from cellulose fibers^{134,139}. Wood, which constitutes the major source of cellulose for producing cellulose nanomaterials, has a hierarchical structure in which the cellulose fibers consist of cellulose microfibrils (Figure 4b) in bundles and each microfibril consists of 30–40 cellulose chains. The cellulose fibers have widths of 20–30 μm and lengths of 1–3 mm and the cellulose microfibrils, which are commonly called CNF (Figure 5e), usually have widths of 3–4 nm and lengths around 2 μm . The CNFs are usually long flexible fibers with kinks and high aspect ratios. The CNCs (Figure 5e) are rigid rods with lower aspect ratio than CNF but higher degree of crystallinity^{139,140}.

1.5.2 Cellulose Nanofibrils (CNF)

The deliberation of CNF can be accomplished by mechanical disintegration in microfluidizers, high-pressure homogenizers, grinders, blenders, aqueous counter collision or screw-type extruders. Different parameters such as the level of desired defibrillation, the pretreatments of cellulose or the presence of hemicellulose will define the proper mechanical treatment for each case. Using only mechanical means for defibrillation usually results in fibrils with diameters over 10 nm. To enhance the fibrillation, to introduce desired properties such as surface charge cellulose and/or to improve colloidal stability, cellulose is usually subjected to chemical pretreatment¹³⁹.

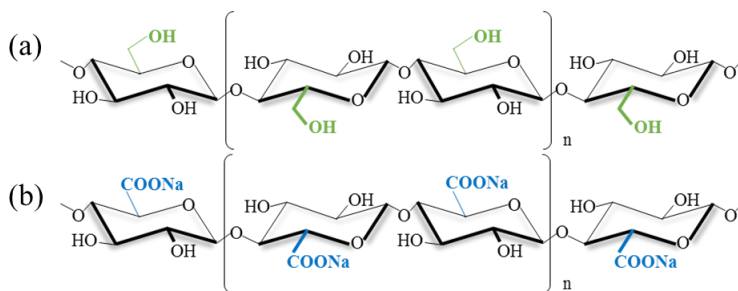


Figure 6. Cellulose I β unit cell. (a) Initial chemical structure and (b) TEMPO-oxidized chemical structure including the oxidation of the $-\text{CH}_2\text{OH}$ located at C₆ to $-\text{COO}^-\text{Na}^+$.

Common cellulose pretreatments are enzymatic hydrolysis, carboxymethylation and TEMPO (2,2,6,6-tetramethylpiperidine-1-oxyl radical)-mediated oxidation. During carboxymethylation, certain $-\text{OH}$ groups are replaced by $-\text{CH}_2\text{COO}^-$ while during TEMPO-mediated oxidation (Figure 6a,b) the $-\text{CH}_2\text{OH}$ groups located on the C₆ of the anhydroglucose unit are converted to $-\text{COO}^-$, thus introducing negative surface charges^{139–141}. However, during enzymatic hydrolysis, the surface glycoside bonds are partially cleaved to enhance the defibrillation of CNF. Combinations of chemical and mechanical treatment methods can result in high degree of fibrillation and thus in fibrils with smaller diameters (3–4 nm)¹³⁹.

1.5.3 Cellulose Nanocrystals (CNC)

In the most common synthesis of CNCs, cellulose pulp is treated with H_2SO_4 , which partially hydrolyzes and removes the disordered regions of cellulose to leave a highly crystalline material^{139,142}. Other acids such as HCl may be also used for the hydrolysis, introducing different surface properties and other aspect ratios¹⁴³. Interestingly, the CNC dispersions exhibit unique properties of self-assembly in chiral nematic liquid-crystalline phases above a critical concentration^{142,144}.

1.6 Thermal Conductivity of Wood and Cellulose

Cellulose $\text{I}\beta$ has an intrinsic anisotropy due to stronger bonding along than perpendicular to the cellulose chain (see Section 1.4). The intrinsic anisotropy caused by the presence of covalent bonding along the c -axis but not the b - and a -axes of the cellulose crystals is translated into thermal anisotropy because phonon propagation is directly correlated with the strength and density of atomic bonding^{21,145–147}. The weaker bonding limits phonon propagation, resulting in lower thermal conductivity values in the radial direction^{19,21,23,145,148–152}.

Wood, which is a great source of cellulose, exhibits an intrinsic thermal anisotropy (up to 1.7^{109}) and thermal conductivity estimations for different wood types confirm that thermal conductivity is higher along the covalent longitudinal direction ($323 \text{ mW m}^{-1} \text{ K}^{-1}$ for birch at 294 K), parallel to the grain (λ_a), than along the transverse (λ_r) direction ($214 \text{ mW m}^{-1} \text{ K}^{-1}$ at 294 K)¹⁵³. Other studies have estimated the anisotropic thermal conductivity of wood cellulose fibers¹⁵⁴ ($1040 \text{ mW m}^{-1} \text{ K}^{-1}$ and $260 \text{ mW m}^{-1} \text{ K}^{-1}$) or wood fibers¹⁵³ ($766 \text{ mW m}^{-1} \text{ K}^{-1}$ and $430 \text{ mW m}^{-1} \text{ K}^{-1}$), confirming large anisotropy in all cases. Of course, wood is less anisotropic than pure cellulose as it contains hemicelluloses, lignin and extractives in a hierarchical structure which may not possess the same intrinsic anisotropy as cellulose.

The anisotropic thermal conductivity of cellulose $\text{I}\beta$ crystals has been investigated by simulations resulting in values of about 900, 240 and $520 \text{ mW m}^{-1} \text{ K}^{-1}$ along the c (λ_a), a , and b (λ_r) axes, respectively at 298 K, with very little temperature sensitivity over a wide range (73–573 K)¹⁹. Furthermore, the

thermal conductivity of a single CNC particle estimated by MD simulations was $5700 \text{ mW m}^{-1} \text{ K}^{-1}$ along the covalent backbone compared to the $720 \text{ mW m}^{-1} \text{ K}^{-1}$ perpendicular to the chain.

To confirm this high anisotropy experimentally, Diaz et al. prepared bulk films consisting of aligned CNC particles, which exhibited thermal conductivities of 530 and $220 \text{ mW m}^{-1} \text{ K}^{-1}$ along (λ_a) and perpendicular to (λ_r) the fibers' direction. The difference between the thermal conductivity of single CNC particles and bulk CNC films can be explained with the interfacial thermal resistance estimated by Diaz et al. to be $9.4\text{--}12.6 \text{ m}^2 \text{ K GW}^{-1}$ ¹⁵⁵. Other attempts to measure the anisotropic thermal conductivity of various cellulosic films have shown that the thermal conductivity and the degree of anisotropy are affected by the cellulose type, crystallinity, crystallite size, and of course the degree of the particles' alignment. For instance, among the different CNM-based nanopapers tested by Uetani et al., the tunicate nanowhiskers (TNWs) exhibited the largest anisotropy while the TEMPO-oxidized Sugi cellulose nanofibril (TOSNF) the lowest (twofold)¹⁵⁶. The nanopapers with aligned TNWs had thermal conductivities of $2500 \text{ mW m}^{-1} \text{ K}^{-1}$ and $300 \text{ mW m}^{-1} \text{ K}^{-1}$ in the directions along (λ_a) and perpendicular (λ_r) to the fibers, respectively¹⁸. This eightfold anisotropy is similar to the anisotropy measured for single CNCs by Diaz et al., confirming the large intrinsic anisotropy of cellulose^{18,145,156}. Another study included the preparation of epoxy resin and CNF/epoxy resin nanocomposite; here, the addition of CNF introduced a fivefold anisotropy thermal conductivity, with values of 1100 and $230 \text{ mW m}^{-1} \text{ K}^{-1}$ along (λ_a) and perpendicular to the fibers (λ_r)¹⁵⁷.

1.7 Scope of the Thesis

As fossil fuels are depleted and CO₂ emissions are increasing, there is a pressing need to implement more renewable and eco-friendly thermal insulation materials. Cellulose is an emerging material which has high potential, but it is necessary to investigate in depth the CNM/cellulose-based foam/aerogel processing as well as heat transfer mechanisms.

Taking into consideration the hygroscopic character of many insulation materials and especially those made from biopolymers such as cellulose, the first goal of this thesis was the development of a measurement cell in which the temperature and relative humidity can be carefully controlled while thermal conductivity is measured. However, performing measurements in such a cell is not straightforward and many parameters had to be investigated and optimised (i.e. the wet density, the specific heat capacity and/or the volumetric shrinkage).

The second goal of this PhD thesis was to investigate the effect of relative humidity on thermal conductivity and understand the underlying mechanisms that influence heat transfer in both isotropic and anisotropic CNM-based foams. The effects of density, nanoporosity, degree of alignment, degree of crystallinity, and fibril dimensions on the thermal conductivity and moisture uptake of anisotropic CNM-based foams have been investigated and modelled. Specifically, one important aim was to estimate the importance of thermal boundary conductance and phonon scattering on the nanoscale for the effective thermal conductivity of the anisotropic foams. The research work has combined experimental measurements with theoretical calculations and molecular simulations, which mainly were performed by our collaborators. The thermal conductivity of isotropic CNF-based foams was also investigated and compared with expanded polystyrene insulation it was also attempted to model it following an engineering approach as function of the moisture uptake. The moisture uptake, being a crucial parameter, was further investigated in relation to temperature and crystallinity by a combination of experiments and molecular simulations performed by our collaborators.

To this end, this thesis sums up the dominant thermal conductivity contributions and paves the way for setting up the foundation of correct reporting of the thermal conductivity measurements of hygroscopic CNM foams.

2 Preparation of Materials

2.1 Preparation of Mechanically-ground CNF and TEMPO-mediated Oxidized CNF (TCNF)

For papers I, III and IV, the starting material was a never-dried sulfite softwood cellulose pulp (Domsjö dissolving Plus) provided by Domsjö Fabriker AB (Aditya Birla, Domsjö, Sweden). For paper V, the starting material was powdered Cladophora cellulose and provided by FMC Biopolymer.

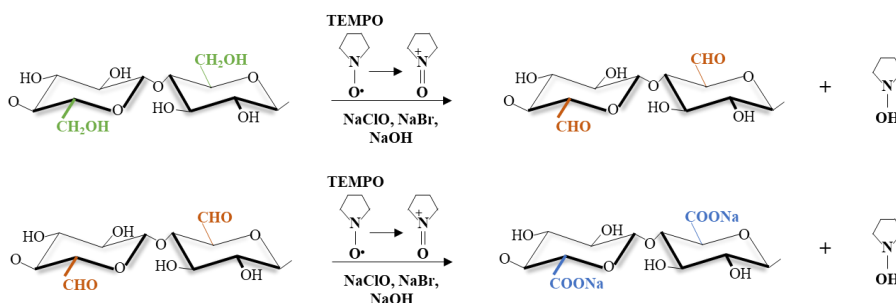


Figure 7. Simplified two-step reaction scheme in which TEMPO oxidizes the primary alcohol to give an aldehyde that is further oxidized to give a carboxylic group.

TEMPO-oxidized cellulose nanofibrils (TCNF) were prepared as previously reported¹⁵⁸ using the TEMPO/ NaBr / NaClO system (Figure 7). Before the oxidation, the cellulose pulp was washed with 0.01 M HCl solution and deionized water until the conductivity of the filtrate dropped below 5 μS . The washed pulp together with TEMPO (0.016 g per g of dry pulp) and NaBr (0.1 g per g of dry pulp) were mixed with deionized water and stirred. NaClO was added dropwise while the suspension was stirred. The pH of the suspension was monitored, and 0.5 M sodium hydroxide solution was added dropwise to maintain the pH at 10 during the entire oxidation reaction. For papers I–V different TCNF were prepared by varying the NaClO content from 2.5 to 10 mmol per gram of cellulose as well as the duration of the oxidation

(up to 4 h) to obtain different charge densities. The next step includes washing of the oxidized pulp with deionized water during filtration until the filtrate has a conductivity below 5 μS .

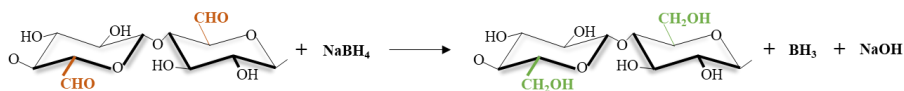


Figure 8. Simplified reduction reaction of the remaining aldehydes into primary alcohols.

For papers I and III, any residual aldehydes and ketones were reduced to primary alcohols (Figure 8) by adding 0.1 g of NaBH_4 per gram of cellulose to the TEMPO-oxidized cellulose pulp suspension at pH 10 under stirring for 3 h¹⁵⁹. After the reduction reaction, the pulp was again washed with deionized water until the conductivity was lower than 5 μS . For paper IV, no reduction reaction was performed.

For papers I and III, the TEMPO-oxidized cellulose pulps and the untreated pulp were grinded by a supermasscolloider grinder (Model MKZA10-15J, Masuko Sangyo Co., Ltd, Japan) equipped with non-porous grinding stones containing silicon carbide (Disk model MKE), using a gap clearance of $-100\ \mu\text{m}$ at a motor frequency of 30 Hz obtaining TCNF and CNF, respectively. For paper IV, the TEMPO-oxidized pulp was disintegrated by passing the dispersion four times through the $400\text{-}\mu\text{m}$ and $200\text{-}\mu\text{m}$ chambers of a high-pressure (1,600 bars) Microfluidizer (M-110EH, Microfluidics)⁷⁵.

The mechanically treated CNF are referred to as CNF_{19} in paper I with 19 representing the CNF diameter in nm. The TCNFs used in paper I are referred to as $\text{CNF}_{2.3}$ and $\text{CNF}_{4.4}$, where 2.4 and 4.4 are the diameters of the TCNF particles in nm. The TCNF used in paper III is referred to in the paper as ‘TCNF’ and the TCNF used in papers IV and V are referred in the papers as ‘CNF’.

2.2 Preparation of CNC and TEMPO-mediated Oxidized CNC (TCNC)

Two types of CNC were used in this thesis. For paper II, the commercial Cellulose CNC powder was selected and dispersed in deionized water using a mechanical stirrer obtaining a dispersion with 4.5 wt% concentration. To obtain higher or lower concentration dispersions we upconcentrated the initial dispersion using a rotary evaporator or diluted it with deionized water. For paper III, the TEMPO-oxidized CNC (TCNC) were prepared by acid hydrolysis (HCl 2.5 M) of the TCNF prepared with 10 mmol g⁻¹ of NaClO for 4 h at 105 °C. The TCNC were obtained by. The HCl was used to keep intact the surface chemistry of TCNF, as previously reported¹⁴³. To obtain a thoroughly clean final material, the TCNC were centrifuged and dialyzed against deionized water.

2.3 Preparation of Carboxymethylated CNF (CMCNF)

The CMCNF was prepared by our collaborators following a procedure described before^{160,161}. Briefly, the cellulose fibers were immersed in ethanol and then filtered, and this process was repeated three times to exchange water to ethanol. The fibers were soaked in a solution of 0.3 g monochloroacetic acid in isopropanol 15 ml for 30 minutes. Then the fibers were placed in a solution of NaOH, methanol and isopropanol at 82 °C. The carboxymethylation lasted for 60 min and was followed by deionized water, 0.1 M acetic acid, and deionized water filtration steps. To convert the pulp into the Na⁺ form, the treated fibers were immersed for 30 min in 4 wt% NaHCO₃(aq) and post-filtered with deionized water. The carboxymethylated pulp was disintegrated in a high-pressure microfluidizer (M-110EH, Microfluidics) by a single pass through the 400-μm and 200-μm chambers and four times through the 200- and 100-μm chambers. Finally, the material was sonicated and centrifuged.

2.4 Preparation of the CNF@Al-MIL-53 Nanofibers

For paper V, the CNF@Al-MIL-53 nanofibers were prepared by our collaborators by growing continuous Al-MIL-53 metal–organic framework (MOF) layers on ultrafine CNFs via interfacial reactions, as has been described¹⁶². Briefly, TCNF with a charge density of 1.3 mmol COO[−] g^{−1} of cellulose, made from *Cladophora* cellulose extracted from algae, was firstly ion-exchanged with Al³⁺ and surface-modified with the surfactant polyvinylpyrrolidone (PVP) to regulate the growth and crystallization of MOFs. Then a solution of 0.75 g metal salt (aluminum nitrate nonahydrate, Al(NO₃)₃·9H₂O) in 10 ml water and a solution of 0.21 g of the organic ligand (disodiumterephthalate, Na₂BDC) in 10 ml water were added in the TCNF suspension dropwise while stirring.

2.5 Preparation of Anisotropic Foams by Freeze-Casting

Anisotropic CNF, TCNF, CNC or TCNC foams for papers I–III were prepared by unidirectional ice templating, also called freeze-casting^{38,70}, from the corresponding dispersions. For papers I and III, the dispersions of CNF, TCNF or TCNC were diluted to 0.5 wt% in DI. For paper II, the the dispersions of CNC were adjusted to the desired concentration. Teflon molds 4 cm in diameter with copper bottom plates were filled with 30 mL of CNM dispersion and placed in contact with a dry ice plate, allowing unidirectional freezing, with cooling rate 3 K min^{−1}, of from the bottom to the top. The final dry foams were obtained by ice sublimation at 0.024 mbar and room temperature (RT) for four days using a freeze-dryer (Christ Alpha 1-2LDplus, Germany).

2.6 Preparation of Isotropic foams

In this thesis two different types of isotropic foams or aerogels are examined, the CNF–polyoxamer foams and the CAM (CNF–AL-MIL-53) foams. The CNF–polyoxamer foams were prepared by mixing the TCNF

dispersion, which had a concentration of 0.5 or 0.7 wt% and a charge density in cellulose of 1.6 mmol with CaCO_3 particles and the triblock poly(ethylene glycol)-poly(propylene glycol)-poly(ethylene glycol) polyoxamer copolymer, P123. The foaming was done using Ultra-Turrax (T18 IKA Werke, Germany) for 3 min at 7000 rpm in a process optimized and analytically described before⁷⁵. Towards the last minute of the foaming, D-(+)-gluconic acid D-lactone (GDL) was added gradually.. The foams were then dried at 60 °C in glass beakers covered with a perforated aluminum film until it was ensured that the foams were completely dry.

The CAM aerogels were prepared by our collaborators by pouring aqueous suspensions of the CNF@Al-MIL-53 nanofiber into copper vessels which were immersed for 60 min in liquid nitrogen. After freeze-drying for 48 h, the aerogels were then infiltrated in a Na_2BDC solution and an $\text{Al}(\text{NO}_3)_3 \cdot 9\text{H}_2\text{O}$ solution was added dropwise. The extended growth of Al-MIL-53 was ensured by gently shaking the mixture for 10 h. The treated aerogels were washed with deionized water and freeze-dried again to obtain the crosslinked CAM aerogel. The mass fraction of the Al-MIL-53 in the CAM aerogel was 30%.

3 Characterization of Dispersions and Foams

3.1 Thermal Conductivity

The thermal conductivities (λ , $\text{mW m}^{-1} \text{K}^{-1}$) of all the foams and aerogels in Papers I, II, IV and V were measured in a customized conditioning measurement cell (Figure 9a-b), ensuring the careful conditioning at a specific T and RH prior to and during the measurement. The cell was connected to a TPS 2500 S Hot Disk Thermal Constants Analyzer¹¹⁸, which offers the opportunity to measure both isotropic and anisotropic samples with high precision (Figure 9a). The customized measurement cell has three apertures on the top and one on the side. The side aperture is used to introduce the TPS sensor. The top apertures are used to introduce the humidified air produced by a P2 Cellkraft humidifier¹⁶³, to let out the conditioning air and to accommodate the ΔT sensor. The ΔT sensor is connected to the Hot Disk and measures the temperature variations. Temperature control is achieved by immersing the measurement cell in a silicone oil bath and conditioning the sample at the desired temperature.

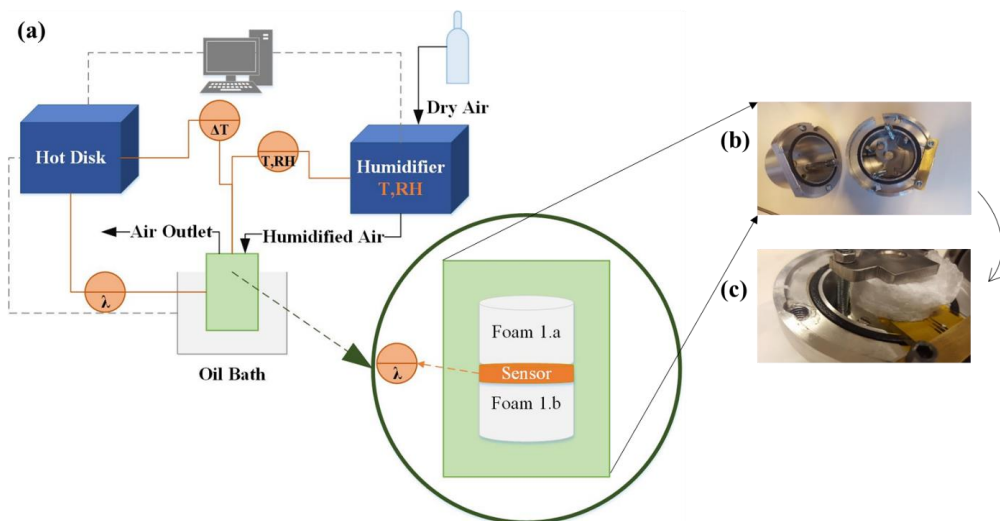


Figure 9. Thermal conductivity measurement cell. (a) Schematic illustration of the customized measurement cell connected to the Hot Disk and the humidifier and immersed in the silicone oil bath. (b) Top view of the empty

measurement cell. (c) The TPS sensor sandwiched between two foam samples. (a) and (c) are taken from Apostolopoulou-Kalkavoura et al. 2018¹¹⁴.

Once the ΔT is very low (<0.25 °C) and the RH is stable (± 0.1), the measurement can be performed. The conditioning prior to the measurement lasted for 2–4 hrs depending on the desired conditions. The total time for specific T and RH considering the pre-conditioning and five independent measurements at 15-min intervals was 3–5 h. In this thesis, the measurements were performed at 262, 277, 295 and 313 K and 5, 20, 35, 50, 65 and 80% RH . The samples were 1.5–2.5 cm in height and 3–4 cm in diameter. For each measurement, the TPS sensor was sandwiched between two identical foam/aerogel pieces. To ensure good thermal contact between the sensor and the sample, a small weight was added on the top of the samples (Figure 9c). Depending on the anisotropy, sample dimensions and thermal diffusivity, the 3.2 mm and 6.4 mm TPS sensors were used for 5–10 seconds at 10–20 mW power.

During the transient power pulse measurement, the time-dependent temperature increase is recorded at 200 points. The first points represent the heating of the TPS sensor and are therefore removed until a low standard deviation is obtained. The selection of the TPS sensor is based on the principle that the dimensionless total characteristic time, which equals the product of thermal diffusivity (the radial one in case of anisotropic materials) multiplied by the test time divided by the square of the sensor's radius, should be between 0.3 and 1¹⁶⁴. Prior to the measurement, the thermal diffusivity is unknown but, in most cases, it could be guessed based on similar measured samples. The dimensionless total characteristic time is part of the calculated results and if the value is smaller than 0.3 or greater than 1, another sensor could be then selected. Another important parameter indicating the consistency of the measurement is the probing depth. The probing depth represents the available distance for the heat to travel within the sample and it equals the height (axially) and/or the radius of the sample subtracting the radius of the sensor (radially). If the calculated probing depth from the results of the measurement exceeds the actual one, then the heat has travelled outside the sample boundaries and in most cases the measurement should be discarded. In some cases, if the calculated probing depth is only a bit higher than the actual one the measurement can be considered valid after removing measurement points

from the end of the transient measurement. In general, if the probing depth is too high, lower power, shorter test time or another TPS sensor could be considered as options to overcome the problem and obtain an accurate measurement.

Once a valid measurement is performed, the thermal diffusivity (α_r) or the radial thermal diffusivity (a_r) in case of anisotropic materials is obtained by an iteration process having a linear relationship between the temperature increase, $\Delta T(\tau)$, and the dimensionless time dependent function, $D(\tau)$ (Equation 10). The $D(\tau)$ is a function of the of the αr , the radius of the TPS sensor and the test time.

$$\Delta T(\tau) = S D(\tau) \quad (10)$$

where S is the slope of the linear relationship between the $\Delta T(\tau)$ and $D(\tau)$, and can be determined from Equation 11 in case of isotropic or Equation 12 in case of anisotropic materials¹⁰⁹.

$$S = \frac{P_0}{r\pi^{3/2}\lambda} \quad (11)$$

$$S = \frac{P_0}{r\pi^{3/2}(\lambda_a\lambda_r)^{1/2}} \quad (12)$$

where P_0 is the total power output of the sensor, r is the radius of the TPS sensor, λ is isotropic thermal conductivity, λ_a is axial thermal conductivity and λ_r is radial thermal conductivity. In the case of isotropic materials, both thermal diffusivity and thermal conductivity can be determined at this step. To measure the thermal conductivity of isotropic samples, the input of the measurement time, the power and the smallest probing depth are the only requirements. However, to measure the thermal conductivity of anisotropic samples, the density and the specific heat capacity (C_p) must be introduced as input values for the measurements. As the cellulosic foams, which represent the core of this thesis, are hygroscopic materials both the density and the C_p must be corrected against the moisture uptake. The $C_{p_{wet}}$ is calculated by the rule of mixtures (Equation 13).

$$C_{p_{wet}} = (1 - H_2O_w) \times C_{p_{dry}} + C_{p_{H_2O}} \times H_2O_w \quad (13)$$

where H_2O_w is the wt% water content in the CNF foams, $C_{p_{dry}}$ is the dry specific heat capacity of the CNF foams measured in the DSC and $C_{p_{H_2O}}$ is the specific heat capacity of water. The ρ_{wet} was corrected against the wet mass but also against the volume shrinkage. The volume shrinkage is caused by the weight which is added to ensure good thermal contact especially in the very

low-density foams. The foams weaken upon increasing moisture content resulting in axial shrinkage mostly for $RH > 65\%$. The volume shrinkage was determined by conditioning the sample in the measurement setup used in thermal conductivity experiments and measuring the volume with a caliper after each RH cycle. Once the C_P and the density are known both the axial (λ_a) and radial (λ_r) thermal conductivities are measured simultaneously in the anisotropic mode of the Hot Disk.

Having then the correct C_P , the λ_r and λ_a are automatically calculated by the Hot Disk using Equations 14 and 15¹⁰⁹.

$$\lambda_r = \alpha_r \rho C_P \quad (14)$$

$$\lambda_a = \left(\frac{P_0}{\pi^{3/2} r m} \right)^2 \frac{1}{\lambda_r} \quad (15)$$

where m is the number of concentric rings equally spaced on the TPS sensor. The axial thermal diffusivity (α_a) is then calculated by Equation 14 using the λ_a instead of the λ_r calculated by Equation 15.

The main challenges to obtaining valid and accurate thermal conductivity measurements were to select the right TPS sensor, to select the right power and time and to accurately determine C_P . Usually, small sensors or very short test times are linked with more problematic measurements in the literature and it is always suggested to use the biggest sensor possible for the longest possible duration^{164,165}. The foams and aerogels having a porosity larger than 90% have large thermal diffusivities making it important to use the biggest possible TPS sensor considering of course the limitations of the dimensionless characteristic time and the probing depth. One limiting factor is usually the sample size as larger samples minimize problems related to the available probing depth. The test time and the power are determined by trial and error considering their effect on the dimensionless characteristic time and the probing depth, as well as on the temperature increase, which should always remain within the recommended limits. The principles of the C_P measurement are summarized in paragraph 3.2.

3.2 Differential Scanning Calorimetry (DSC)

DSC (Mettler Toledo 820, Sweden) was used to estimate the specific heat capacity of the anisotropic foams in Papers I and II.

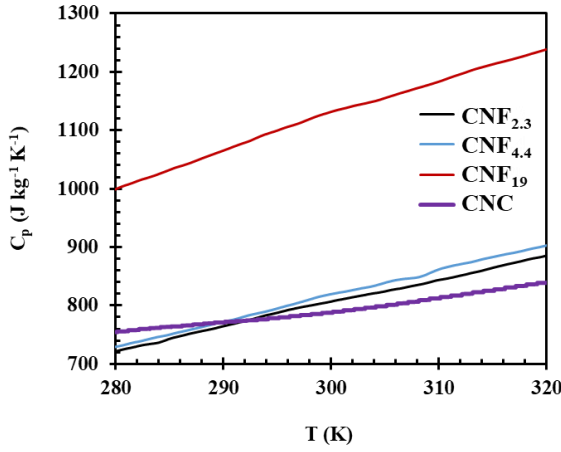


Figure 10. C_p of different CNMs between 280 and 320 K. The figure is partially adapted from Apostolopoulou-Kalkavoura et al. 2021⁷¹.

Considering the hygroscopicity of cellulose, the foams were dried in three steps. A CNM foam was firstly dried in the oven at 105 °C for 24 h. After the first drying step, a small piece of the CNM foam ($\approx 10^{-2}$ g) was placed in a crucible. The lid was affixed and then pierced with a small needle. As the foam has been exposed to room conditions during the sample preparation, the crucible with the sample was again placed in the oven at 105 °C for 24 h to ensure the removal of water. After the second cycle of drying, the three DSC samples were measured: the empty (reference) crucible, the crucible with the standard (sapphire) and the oven-dried crucible with the sample. All three samples were first heated at 105 °C in situ for 10 min before the C_p was measured between -20 and 50 °C at heating rate of 10 K min^{-1} under N_2 atmosphere. The in-situ heating was performed to ensure that the samples were perfectly dried. The crucible had been weighed empty, with the sample and after the second drying, and the latter mass was used in the calculations of the C_p . There are many parameters affecting the C_p such as the crystallinity, the particle diameter, the particle aspect ratio, and the surface area^{166,167}. The higher aspect ratio and the smaller diameter of nanoparticles have been both connected to lower specific heat capacity¹⁶⁶ explaining why the CNF₁₉ (Figure 10) which possesses the lowest aspect ratio, and the biggest diameter exhibits higher C_p .

3.3 Gravimetric Moisture Uptake

The moisture uptake of the CNF, TCNF or CNC foams for Papers I– IV was determined gravimetrically under controlled RH and T (Figure 11a). In a humidity chamber, a high-precision balance (BP 210 S, Sartorius, Germany) connected to a computer recorded the weight every 300 s. The foams were measured at 285, 295, 303, 308 and 313 K. Each temperature (T) cycle included measurements at 20, 35, 50, 65 and 80% RH . The samples were considered to be dry at 313 K and 20% RH as the mass values under these conditions were similar to the dry mass confirmed by TGA or oven drying after the moisture removal. The measurement at a constant T and RH lasted 6 h to ensure that steady state was reached and only the mass over the last 1 h was used to calculate the moisture content (H_2O_w) as a function of RH . Typical CNM-based foams had a moisture uptake of 6–25 wt% depending on the composition, crystallinity, density, and surface charge (Figure 11b).

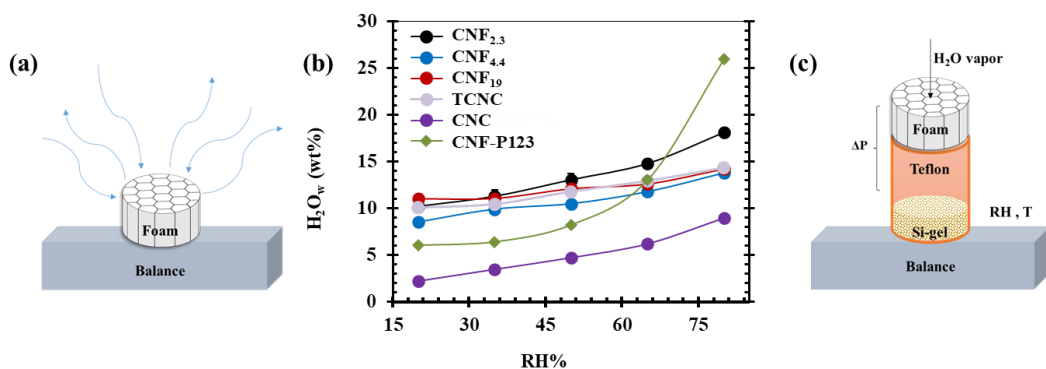


Figure 11. Gravimetric moisture uptake in a humidity chamber. (a) Experimental setup for moisture uptake. (b) Typical moisture uptake of various CNF-, TCNF- and CNC-based foam samples. (c) Water vapor permeability (WVP) setup. (b) Adapted from Apostolopoulou-Kalkavoura et al. 2018¹⁴ and Apostolopoulou-Kalkavoura et al. 2021⁷¹.

3.4 Water Vapor Permeability

Similarly to the moisture uptake, the water vapor permeability (*WVP*) of the CNF- and nonionic polyoxamer-based foams was determined gravimetrically as a function of *RH* in a humidity chamber (Figure 11c) under controlled *T* and *RH* following the standard E96 method^{168,169}. To ensure a water vapor flow, a ΔP was created because the foam was sealed laterally by using a cylindrical Teflon beaker and the bottom of the beaker contained Si- gel to maintain dry conditions under the foam. The *WVP*, and the water vapor resistance factor (μ) were calculated from Equations 16 and 17^{168,170}.

$$WVP = \frac{S \times h}{A \times \Delta P} \quad (16)$$

$$\mu = \frac{\delta_{air}}{WVP} \quad (17)$$

where *S* is the slope of the mass gain of the foam, *h* is the height of the foam, *A* is the exposed surface area, ΔP is the vapor pressure difference between the top and the bottom of the foam, and δ_{air} ($=1.97719 \times 10^{-10}$ kg (msPa)⁻¹ at *T* = 295 K and *P* = 1 atm) is the water vapor diffusion coefficient in air.

3.5 Nitrogen Adsorption

To estimate the surface area and the pore volume of the CNM-based foams for papers I, II and IV, nitrogen adsorption measurements were performed using the ASAP 2020 (Micromeritics Instrument Corporation, Norcross, GA, USA). The CNF foams were placed in the measurement tubes and degassing lasted 10 h at 70 °C. The surface area and the pore volume during adsorption were calculated by the Brunauer–Emmett–Teller (BET)¹⁷¹ and Barrett–Joyner–Halenda (BJH)¹⁷² methods, respectively. For paper V, the degassing was performed at 100 °C for 10 h.

Figure 12 summarizes the specific surface area measured by nitrogen adsorption for all foams and aerogels in this thesis. The Cladophora CNF (CC-CNF) exhibits much higher specific surface area than other CNF foams since the Cladophora fibers are mesoporous compared to the wood cellulose fibers¹³⁰. Furthermore, the CAM aerogels have more than twice the surface area of the CC-CNF aerogels due to the microporous MOF, which offers a great potential to minimize gas conduction in the small pores due to the

Knudsen effect. On the other hand, the CNF–P123 foams exhibit the smallest surface area since they suffered the greatest capillary forces, as they are oven-dried.

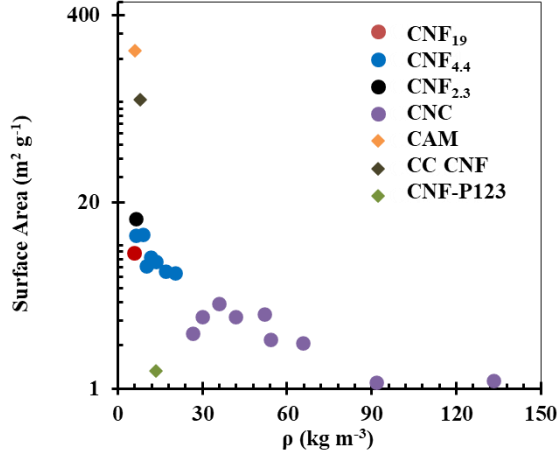


Figure 12. BET surface area measured with nitrogen adsorption experiments for different foams and aerogels included in the thesis. The \blacklozenge indicates the isotropic foams and aerogels while the \bullet indicates the anisotropic foams and aerogels. Adapted from Apostolopoulou-Kalkavoura et al 2021⁷¹.

The surface area of pure CNF/TCNF anisotropic foams scales with the surface charge and reaches the highest surface area for the CNF_{2.3}. The anisotropic CNC foams have small surface areas especially at high densities where the particles are packed closer to each other.

3.6 Foam Density and Porosity

The porosity (Π) of the foams was determined from the skeletal (ρ_{skel}) and the apparent foam density (ρ_{app}) calculated from the mass divided by the volume of the foams, at 295 K and 0–80% RH.

$$\Pi_{mp} = 1 - \frac{\rho_{app}}{\rho_{scel}} \quad (18)$$

As the anisotropic foams exhibited a hierarchical porous structure that combined macropores and nanosized pores (nanopores), the porosity of the nanopores, (Π_{np}) in the foam walls was estimated using Equation 19.

$$\Pi_{np} = 1 - \frac{\rho_{fw}}{\rho_{scl}} \quad (19)$$

where ρ_{fw} is the density of the foam wall and ρ_{scl} is the skeletal density of cellulose. The ρ_{fw} is estimated by Equation 20:

$$\rho_{fw} = \frac{m_{wet}}{V_f \times (1 - \Pi) + V_{ms}} \quad (20)$$

where m_{wet} is the wet mass of the foam at 295 K and 0–80% RH, V_f is the volume of the foam, Π is the total porosity of the foam (macro- and nanoporosity), and V_{ms} is the volume of the nanopores in the foam walls measured by nitrogen sorption at RH = 0.

3.7 Scanning Electron Microscopy (SEM)

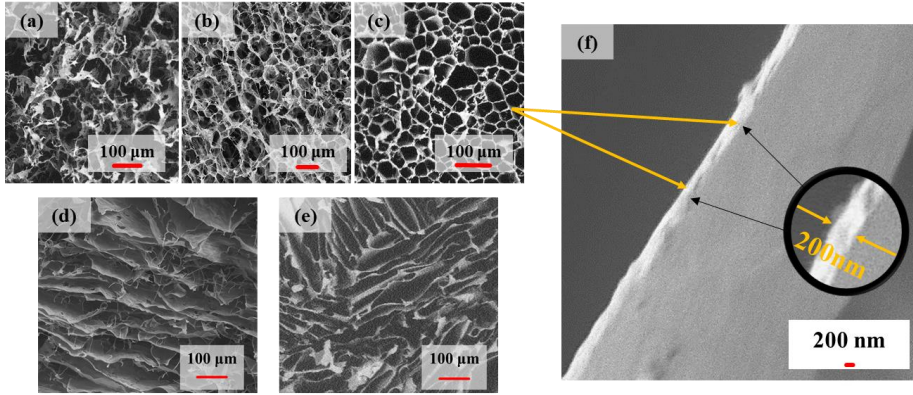


Figure 13. Representative SEM and HRSEM images of CNM foams. SEM images of (a) CNF₁₉, (b) CNF_{4.4}, (c) CNF_{2.3} and (d) TCNC made from 0.5 wt% dispersions. SEM image of (e) CNC foam made from a 5 wt% dispersion. (f) Wall of a CNF_{2.3} foam. (a), (b), (c) and (f) are taken from Apostolopoulou-Kalkavoura et al. 2021⁷¹.

The morphology of the CNM-based foams, the porous structure of the cross-sections along the radial direction (Figure 13a-e) and the foam walls

(Figure 13f), as well as the structure along the freezing front in case of anisotropic CNM-based foams were characterized by SEM and high-resolution SEM (HRSEM). The SEM images of the foam cross-section and along the freezing front were taken using a HITACHI TM-3000 (Germany) using a 5 kV electron beam. The HRSEM images of the foam wall were taken using a JEOL JSM-7401F (USA) and a 0.5-kV electron beam. Prior to imaging, the samples were cut in pieces and coated with gold to minimize the charging effects (35 s in 10 mbar Ar). To be able to have a sharp cut, the foams were cut frozen.

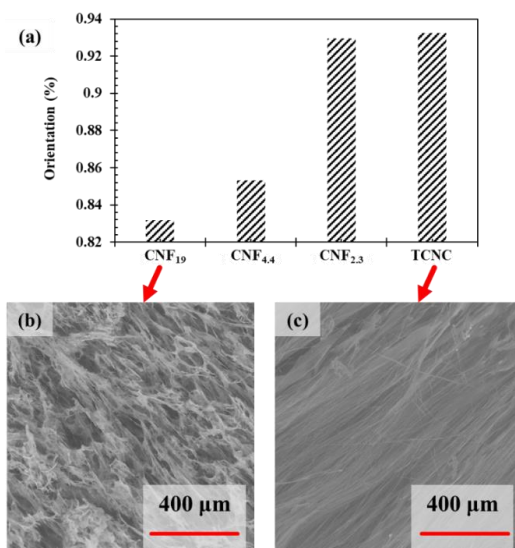


Figure 14. Foam orientation degree from SEM image analysis. (a) Orientation degree of different CNMs. SEM images along the freezing front of (b) CNF₁₉ and (c) TCNC foams. (a) Adapted from Apostolopoulou-Kalkavoura et al. 2021⁷¹.

The foams' orientation degree (Figure 14a) was also estimated from SEM image analysis (Figure 14b,c) in Image J software and the plug-in "OrientationJ"¹⁷³. The orientation of each pixel was compared with respect to neighboring pixels (1280 x 960), and the frequency was plotted against the angle to give a histogram for each image. This was fitted to a Gaussian curve and the orientation index (f) was calculated by Equation 21.

$$f = \frac{180 - \text{fwhm}}{180} \quad (21)$$

where fwhm is the full width at half-maximum of the curve.

3.8 Conductometric Titration

The charge density of all CNF, TCNF and TCNC samples (Figure 15a) prepared was estimated by conductometric titration, which has been previously described¹⁷⁴. Briefly, the titration is performed with 0.01 M NaOH as titrant after converting the cellulosic samples into their proton (H^+) form with the addition of HCl. During the dropwise addition of NaOH to the pulp or CNF/TCNF solution, the conductivity is recorded.

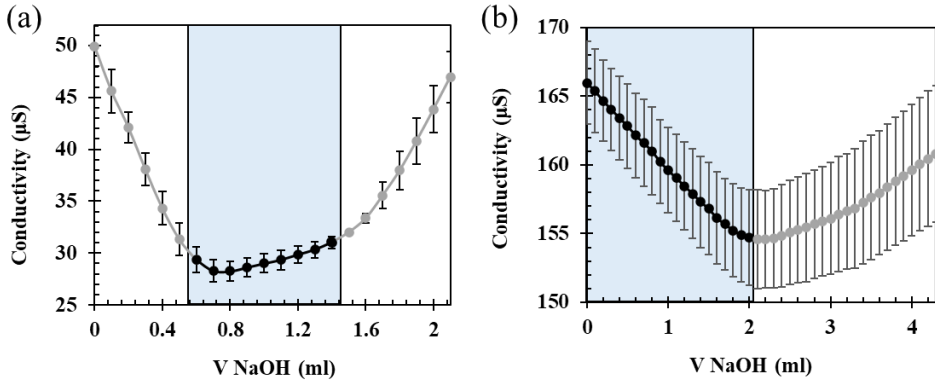


Figure 15. Representative titration curves for the determination of the surface charge of CNMs. (a) Conductivity vs the volume of NaOH for TEMPO-oxidized pulp/TCNC titration with the blue zone illustrating the stabilization zone or phase II in which the neutralization of the $-\text{COOH}$ is occurring. (b) Conductivity vs the volume of NaOH for Celluforce CNC with the blue zone illustrating the neutralization of the $-\text{OSO}_3^{3-}$.

There are three phases in the graph of conductivity vs the consumed NaOH volume. During phases one and two, the free H^+ groups and the weak acidic groups ($-\text{COOH}$) are neutralized with NaOH resulting in conductivity reduction and stabilization. During phase three the accumulation of NaOH results in increased conductivity and the titration is finished. The volume of NaOH consumed during the stabilization (plateau) during phase two is used

to estimate the charge density in mmol per g of dry cellulose. The TCNFs (CNF_{2.3} and CNF_{4.4}) and the CNF (CNF₁₉) used in paper I had charge densities of 1.60 ± 0.01 , 0.30 ± 0.02 and 0.02 ± 0.004 mmol per g of cellulose. The TCNF used in paper III had a charge density of 1.60 ± 0.01 mmol per g of cellulose. The TCNF used in paper IV had a charge density of 1.60 ± 0.01 mmol per g of cellulose. The TCNF used in paper V had a charge density of 1.30 mmol per g of cellulose.

To determine the surface charge of commercial Cellulforce CNC (Figure 15b), the procedure was slightly different^{142,175}. The commercial CNC can contain ionic residues from the production and usually contains surface groups in Na⁺ form; thus, sonication and dialysis against deionized water, followed by protonation of all surface groups using a strong acidic ion exchange resin (Alfa Aesar Dowex Marathon C, H⁺ form) was performed. After ensuring the protonation of the sulfate half-ester ($-\text{OSO}_3^-$) groups, NaCl was added to increase the conductivity in a detectable range and the titration was performed with 0.002 M NaOH. The volume of NaOH consumed up to the equivalence point (the point where conductivity started to increase) was used to determine the charge density of Cellulforce CNC in mmol $-\text{OSO}_3^-$ per gram of cellulose.

3.9 Atomic Force Microscopy (AFM)

AFM (Dimension 3100, Bruker, USA) operated in tapping mode was used to determine the dimensions of CNM samples. A droplet of aqueous CNM dispersion with concentrations around 0.001–0.005 wt% was deposited onto a freshly cleaved mica substrate and dried at RT. To avoid the formation of aggregates in some samples the freshly cleaved mica substrate was modified with (3-aminopropyl) triethoxysilane (APTES) and dried using dry air. Figures 16a-d illustrate different CNMs used in this thesis. In certain cases, the length was difficult to estimate directly from AFM images due to the high standard deviation.

The CNF/TCNFs (Figures 16a-c) used in paper I had diameters of 2.3 ± 0.7 nm (CNF_{2.3}), 4.4 ± 1.8 nm (CNF_{4.4}) and 19 ± 7.9 nm (CNF₁₉). The CNC in paper II had a diameter of 4.3 ± 0.8 nm and a length of 173 ± 41 nm. The TCNF used in paper III had a diameter of 2.3 ± 0.7 nm and the TCNC (Figure 16d) and had a diameter of 4.8 ± 1.3 nm and a length of 343 ± 91 nm. The

TCNF used in paper IV had a diameter of 2.9 ± 0.9 nm and a length up to 1 μm .

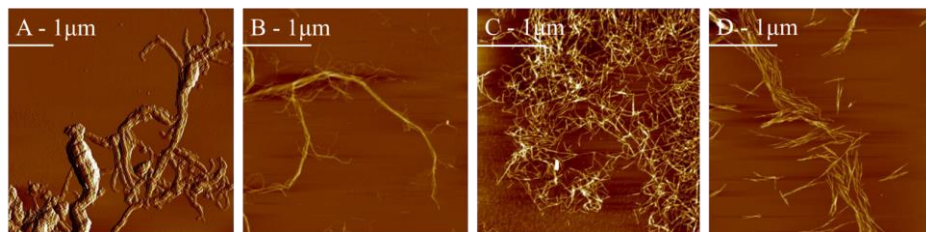


Figure 16. AFM images of different CNMs. (a) CNF₁₉ from Paper I, (b) CNF_{4.4} from Paper I and (c) CNF_{2.3} for Papers I, III and (d) TCNC from Paper III. Adapted from Apostolopoulou-Kalkavoura et al. 2021⁷¹.

3.10 Other Characterization Techniques

3.10.1 Aspect Ratio by Sedimentation Experiments

Sedimentation experiments were conducted to directly determine the aspect ratios of the CNF (CNF₁₉) and TCNF (CNF_{2.3}, CNF_{4.4}). The aspect ratio was assessed and calculated as previously reported^{176,177} from Crowding Number theory. Briefly, the low- and medium-charge CNF and TCNF (CNF₁₉ and the CNF_{4.4}) were dispersed in deionized water at six different concentrations (0.05, 0.08, 0.1, 0.2, 0.3 and 0.4 wt%) and the high-charge TCNF (CNF_{2.3}) was dispersed in 4 M aqueous NaCl solution at three different concentrations (0.02, 0.05, 0.08 wt%). The diluted suspensions were homogenized using an Ultra-Turrax (T18 IKA Werke, Germany) for 1 min at 10,000 rpm¹⁷⁶. The suspensions were then poured in cylindrical glassware to sediment and the heights of the sediments were measured after one week.

Knowing the aspect ratio, we can estimate the average length of the CNF/TCNFs, which is usually hard to assess by AFM due to entanglement, kinks or aggregation.

The ratio of the height of sediment divided by the height of the suspension (h_s/h_0) was plotted against the initial concentration (c_0) and fitted with a

quadratic curve. The linear term of the fit corresponds to the gel point concentration g_c . Based then on the Crowding Number theory, the aspect ratio (A) can be calculated from Equations 22 and 23.

$$g_c = \frac{2A}{A^2} \quad (22)$$

$$A = 4.90 \times C \left(\frac{\rho_l}{\rho_f} \right) \quad (23)$$

Where C is weight fraction (g of fibrils per g of suspension), ρ_l is the density of the liquid water and ρ_f is the density of cellulose fibrils ($=1500 \text{ kg m}^{-3}$). The aspect ratios of CNF₁₉, CNF_{4.4}, CNF_{2.3} and the TCNC used in Paper I and III were 110 ± 26 , 140 ± 4 , 200 ± 16 , and 89 ± 36 respectively (Figure 17). The aspect ratio of the latter sample was estimated both via sedimentation and AFM measurements to evaluate the accuracy of the data and the convergence of the two methods. The AFM-measured aspect ratio of the TCNC was 73 ± 27 , not significantly different from the 89 ± 36 estimated from the sedimentation. Thus, both methods converged even though the standard deviations were high.

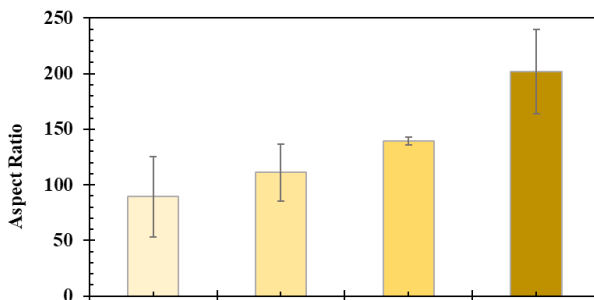


Figure 17. Aspect ratio of different CNMs. Adapted from Apostolopoulou-Kalkavoura et al. 2021⁷¹.

Figure 17 summarizes that the CNF/TCNFs exhibit greater aspect ratios than CNCs but also the fact that highly TEMPO-oxidized samples exhibit the highest aspect ratio due to significant reduction of the fibril diameter (2.3 nm).

3.10.2 X-ray Diffraction (XRD)

XRD (Oxford Diffraction Xcalibur 3, Agilent Technologies, U.S.A.) was used to determine both the crystallinity index and Hermans' orientation parameter of the CNF, TCNF or CNC in the foam walls for Papers I– III.

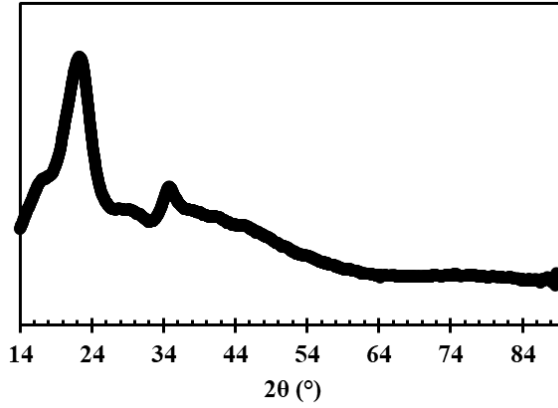


Figure 18. Typical XRD 1D diffractogram for the CNF_{2.3} foam sample used in Papers I and III. Adapted from Apostolopoulou-Kalkavoura et al. 2021⁷¹.

The crystallinity index (CI) of the CNF, TCNF or CNC foams was calculated from 1D diffractograms (Figure 18) obtained by integrating the 2D patterns using the Segal method¹⁷⁸ (Equation 24) after converting the angular values measured with the molybdenum (Mo) source to the values for copper (Cu).

$$CI(\%) = \frac{I_{200} - I_{am}}{I_{200}} \times 100 \quad (24)$$

where, I_{200} is the intensity value for the (200) peak of crystalline cellulose located at $2\theta = 22\text{--}23^\circ$ and I_{am} is the intensity value for the peak for amorphous cellulose located at $2\theta = 18\text{--}19^\circ$.

The Hermans' orientation parameter of the fibrils within the foams was calculated from 2D XRD patterns (Figure 19a) obtained on foam pieces prepared by compressing them radially to avoid disrupting the alignment. The Hermans' orientation parameter, f_H , quantitatively describes the alignment of

the nanofibrils or nanorods along the axial direction. The f_H (Equations 25 and 26) is obtained by azimuthal integration of the (200) peak of cellulose.

$$f_H = \frac{3\langle \cos^2 \varphi \rangle - 1}{2} \quad (25)$$

$$\langle \cos^2 \varphi \rangle = \frac{\int_0^{\pi/2} I(\varphi) \sin \varphi \cos^2 \varphi d\varphi}{\int_0^{\pi/2} I(\varphi) \sin \varphi d\varphi} \quad (26)$$

where φ represents the theoretical angle between a nanofibril main direction and the freezing direction of ice crystals during ice templating. This angle can be identified as the azimuthal angle (Figure 19b) on the 2D pattern (Figure 1c). $I(\varphi)$ represents the intensity at a certain φ angle¹⁷⁹.

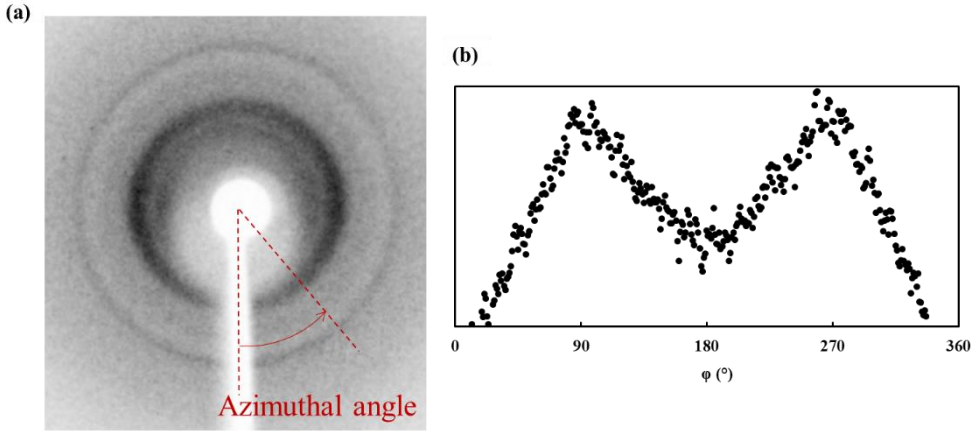


Figure 19. Calculation of Hermans' orientation parameter. (a) Typical 2D XRD pattern for the CNF_{2,3} and (b) the intensity plotted against the azimuthal angle. The Figure is taken from Apostolopoulou-Kalkavoura et al. 2021⁷¹.

3.10.3 Mechanical Compression

To estimate the compressive behavior of anisotropic and CNC foams in Paper II along the axial direction, the foams were compressed in an Instron 5966 (Instron, U.S.A.) equipped with a 100 N load cell. Prior to the measurements, to ensure the reproducibility of the experiments, the foams were conditioned for minimum 24 h at 296 K and 50% RH. The compressive behavior was tested on five foam samples for each CNC foam density at a

compression rate of $10\% \text{ min}^{-1}$ at 296 K and 50% *RH*. The compressive Young's modulus was determined from the slope of the initial linear region of the stress–strain curve, and the energy absorbed by the foam (i.e., toughness) was evaluated from the area under the stress–strain curve up to 70% strain¹⁸⁰.

4 Heat Transfer and Moisture Transport of Anisotropic CNM Foams (Papers I, II and III)

The intrinsic anisotropy of cellulose makes it a potential raw material for anisotropic materials which can inhibit heat transfer in one direction and favor it in the other one^{19,145}. Wood,^{90,153} which contains aligned cellulose fibers, and graphene^{120,181,182} are examples of anisotropic materials which have unique properties and can be used in a variety of applications. The directional heat management materials can be used for instance in heat dissipation applications for electronic devices, packaging, or building insulation. Cellulose has been used as a traditional insulation material but the thermal conductivities ranging from 40 to 60 mW m⁻¹ K⁻¹ are insufficient to meet the current needs⁵². Previous studies have shown that anisotropic freeze-dried CNF foams can exhibit thermal conductivities below the super-insulating level, and thus compete with silica aerogels or other isotropic mostly supercritically dried foams and aerogels^{8,38}. This chapter describes the thermal conductivity and moisture uptake of anisotropic TCNF, CNF or CNC foams of varying diameters as a function of *RH*. Furthermore, moving towards the nanoscale, interfacial phonon scattering becomes very important, but has been poorly investigated, especially as a function of relative humidity. Moisture-induced swelling and the replacement of air with water in the pores control the thermal boundary conductance and the thermal conductivity of the foams. Other parameters such as the nanofibril/nanorod diameter, foam density, and temperature-dependent moisture uptake are also crucial to designing and tailoring insulation materials based on CNMs. Furthermore, to achieve minimal thermal conductivity, the importance of the gaseous or solid thermal conductivity contributions has to be assessed and evaluated.

4.1 Thermal Conductivity of CNF Foams as a Function of the Fibril Diameter and *RH* (Paper I)

Three grades of nanofibrils (Figure 20a) of varying charge densities and fibril diameters were prepared by TEMPO-mediated oxidation and mechanical grinding. Increasing the degree of carboxylation at C6 led to thinner fibrils of 2.3 nm and higher fibril aspect ratio (200 ± 16) while CNFs

that were only mechanically disintegrated (CNF₁₉) had a larger diameter of 19 nm and a lower aspect ratio ($=110 \pm 26$). The crystallinity index determined by XRD and the Segal method¹⁷⁸ seemed also to be higher for the CNF₁₉ compared to the TEMPO-oxidized fibrils (CNF_{2,3}, CNF_{4,4}).

The anisotropic foams were prepared by freeze-casting (Figure 20b) on plates of dry ice using a mold with a copper bottom and Teflon walls, which allowed unidirectional freezing from the bottom to the top. The fibrils were aligned along the freezing direction and the frozen material was freeze-dried to sublimate the water and obtain dry lightweight anisotropic foams (5.9–6.3 kg m⁻³). The foams had rather dense walls, consisting of nanosized pores, separated by tubular macropores. The alignment of the fibrils within the foam walls was confirmed by XRD experiments (Figure 20c) and SEM image analysis (see the SI of Paper I). The Herman's parameter ranged between 0.17 and 0.27 and the SEM image analysis showed an orientation of between 0.82 and 0.93. For both methods, the highest alignment was calculated for the CNF_{2,3} foam samples.

In the SEM images of the cross-section along the radial direction, the macropores resembled honeycomb structures (Figure 20d) especially for the CNF_{2,3} foams. The ability of the particles to pack in honeycomb structures, the interactions among the particles and the ice-crystal growth are the most dominant parameters that determine the final porous architecture from freeze casting^{183,184}. At low charge densities, van der Waals interactions among the nanocellulose particles overcome the repulsion forces during ice-templating, making the nanocellulose fibers aggregate and thus form foams with more disordered structure^{185,186}. On the other hand, as the charge density increases (i.e. at 1.6 mmol COO⁻ g⁻¹), a balance between the repulsive and van der Waals forces^{185,186} results in better packing and more ordered and denser foam walls. The balance between repulsion and van der Waals forces is confirmed from the BET surface area, which increased twofold from 8.7 for the CNF₁₉ to 15 m²/g for the CNF_{2,3} foams.

Furthermore, the HRSEM images (Figure 20e) confirm that the foam walls are dense and thin (≈ 200 nm). Combining the pore volume information measured by N₂ sorption, the density, and the porosity of the foam, it is possible to estimate the porosity of the foam walls. Therefore, according to Equation 19, the foam walls have low porosity of 3.5 to 5% at $RH = 0$.

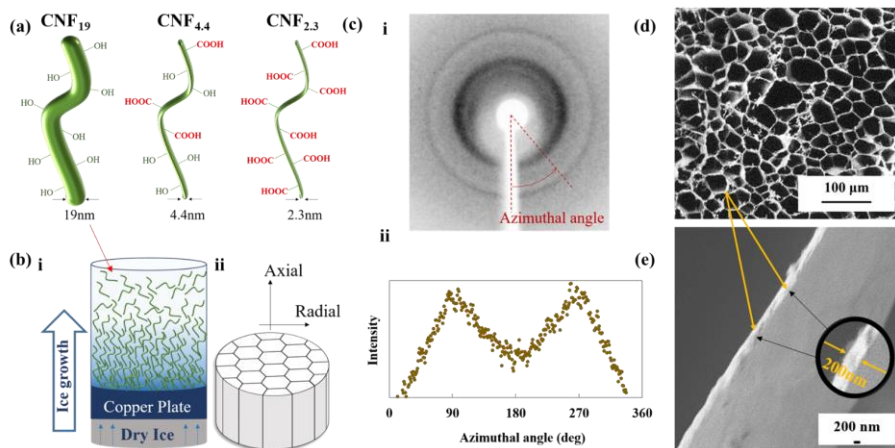


Figure 20. Preparation and structure of ice-templated anisotropic CNF foams. (a) Schematic illustration of the CNF morphology, diameter and surface chemistry. (b) Schematic representation of the ice-templating process: (i) the setup and mechanism; (ii) the highly aligned pores in the axial and the radial cross-sections. (c) X-ray diffraction investigation of CNF_{2.3} foams showing: (i) 2D diffraction pattern; (ii) azimuthal intensity profiles. (d) SEM image of the radial cross-section of the ice-templated CNF_{2.3} foams. (e) HRSEM image of a CNF_{2.3} foam wall. The Figure is taken from Apostolopoulou-Kalkavoura et al. 2021⁷¹.

The thermal conductivity of the anisotropic CNF foams was measured at 295 K and 5–80% RH at the customized measurement cell (Supplementary Information of Paper I) connected to the Hot Disk, the P2 Cellkraft humidifier and the silicone oil bath. Both the λ_r (Figure 21a) and axial λ_a thermal conductivities were determined in a single measurement in the anisotropic mode of the Hot Disk having as input the wet density (ρ_{wet}) and the wet specific heat capacity (C_{Pwet}). The C_P at dry conditions, determined by DSC, decreased with increasing charge density of the CNFs, from 1180 to 753 J kg⁻¹ K⁻¹ for CNF₁₉ and CNF_{2.3} foams, respectively (Supplementary Information of Paper I). The C_{Pwet} was calculated from Equation 13 by the rule of mixtures. The λ_r was much smaller (3–10 times) than the λ_a for the entire RH range examined, resembling the intrinsically anisotropic thermal conductivity of cellulose as the nanofibrils are aligned axially along the freezing front. Interestingly, two prior studies simulated the thermal conductivity of cellulose

I β crystals and single CNC particles, resulting anisotropy ratios of three and eight, respectively^{19,145}.

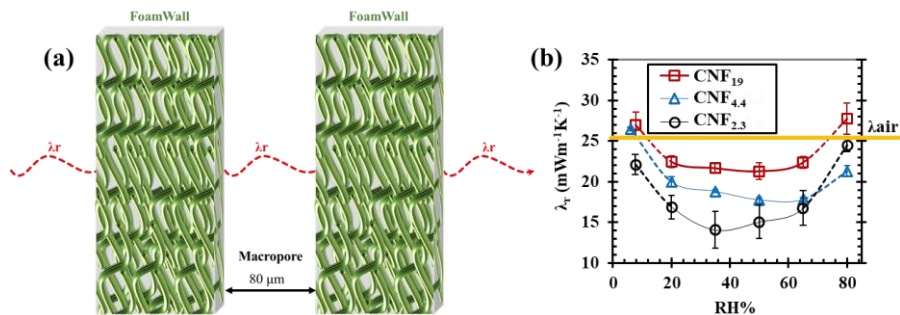


Figure 21. Thermal conductivity of anisotropic CNF foams. (a) Schematic illustration of the radial thermal conductivity (λ_r) across two foam walls. (b) Experimental λ_r of CNF_{2.3}, CNF_{4.4} and CNF₁₉ foams as a function of *RH* at 295 K. The Figure is modified from Apostolopoulou-Kalkavoura et al. 2021⁷¹.

In both directions, the thermal conductivities were strongly related to the *RH* and the fibril diameter. λ_a was proportional to *RH* (Supplementary Information of Paper I), confirming the effect of water as a more thermally conductive medium than air. However, λ_r remained below the thermal conductivity of air for almost the entire *RH* range tested and exhibited a three-step non-linear and unexpected *RH* dependency (Figure 21b), which was also reversible at least within 7 and 50% *RH* (See Figure 2b in Paper I). Specifically, λ_r of the anisotropic CNF foams decreased with increasing *RH* up to 35–50% *RH*, then stabilized in a narrow plateau at 50–65% *RH* before increasing with *RH* from 65 to 80% *RH*. The CNF_{2.3} foams were more anisotropic than the CNF_{4.4} and CNF₁₉ ones as they are made from the thinnest nanofibrils with the highest surface charge and aspect ratio, allowing them to pack and align more effectively. Therefore, the lowest thermal conductivity ($14 \text{ mW m}^{-1} \text{K}^{-1}$) was achieved at 35% *RH* for the CNF_{2.3} foam. The value of $14 \text{ mW m}^{-1} \text{K}^{-1}$ is more than $10 \text{ mW m}^{-1} \text{K}^{-1}$ lower than the value for air, which is surprising considering the presence of macropores in which the Knudsen effect is negligible. However, the foams exhibit a hierarchical pore structure consisting of both macro- and nanosized pores, thus the nanosized pores on the foam walls can both reduce the gaseous but also the solid

conduction contributions. The gas conduction is reduced as the mean free path of air molecules becomes very small in nanosized pores and the solid conduction may be also reduced as the nanopores can act as phonon scattering interfaces. The very low λ_r for the CNF foam with the smallest fibril diameter can be additionally explained by the fact that the smaller the fibril diameter, the more interfaces will be present within a foam wall and can act as diffuse phonon scattering sites.

4.2 Moisture Uptake and Swelling of CNF and TCNF Foams (Paper I)

To investigate more deeply the three-step non-linear dependency of λ_r on RH , the moisture uptake (Figure 22a) and degree of swelling (Figure 22b) were determined based on gravimetric moisture uptake and nitrogen sorption experiments. The increasing moisture uptake with increasing RH could explain the steady increase of the λ_a as a function of RH , but not the decreasing and plateau steps seen for λ_r .

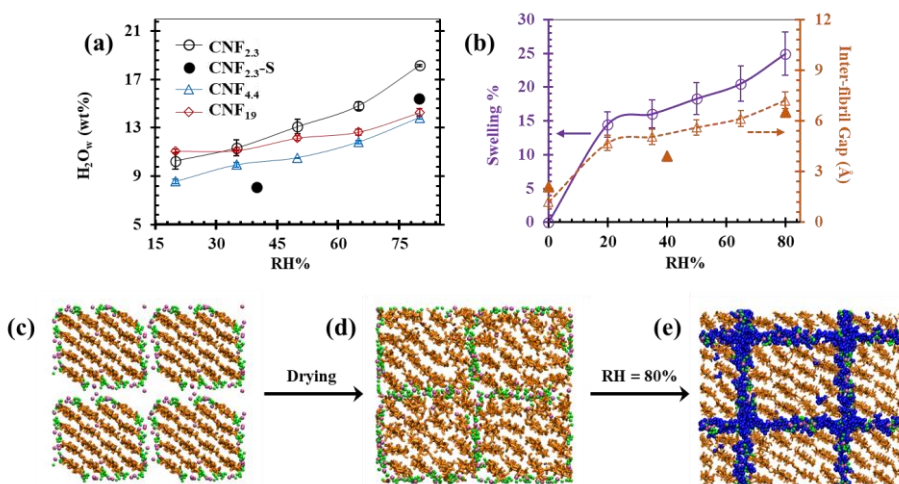


Figure 22. Experimental and hybrid GCMC/MD simulations of moisture uptake and foam-wall-sorption-induced swelling. (a) Experimental H_2O_w of ice-templated foams prepared from CNF_{2.3}, CNF_{4.4} and CNF₁₉ and the calculated by hybrid GCMC/MD simulation of H_2O_w for the CNF_{2.3} (CNF_{2.3}-S) as a function of $RH\%$ at 295 K. (b) The swelling percentage (continuous

line-○) in a CNF_{2.3} foam, the estimated average interfibril gap (dashed line-Δ) in a CNF_{2.3} foam and the calculated by hybrid GCMC/MD simulation interfibril gap (▲) as a function of *RH*%. (c) Initial arrangement of four individually equilibrated fibrils before drying. Snapshots of cellulose bundle of (d) aligned CNF_{2.3} fibril after the drying when they come close to each other and (e) the same fibrils subjected to *RH* that have swelled as water molecules have entered their interstitial sites. Cellulose chains are colored in orange, COO⁻ groups in green, counterions in pink and water in blue. The Figure is taken from Apostolopoulou-Kalkavoura et al. 2021⁷¹.

However, the increasing *RH* caused not only moisture uptake but also swelling. The swelling resulted in an increase of the nanoporosity fraction (Equation 19), from 5% at 0% *RH* to 24% at 80% *RH* for CNF_{2.3}, emerging and crowning the Knudsen effect at *RH* > 0. The swelling resulted in a greater interparticle distance which was quantified by Equation 27 and using the determination of the percentage of swelling in Equation 28.

$$g_i = \frac{\Pi_{np}}{(1-\Pi_{mp})} d_{CNF} \quad (27)$$

where Π_{np} is the *RH*-dependent nanoporosity (Equation 19) and d_{CNF} is the CNF diameter (Table 1). In detail, the fibril–fibril separation distance increased sharply at low *RH* (0→20%); from 1.2 to 4.7 Å for CNF_{2.3}, from 1.9 to 7.4 Å for CNF_{4.4} and from 6.8 to 37 Å for CNF₁₉. Between 20 and 80% *RH*, the increase in fibril–fibril separation distance was moderate, reaching the values of 7.4 Å for CNF_{2.3}, 10.8 Å for CNF_{4.4} and 46 Å for CNF₁₉ at 80% *RH*.

$$\%Sw = (1 - \Pi_{np0}) \times \left(\frac{g}{d_{CNF}} + 1 \right) - 1 \quad (28)$$

where Π_{np0} is the nanoporosity at *RH* = 0% (Equation 19). The foam wall swelling at 80% *RH* was around 20% for the CNF_{4.4} and CNF₁₉ foams and about 26% for the CNF_{2.3} foams, which corresponds to an estimated increase of the thickness of the foam wall from 200 to 250 nm in the latter case.

The percentage of swelling and the interparticle distance were also simulated using Grand Canonical Monte Carlo Simulation and Molecular Dynamics simulations (GCMC/MD). The configuration included a bundle of aligned cellulose fibrils, consisting of cellulose chains arranged in a Iβ crystal lattice with an approximately square cross-section (Figure 22c). The *RH* of the system was varied by changing the chemical potential (μ) of the system. The

four individually equilibrated fibrils with COO^- surface groups and Na^+ counterions came closer to each other upon drying (Figure 22d), whereas increasing the RH resulted in moisture uptake, swelling, and increase of the fibril–fibril interparticle distance (Figure 22e). Figures 22a-b show the relation of the theoretically calculated moisture uptake and interparticle distance to the ones from the molecular simulations for the $\text{CNF}_{2.3}$. The theoretical and the simulated values showed good agreement concluding that indeed the interparticle distance increases significantly at 80% RH .

4.3 Thermal Boundary Conductance of CNM Materials (Paper I)

To explain the mechanism of the non-linear radial thermal conductivity, the thermal boundary conductance (TBC) at the interface between two cellulose slabs, composed of chains organized in parallel, was estimated as a function of the interparticle distance and water content by non-equilibrium molecular dynamics (NEMD) simulations. Knowing the effect of the RH on the fibril–fibril separation distance based upon quantifying the swelling in Figure 22, the estimation of the TBC becomes very important.

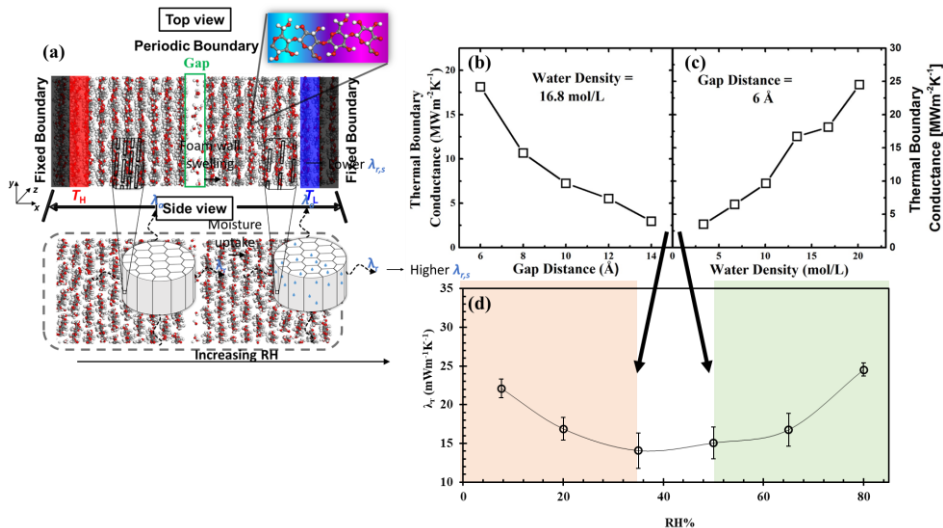


Figure 23. Thermal boundary conductance of cellulose nanofibrils. (a) Schematic of the system examined by NEMD simulation, showing top and

side views of two cellulose slabs separated by a gap with a variable distance. Fixed boundary conditions are applied along the x direction, while periodic boundary conditions are applied along the y and z directions. Thermal boundary conductance at room temperature estimated by NEMD simulations as (b) a function of gap distance at a water density of 16.8 mol L⁻¹ and compared with the λ_r of CNF_{2,3} for $RH < 35$, and (c) as a function of water density at gap distance of 6 Å and compared with the λ_r of CNF_{2,3} for $RH > 50$. (d) λ_r of the CNF_{2,3} foams separated in different areas. The Figure is adapted from Apostolopoulou-Kalkavoura et al. 2021⁷¹.

The system used in simulations resembled the aligned nanofibrils within a foam wall and the thermal boundary conductance was calculated by Equation 29.

$$TBC = -\frac{J}{\Delta T}, \quad (29)$$

where ΔT and J are the temperature difference and the heat flux across the interface, respectively. To simplify the calculations, the fibrils approaching the interfaces are modeled as single crystals.

The fibril–fibril separation distance ranged between 6 and 14 Å, values of the same magnitude as those calculated from both experimental data and molecular simulations (Figure 22b). Keeping the water density constant at 16.8 mol L⁻¹, the TBC decreased sixfold upon varying the separation distance from 6 to 14 Å, confirming the large effect of the increasing gap on the thermal properties (Figure 23b). On the other hand, keeping the separation distance constant at 6 Å, the TBC increased sixfold when the water density increased from 3.4 to 20.1 mol L⁻¹ (Figure 23c). Knowing the large effects of the increasing gap distance due to moisture-induced swelling and of the increasing water content between the fibrils, allows the behavior of the radial thermal conductivity as a function of RH (Figure 23d) to be understood based on a competing mechanism. This mechanism explains the decrease of the λ_r at $RH < 35\%$ due to the dominance of the increasing separation distance and the increase of the λ_r at $RH > 50\%$ due to the dominance of the increasing water content. As the gap distance increases at constant water density, phonon transmission decreases. Furthermore, reducing the water density while keeping the gap distance constant reduces even further the phonon transmission.

4.4 Density-dependent Thermal Conductivity of CNF Foams

We have shown that the strong effect of increasing RH on the λ_r of CNF foams is unexpectedly beneficial as the non-linear RH -dependence of λ_r is related to the reduction of the TBC by the increase in the moisture-induced interparticle separation distance and the increase of the TBC by the replacement of air with water. Moving one step further, the effect of increasing CNF density on the thermal conductivity is equally important when tailoring insulation materials.

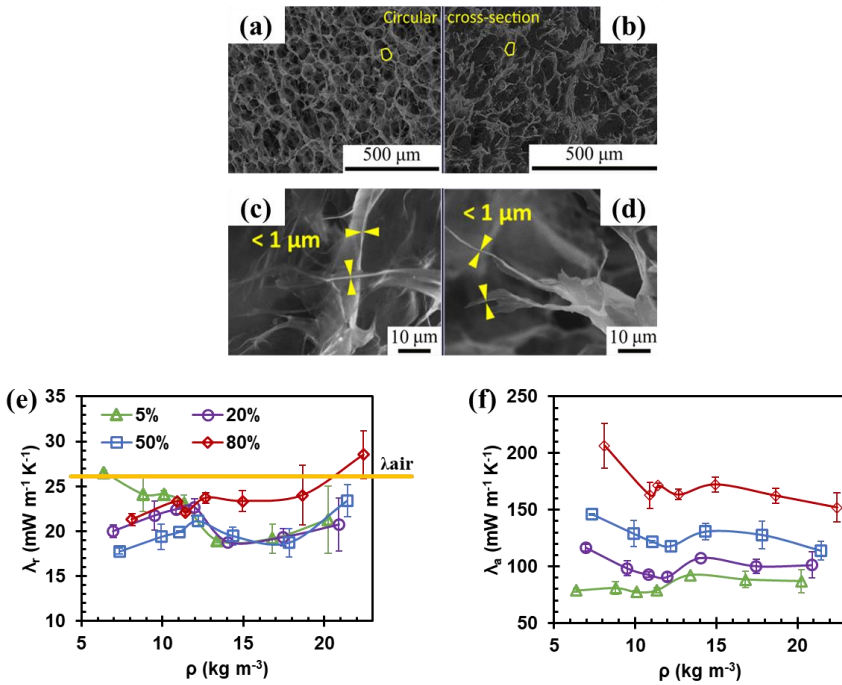


Figure 24. CNF_{4.4} foams with densities 6.4–20.2 kg m⁻³ obtained from dispersion containing 0.5–1.62 wt% CNF. SEM images showing the foam macropore cross-section of (a) 6.4 kg m⁻³ CNF_{4.4} foams and (b) 20.2 kg m⁻³ CNF_{4.4} foams. HRSEM images of the foam wall thickness of (c) 6.4 kg m⁻³ CNF_{4.4} foams and (d) 20.2 kg m⁻³ CNF_{4.4} foams. (e) Radial thermal conductivity (λ_r) and (f) axial thermal conductivity (λ_a) of CNF_{4.4} foams as a function of density at 5, 20, 50 and 80% RH and 295 K.

Figure 24 illustrates unpublished data for CNF_{4.4} foams at various densities. The CNF_{4.4} foams had honeycomb-like macropores (Figures 24-b) even at a density as high as 20.2 kg m⁻³ while the foam wall thickness remained <1 μm (Figures 24c-d). Both λ_r and λ_a changed very little with density (Figures 24e-f). λ_r remained below the super-insulating level over the density range tested, making it possible to obtain super-insulating CNF_{4.4} foams from dispersions with solid concentrations as high as 1.62 wt% despite the strong gelation of CNF above 1 wt% which makes it harder to process. λ_a also lay in a plateau, keeping the thermal anisotropy ratio rather constant as a function of density.

4.5 Density-dependent Thermal Conductivity of CNC Foams (Paper II)

The practicality of preparing CNF dispersions at higher concentration is limited by their viscoelasticity and low gelation concentration. Therefore, to study the influence of foam density on thermal conductivity over a wide range, we turned to CNC particles, which are processable in suspension at concentrations up to 10 wt%. CNC foams made from dispersions with concentrations below 2 wt% were rather fragile and were excluded from the study. The CNC used in this study were the commercial Celluforce CNC powder with diameters of 4.3 ± 0.8 nm and length of 173 ± 41 nm and having sulfate half-esters ($-\text{OSO}_3^-$) as surface groups and surface charge of 0.31 ± 0.01 mmol $\text{OSO}_3^- \text{ g}^{-1}$. Table 1 shows that dispersions containing 2–10 wt% CNC yielded solid foams with densities of 25–129 kg m⁻³.

Table 1. Dispersion concentrations used to produce dry CNC foams of various densities, as well as their reference names.

Dispersion concentration (wt%)	ρ_{dry} (kg m ⁻³)	Reference name
2	24.9	CNC ₂₅
2.5	28.4	CNC ₂₈
3	34.2	CNC ₃₄
3.5	40.1	CNC ₄₀

4.5	49.7	CNC ₅₀
5	51.9	CNC ₅₂
6	63.4	CNC ₆₃
7	70.3	CNC ₇₀
7.8	88.4	CNC ₈₈
8.9	97.2	CNC ₉₇
10.5	128.6	CNC ₁₂₉

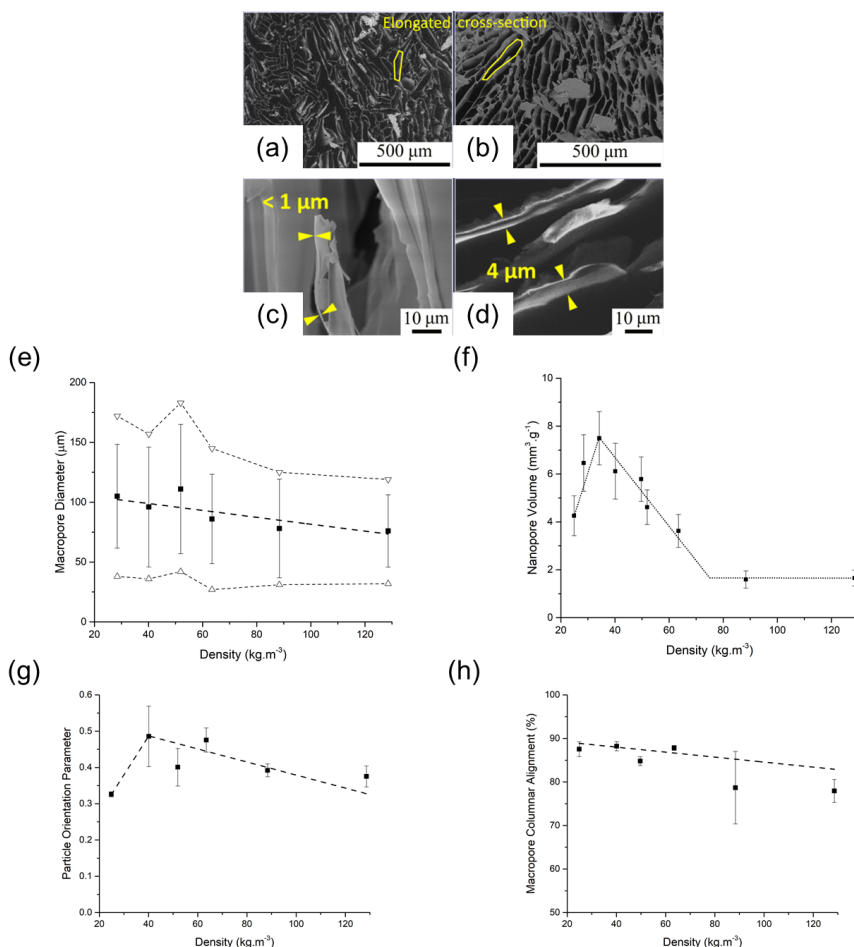


Figure 25. Morphological and structural characteristics of anisotropic CNC foams with densities 25–129 kg m⁻³. SEM images showing the foam macropore cross-sections of CNC foams with densities of (a) 40 and (b) 129 kg⁻³ CNC foams. HRSEM images of the foam wall thickness of CNC foams

with densities of (c) 40 and (d) 129 kg m⁻³. (e) Average macropore size as a function of foam density. (f) Nanopore volume measured by nitrogen sorption as a function of foam density. (g) Particle orientation parameter calculated by XRD 2D patterns as a function of foam density. (h) Macropore columnar alignment calculated by SEM image analysis as a function of foam density.

As illustrated in Figure 25, the dry foams obtained from CNCs exhibited lamellar structures with elongated oval macropores (Figures 25a-b). Furthermore, all foams were prepared using the same freeze-casting mold and have the same foam volume; increasing the solid concentration therefore resulted in more and thicker foam walls. These changes could not be quantified accurately from SEM images, but the relative changes in foam wall thickness are illustrated in Figures 25c-d. The porosity of the CNC foams ranged between 90.7 and 98.3 depending on the foam density, and the macropore size slowly decreased with increasing density from 38 to 32 μm (Figure 25e).

Similarly to the CNF foams in the previous chapter, the CNC foams displayed a hierarchical pore structure having not only macropores but also nanosized pores in the foam walls (Figure 25f). Nitrogen sorption experiments indicated that the nanopore volume (or surface area) generally decreased with increasing the foam density. The CNC foam wall porosity calculated using Equation 19 ranged between 0.3% and 1.3%. The better packing of CNC rods within the foam wall is once more confirmed by the much lower pore volumes or surface areas compared to the CNF foams of the previous chapter. However, there was a non-linear relationship between the pore volume and the density for the CNC₂₅₋₄₀ foams, with a maximum in nanoporosity that coincided with the onset of the chiral nematic phase. Far below the critical concentration, dispersed CNC rods rotate freely due to the very low viscosity and can therefore arrange and pack well in the foam walls. As the concentration surpasses 2 wt%, rotation is more hindered, blocking the efficient packing of rods and resulting in increasing foam wall nanoporosity. We observe then a compensation between the arrangement of the solid and gas fractions within the foams, which is expected to influence the thermal conductivity by the Knudsen effect in the small nanopores. The sizes of the nanopores are not influenced significantly by the foam density increase, being

between 9.2 and 11.4 nm with only the most dense CNC₁₂₉ foam having nanopores below 9 nm.

The particle orientation parameter estimated by XRD (Figure 25g) generally decreased with increasing density. However, CNC₄₀ foams differed slightly from the general trend, displaying a higher orientation parameter than CNC₂₅ foams. This probably happened because the CNC₂₅ foams were fragile and the particles did not pack efficiently in the foam walls. Similarly to the particle orientation parameter, the macropore columnar orientation displayed a decreased trend with increasing foam density (Figure 25h).

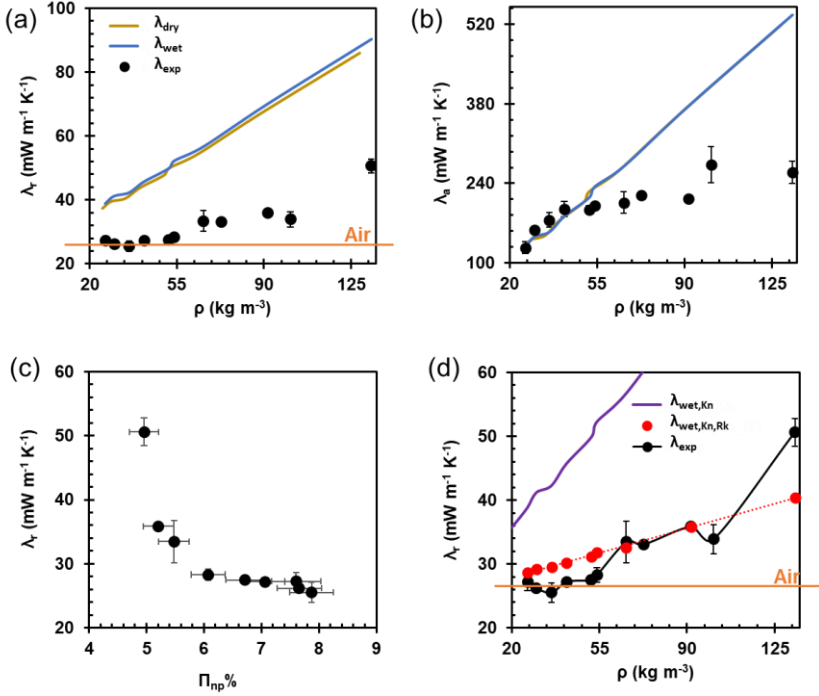


Figure 26. Thermal conductivity of anisotropic CNC foams as a function of density. (a) λ_r and (b) λ_a (experimental thermal conductivities, λ_{exp}) at 50% RH and 295 K and the theoretical estimations for dry (λ_{dry}) and wet CNC foams at 50% RH (λ_{wet}) with air confinement effects as a function of foam density. (c) λ_r as a function of nanoporosity at 50% RH and 295 K. (d) λ_r (experimental thermal conductivity, λ_{exp}) at 50% RH and 295 K and the theoretical estimation for wet CNC foams including air confinement effects (λ_{wet_Kn}) and phonon scattering ($\lambda_{wet_Kn_Rk}$).

Figure 26a and 26b display the λ_r and λ_a of CNC foams at 50% *RH*. Figure 26a shows that the λ_r of the CNC foams is divided into four distinct regions depending on their density. Interestingly, the first region includes a drop in the λ_r for CNC_{25–34}, reaching the low value of 25.5 and 24 mW m⁻¹ K⁻¹ at 50% (Figure 26a) and 20% *RH*, respectively, for CNC₃₄ (Supplementary Information of Paper II). The decreasing λ_r with increasing density can be related to the increasing particle alignment (Figure 25g) and nanoporosity or nanopore volume (Figure 25f) observed in same density range (CNC_{25–34}). The nanoporosity was highest (1.3% at 5% *RH* and 7.9% at 50% *RH*) for CNC₃₄, which had the lowest λ_r (Figure 26c), confirming the influence of the Knudsen effect in the nanopores. λ_r was relatively constant at 27–28 mW m⁻¹ K⁻¹ CNC_{40–52} at 50% *RH*, then gradually increased with increasing density, reaching the high value of 51 mW m⁻¹ K⁻¹ at 50% *RH* for CNC₁₂₉ foams. Similar trends have been observed for 5%, 20% and 80% *RH* (Supplementary Information of Paper II).

λ_a generally increased with increasing density, passing through a first increase, a plateau, and a final increase. The first increase occurred for CNC_{25–40}, coinciding with the increase in the particle alignment within the same range and the onset of the chiral-nematic phase in the starting dispersions. We speculate that the onset of the chiral-nematic phase locks the particles in certain configurations, causing losses in the particle and macropore orientation (Figure 25g,h) that result in a plateau area for λ_a . The final increase is a result of more solid material due to significant density increase, less nanoporosity and the further loss in the alignment.

To further evaluate the thermal conductivity contributions, we attempted to predict the theoretical thermal conductivity by a simple model. We assumed that the particles were perfectly aligned along the axial direction. Then, as first step represented by the ' λ_{dry} ' in Figures 26a-b, we have added the contributions for bulk solid conduction which equals the thermal conductivity of cellulose ($\lambda_{cell} = 720$ mW m⁻¹ K⁻¹ and 5700 mW m⁻¹ K⁻¹ for the radial and axial directions¹⁵⁵) and air conduction without considering air confinement effects ($\lambda_{air} = 25.6$ mW m⁻¹ K⁻¹ at 295 K), multiplied by their volumetric fractions (φ_{wall} for the solid and φ_{air} for the air conduction contribution); see Equation 30.

$$\lambda_{dry} = \lambda_{cell} \cdot \varphi_{wall} + \lambda_{air} \cdot \varphi_{air} \quad (30)$$

The second step, ' λ_{wet} ', includes the addition of the water contribution ($\lambda_{H_2O} = 601 \text{ mW m}^{-1} \text{ K}^{-1}$) at 50% *RH* multiplied by its volumetric fraction (ϕ_{H_2O}); see Equation 31.

$$\lambda_{wet} = \lambda_{cell} \cdot \phi_{cell} + \lambda_{air} \cdot \phi_{air} + \lambda_{H_2O} \cdot \phi_{H_2O} \quad (31)$$

Neither λ_{dry} nor λ_{wet} reproduced well the experimental thermal conductivities in the radial (Figure 26a) or axial (Figure 26b) directions. The values in the axial direction seem to have a closer correlation to the experimental data but the deviation is greater as the density increases probably due to the orientation and alignment loss.

The third step, ' λ_{wet_Kn} ' (Figure 26d) includes the division of the gas conduction into the macropore (λ_{mp}) and nanopore (λ_{np}) contributions, multiplied by their volumetric fractions (ϕ_{mp} for the macropores and ϕ_{np} for the nanopores); see Equation 32.

$$\lambda_{wet_Kn} = \lambda_{cell} \cdot \phi_{cell} + \lambda_{mp} \cdot \phi_{mp} + \lambda_{np} \cdot \phi_{np} + \lambda_{H_2O} \cdot \phi_{H_2O} \quad (32)$$

The gaseous contribution of the macropores and nanopores was estimated by Equations 33–34.

$$\lambda_{mp \text{ or } np} = \frac{\lambda_{go}}{1 + 2\beta Kn} \quad (33)$$

where λ_{go} is the thermal conductivity of air in free space, β is a characteristic number (=2 for foams and aerogels), and Kn is the Knudsen number (mean free path of air molecules (Equation 34) divided by the pore size⁴³.

$$I = \frac{1}{\sqrt{2} \times \frac{P_{amb} \times \pi \times d_{air}^2}{k_B \times T} + \frac{S \times \rho}{\pi}} \quad (34)$$

Where P_{amb} is the pressure, d_{air} is the diameter of the air molecule, S is the specific surface area, ρ is the foam density, k_B is Boltzmann's constant and T the temperature.

The very high Knudsen number (=2.5–6) in a nanopore results in values for λ_{np} that are below $2.2 \text{ mW m}^{-1} \text{ K}^{-1}$ for all foam samples over the whole *RH* range; however, due to their relatively small volume fraction, the nanopores have a negligible effect on the effective thermal conductivity according to the theoretical estimation.

For the radial thermal conductivity, knowing the average particle diameter and the interfacial resistance, is it possible to also consider phonon scattering

at the particle–particle interfaces. In this case, the solid conduction contribution (λ_p) can be estimated by Equation 35.

$$\lambda_p = \frac{\lambda_{cell}}{1 + \lambda_{cell} \frac{R_K}{d}} \quad (35)$$

where λ_{cell} is the thermal conductivity of CNC ($\lambda_{cell} = 720 \text{ mWm}^{-1} \text{ K}^{-1}$), R_K is the Kapitza or interfacial thermal resistance³⁹ and d is the CNC diameter. The interfacial thermal resistance (g_i/λ_i) is estimated by Equation 36¹⁵⁵:

$$\frac{g_i}{\lambda_i} = \frac{d_t}{\lambda_t} - 2 \frac{d}{\lambda_{cell}} \quad (36)$$

where g_i is the gap distance between two adjacent CNC particles, λ_i is the interfacial thermal conductivity, d is the diameter of a CNC particle, λ_{cell} is the thermal conductivity of a CNC particle, d_t is the total width of two adjacent CNC particles and their gap distance and λ_t is the equivalent thermal conductivity contribution of two CNC particles and their gap distance. λ_{cell} and λ_t are calculated by Diaz et al.¹⁵⁵ for CNC particles and we assume they are similar for our system as the diameter of the CNC particles is of similar magnitude. Of course, this is a rough estimation that could be improved by directly measuring the interfacial resistance.

The fourth step then (Figure 26c) can be calculated by Equation 37.

$$\lambda_{wet_Kn_Rk} = \lambda_p \cdot \varphi_{cell} + \lambda_{mp} \cdot \varphi_{mp} + \lambda_{np} \cdot \varphi_{np} + \lambda_{H2O} \cdot \varphi_{H2O} \quad (37)$$

The addition of the interfacial resistance in the calculation of the contribution of solid conduction to thermal conductivity allowed the experimental radial thermal conductivities to be reproduced more closely. We have not included the interfacial resistance in the calculation of the axial thermal conductivity because it is hard to estimate the gap distance axially and the Diaz value corresponds more to the radial direction due to the small diameter of the CNC particles rather than their greater length.

The quantity ‘ $\lambda_{wet_Kn_Rk}$ ’ (Equation 37) greatly underestimated the experimental radial conductivity of the CNC₁₂₉ foam, probably due to the alignment and orientation loss or even the higher foam wall thickness, which were not considered in the theoretical estimation.

Figure 27 illustrates the potentially significant contributions to the changes in thermal conductivity of CNC foams as a function of the foam density. Phonon scattering in the solid-solid interfaces is the main mechanism that was confirmed by theoretical calculations to significantly decrease the λ_r .

However, when the separation distance (g) between adjacent CNC particles becomes very small at high solid contents and thicker foam walls (i.e. CNC₁₂₉), the thermal conductivity inevitably increases due to the creation of phonon bridges. Furthermore, the Knudsen effect in the nanopores that showed minimal influence according to the calculations, but the lowest λ_r was achieved for the foam with the maximum nanoporosity (i.e. CNC₃₄) is also important.

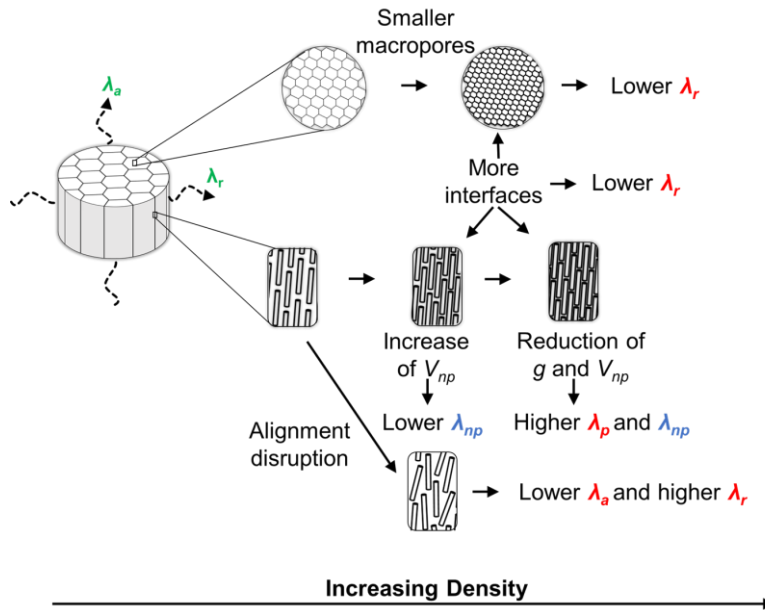


Figure 27. Schematic illustration of the main parameters that influence thermal conductivity.

The theoretical estimations do not take into consideration the phonon scattering at the solid/air boundaries, which is expected to increase with increasing density as there are more foam walls and smaller macropores. Factors such as the particle alignment, the macropore columnar orientation and the foam wall thickness are also disregarded from the theoretical estimations but their contributing role to the effective thermal conductivity can potentially explain the deviations at high CNC foam densities.

4.6 Moisture Uptake as a Function of RH, Temperature and Crystallinity (Paper III)

As climatic conditions vary around the globe, the ability to scale up the use of cellulosic materials as insulators depends crucially on understanding how moisture uptake at different RH and temperature affects cellulosic materials with different crystallinity indices and surface modifications. TCNF and TCNC having the same charge density and surface chemistry but different crystallinity were prepared by TEMPO-mediated oxidation and HCl hydrolysis. The TCNF and TCNC foams were prepared as described before by freeze-casting 0.5 wt% dispersions. The TCNC foams were 33% more crystalline than the TCNF foams while the surface charge remained unchanged. To examine the effect of surface modification on the moisture uptake of CNM foams, CMCNF nanofibrils were also used to prepare dry foams.

Table 2. CNM particles and foams.

	Surface Groups	Surface Charge (mmol COO ⁻ g ⁻¹)	Particle Diameter (nm)	Crystallinity Index (CI)
TCNF	–COO ⁻	1.60 ± 0.01	2.3 ± 0.7	51.1
TCNC	–COO ⁻	1.60 ± 0.01	4.5 ± 1.3	67.8
CMCNF	–CH ₂ COO ⁻	0.65 ± 0.00	3.0 ± 0.6	45.8

The moisture uptake of the dry foams was then measured gravimetrically in a humidity chamber at 285, 295, 303, 308 and 313 K and 20–80% RH (Figure 28). Furthermore, the moisture uptake was calculated by hybrid Grand Canonical Monte Carlo and Molecular Dynamics simulations for crystalline cellulose bundles and amorphous cellulose films having the same surface modification as the raw materials used to prepare the foams. Figure 28a,b shows that the experimental gravimetric moisture uptake of partially crystalline TCNF, TCNC and CMCNF foams lies between the moisture

uptake estimated by molecular simulations for an amorphous cellulose film and crystalline cellulose bundles of the same composition and surface charge. The CMCNF foams took up less moisture than the more crystalline TCNF foams, but a direct comparison is hard as they have different surface charge.

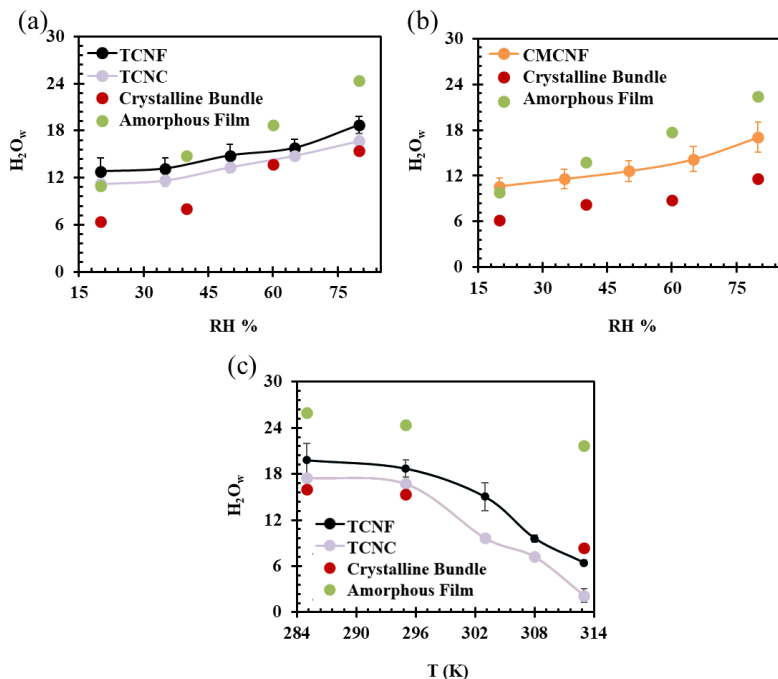


Figure 28. Experimental moisture uptake of CNM foams combined with hybrid Grand Canonical Monte Carlo and Molecular Dynamics simulations. (a) Moisture uptake by mass as a function of RH at 295 K for TCNF and TCNC foams as well as for simulated TEMPO-modified crystalline cellulose bundles and TEMPO-modified amorphous cellulose film. (b) Moisture uptake by mass as a function of RH at 295 K for CMCNF foams as well as for simulated carboxymethylated crystalline cellulose bundles and carboxymethylated cellulose amorphous film. (c) Moisture uptake by mass as a function of temperature at 50% RH for TCNF and TCNC foams as well as for simulated TEMPO-modified crystalline cellulose bundles and TEMPO-modified amorphous cellulose film.

The higher crystallinity of TCNC resulted in lower moisture uptake than TCNF foams. Similarly, the moisture uptake of the amorphous cellulose film

was always significantly higher than that of the crystalline cellulose bundles, confirming that more crystalline celluloses inhibit moisture uptake to a certain extent, and are naturally more hydrophobic^{152,187}. In all foam and simulated samples, the moisture uptake increased with increasing *RH* due to the increase in the chemical potential of water.

Furthermore, as the temperature rose, the moisture uptake gradually dropped (Figure 28c) due to the decreasing chemical potential of water. At temperatures up to 295 K the standard deviation between the experiments and simulations was lower than at temperatures between 303–313 K. The higher deviation at higher temperatures can be explained by the presence of bound water which becomes more significant as the moisture uptake is lower.

Going one step further to explain the decreasing moisture uptake with increasing temperature, our collaborators examined the morphological changes within the cellulosic simulated samples. The pores are larger and the pore distribution wider for the TEMPO-modified amorphous cellulose film compared to the TEMPO-modified crystalline cellulose bundles (See Figure 4 in Paper III). The smaller pores of the crystalline bundles did not allow water penetration, confirming the lower moisture uptake of more crystalline samples. For the TEMPO-modified amorphous cellulose film the pore size distribution becomes narrower as temperature increases, explaining the decreasing moisture uptake at higher temperatures. On the other hand, the crystalline bundles, being rigid, exhibited similar pore size distributions over the entire temperature range.

Furthermore, the distribution function $g_{O^-OW}(r)$ as a function of the distance between the oxygen (O^-) located in the carboxyl of cellulose and the oxygen (OW) located in the water was investigated (See Figure 4 in Paper III). For both the TEMPO-modified amorphous cellulose film and the TEMPO-modified crystalline bundle, the distance between the two oxygens peaked at 3 Å, representing the hydration shells around the oxygen in the carboxyl group. While the distribution function $g_{O^-OW}(r)$ was almost constant with temperature for the TEMPO-modified amorphous cellulose film, it changed significantly for the TEMPO-modified crystalline bundles. The increasing distribution function $g_{O^-OW}(r)$ with decreasing temperature for the TEMPO-modified crystalline bundles shows that the amount of absorbed water molecules in the crystalline bundle decreased with decreasing temperature. However, the amount of water around the TEMPO-modified amorphous

cellulose film remained unchanged as a function of temperature. The carboxymethylated crystalline bundles and amorphous film show the same behavior and the results are summarized in the SI of Paper III.

Thus, pore size decreases with increasing temperature in amorphous samples, whereas the amount of absorbed water molecules decreases with increasing temperature in crystalline samples. The two mechanisms together result then in reduced moisture uptake at higher temperatures in all cases, making the cellulosic foams potentially good alternatives for thermal insulation even at high temperatures.

4.7 Conclusions

The thermal conductivity of anisotropic nanocellulose foams, directly or indirectly, is influenced by the chemical pre-treatment, moisture uptake, foam density and crystallinity of CNC and CNF foams. The intrinsic anisotropy of cellulose results in anisotropic CNM foam structures with anisotropy ratios greater than 3.

The radial thermal conductivity perpendicularly to the particles' direction can be as low $14 \text{ mW m}^{-1} \text{ K}^{-1}$ at 295 K and 35% *RH* for the CNF_{2,3}, which is much below the super-insulating level. TEMPO-mediated oxidation tunes the CNF diameter and aspect ratio, which is crucial in tuning the thermal conductivity. CNF_{4,4} foams within the density range of $6\text{--}20 \text{ kg m}^{-3}$ were super-insulating. The thinner the diameter of the CNM particles, the more phonon diffuse scattering can occur at the interfaces, which reduces the solid conduction. The radial thermal conductivity varied non-linearly with *RH* and moisture uptake. NEMD simulations indicated that the thermal conductivity of the hygroscopic CNF foams is influenced by the competing mechanisms of increased phonon scattering due to moisture-induced swelling and increasing moisture content. Swelling at *RH* up to 35-50% influences the solid conduction by disrupting the heat path and enhancing the interfacial phonon scattering. Furthermore, the increased fraction of wall nanoporosity is expected to reduce the gas conduction contribution due to the Knudsen effect. The increasing moisture uptake at *RH* > 50% will increase the thermal conductivity as water is more conductive than air.

CNC foams made from dispersions with solid contents between 2 and 10.5 wt% were used to study the effect of foam density on thermal conductivity over a wide range of densities. Analysis of the effective thermal conductivity by summing up various contributions demonstrated that the phonon scattering at the solid-solid interfaces was the most dominant factor that suppressed the radial thermal conductivity. Nanoporosity, which was expected to strongly reduce radial thermal conductivity due to the Knudsen effect, actually had minimal influence according to the theoretical calculations due to the low volumetric fraction of nanopores. Furthermore, parameters such as the alignment, the foam wall thickness and the phonon scattering at the solid-air boundaries were also expected to have an influence, but they were not included in the simplified theoretical models. The lowest radial thermal conductivity for CNC foams ($24\text{--}26\text{ mW m}^{-1}\text{ K}^{-1}$ at 295 K and 20–50% *RH*) was achieved for CNC₃₄ foams which also had the maximum nanoporosity.

Foams based on highly crystalline CNM particles are characterized by low moisture uptake which can be beneficial for many applications. Molecular simulations in combination with experimental measurements showed that increasing the temperature results in decreasing moisture uptake which may be beneficial when using CNM foams in hot and humid climatic conditions. The cause of the lower moisture uptake at higher temperatures depends on the reduced chemical potential of water and the decreasing pore size in the amorphous cellulose films, or the decreasing water content around the oxygen of the carboxyl group in the crystalline cellulose bundles.

5 Thermal Conductivity of Isotropic Foams (Papers IV and V)

Although cellulose is strongly anisotropic, traditionally there are many more studies tailoring isotropic thermally insulating materials, due both to their lower structural complexity and the ease of directly comparing their performance with the current mostly fossil-based thermal insulation materials. Apart from thermal insulation in buildings, isotropic foams are excellent choices for packaging applications, which require thermal conductivities to be low, but not necessarily below the super-insulating level. The isotropic CNM foams or aerogels are usually prepared by either SCD, FD or ED, resulting in different porous structures that strongly impact heat transfer both in the solid and the gas phase. This chapter characterizes the thermal conductivity and moisture uptake of CNF–polyoxamer foams, which are made by foaming and ED in an oven, over a wide range of temperatures (261–314 K) and *RH* (2–80%). The CNF–polyoxamer foams could be then directly compared with EPS over the same range of *T* and *RH*. Furthermore, this chapter explains a modified empirical model which fits the thermal conductivity data and predicts the thermal conductivity even at high-moisture conditions. As an attempt to compare the CNF–polyoxamer foams with other CNF-based isotropic foams, this chapter includes the thermal conductivity and moisture uptake characterization of CNF–MOF foams which are made by FD. Most studies on thermal insulation materials based on cellulosic components have disregarded the impact of moisture uptake which makes it difficult to compare and design the proper materials. Therefore, measuring thermal conductivity at different climatic conditions is very important to be able to upscale the production of cellulose/CNM based foams and aerogels.

5.1 Thermal Conductivity and Moisture Transport Properties of Isotropic CNF-Nonionic Polyoxamer Foams (Paper IV)

CNF–(nonionic) polyoxamer foams (Figure 29a) were prepared by foaming Pluronic P123, crosslinking the CNF with Ca^{2+} , and oven drying at

60 °C. The foams had a final dry composition of 46.3 wt% CNF, 32.4 wt% P123, 4.6 wt% CaCO₃ and 16.7 wt% GDL, a low density of $11.9 \pm 1.2 \text{ kg/m}^3$ and porosity of 99%. The foams exhibited a closed macropore structure (Figure 29b) with low foam wall porosity as confirmed by the low specific surface area ($1\text{--}2 \text{ m}^2/\text{g}$) and average macropore size of $145 \pm 46 \text{ }\mu\text{m}$ ⁷⁵.

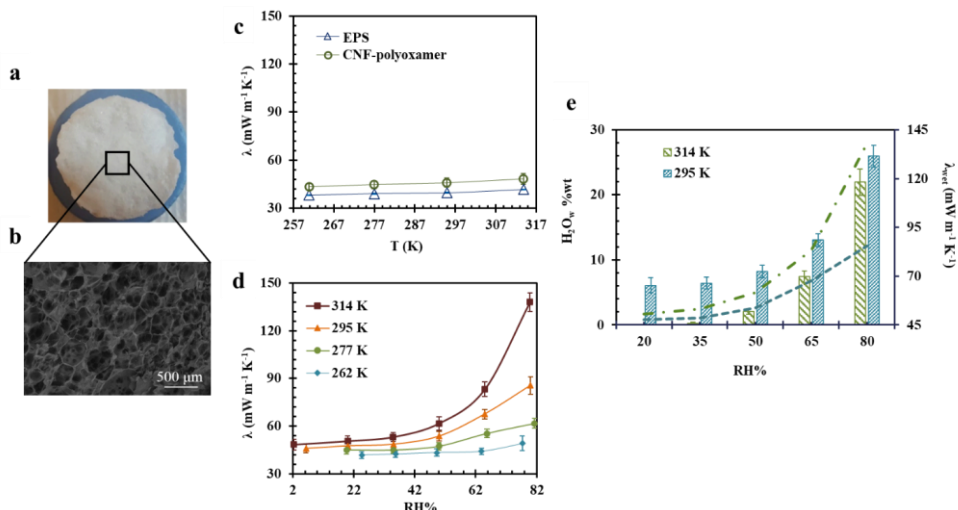


Figure 29. CNF–(nonionic) polyoxamer foams. (a) Picture of the solid foam. (b) SEM image of the porous structure of the foam. (c) Thermal conductivity (λ) of CNF-based foams and EPS foam as a function of temperature at constant absolute humidity ($AH = 1.19 \pm 0.1 \text{ g H}_2\text{O m}^{-3} \text{ air}$); (d) Thermal conductivity (λ) of CNF-based foams as a function of the RH at 314, 295, 277 and 262 K. (e) H_2O_w , (wt %) (histogram) and thermal conductivity of the CNF-based foams as a function of the RH at 314 and 295 K. Figures are taken and modified from Apostolopoulou-Kalkavoura et al. 2018¹¹⁴.

Interestingly, the thermal conductivity of CNF–polyoxamer foams, which ranged between 43 and $48 \text{ mW m}^{-1} \text{ K}^{-1}$, was very similar to the EPS foams at low absolute humidity ($1.18 \pm 0.1 \text{ g H}_2\text{O /m}^3 \text{ air}$) deviating by only $5\text{--}7 \text{ mW m}^{-1} \text{ K}^{-1}$ (Figure 28c). The thermal conductivity of the EPS foams was identical to the standard value given by the manufacturer ($38 \text{ mW m}^{-1} \text{ K}^{-1}$), confirming the validity of the thermal conductivity measurements performed in the customized setup. Furthermore, the experimental values for the CNF–polyoxamer foams

were well correlated with the thermal conductivity of cellulosic or other biopolymer foams^{52,59,95}. The temperature dependence of the CNF–polyoxamer foams increased moderately by 11% increasing the temperature from 257 to 317 K, resembling the temperature dependence of other porous materials such as wood¹⁰⁵, fireboard¹⁰⁵, expanded glass granules, foam glass gravel¹⁸⁸, polystyrene^{105,189} and polyurethane foams^{53,92}. However, the thermal conductivity of CNF–polyoxamer foams increased significantly with increasing *RH*, especially at *T* above 295 K (Figure 29d). The exponential increase of the λ_{wet} reached 86 mW m⁻¹ K⁻¹ at 80% *RH* and 295 K and 138 mW m⁻¹ K⁻¹ at 80% *RH* and 314 K. Other hygroscopic materials such as wood, concrete or expanded glass granules^{97,190–192} exhibit similar thermal conductivity as a function of increasing *RH*, confirming the importance of controlling carefully the climatic conditions. Therefore, we measured the moisture uptake gravimetrically (Figure 29e) and observed a strong dependence on the *RH*. The moisture uptake increased from 0.26 ± 0.16% at 314 K and 35% *RH* to 6.44 ± 0.94% at 295 K and 35% *RH*. Considering the very high thermal conductivity of water (600 mW m⁻¹ K⁻¹) compared to air (25.7 mW m⁻¹ K⁻¹), the thermal conductivity increased similarly as the axial thermal conductivity in case of anisotropic materials. However, as has been discussed in the previous section, the moisture uptake decreased with increasing temperature as it has been observed for other polysaccharides, such as chitosan¹⁹³, starch¹⁹⁴, and potato¹⁹⁵.

5.2 Modelling of the Thermal Conductivity of Hygroscopic Foams (Paper IV)

Künzel et al.^{97,190} attempted to model the exponential dependence of the thermal conductivity on the moisture uptake for various hygroscopic building materials such as cement and wood. Figure 30a shows the non-linear dependence of the λ_{wet} of CNF–polyoxamer foams on the moisture content by volume described in Künzel's empirical model (Equation 38).

$$\lambda_{wet} = \lambda_{dry} * \left(1 + \frac{b * H_2O_{vl}}{\rho_{dry}}\right) \quad (38)$$

where, λ_{dry} is the dry thermal conductivity of the foam, *b* is the dimensionless moisture supplement, H_2O_{vl} is the foam volumetric water content, and ρ_{dry} is the dry foam density. Here, *b* was set to 1.5 in analogy to that for wood,^{97,190} changing *b* within the range 0.5–5 did not improve the fit to the Künzel model.

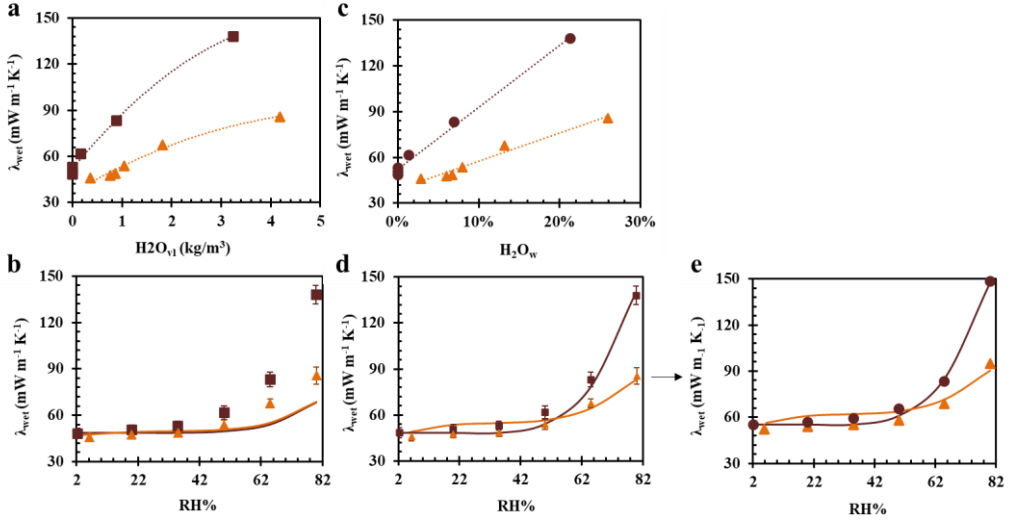


Figure 30. Künzle et al. vs empirical modelling. (a) Experimental wet thermal conductivity values (λ_{wet}) of CNF–polyoxamer foams as a function of volumetric moisture content. (b) Fitting of the experimental wet thermal conductivity values (λ_{wet}) of CNF-based foams to the equation proposed by Künzle et al. ^(97,190) as a function of RH at 314 and 295 K. (c) Experimental wet thermal conductivity values (λ_{wet}) of CNF–polyoxamer foams as a function of gravimetric moisture content. (d) Fitting of the experimental wet thermal conductivity (λ_{wet}) of the 11.9 kg/m³ CNF–polyoxamer foams calculated by Equation 39 as a function of RH at 314 and 295 K. (e) Fitting of the experimental wet thermal conductivity values (λ_{wet}) of the 28.8 kg/m³ CNF–polyoxamer foams calculated by Equation 39 as a function of RH at 314 and 295 K. Figures are taken and modified from Apostolopoulou-Kalkavoura et al. 2018¹¹⁴

Equation 38 significantly underestimated the thermal conductivity of the CNF–polyoxamer foams (Figure 30b). Therefore, we attempted to correlate the experimental λ_{wet} to the moisture content by mass (Figure 30c) and found a linear dependency from which we derive the relationship between λ_{wet} and the moisture content by mass shown in Equation 39 (Figure 30d-e).

$$\lambda_{wet} = \lambda_{dry} \times \left(1 + \gamma(T) \times \frac{H_2O_{vl}}{\rho_{dry} + H_2O_{vl}} \right) \quad (39)$$

where, H_2O_{vl} divided by $\rho_{wet} = \rho_{dry} + H_2O_{vl}$ is the water content by mass H_2O_w , and $\gamma(T)$ is a temperature-dependent supplement. Equation 39 was used to calculate the theoretical λ_{wet} at 295 K and 314 K for both 11.9 and 28.8 kg m⁻³ CNF–polyoxamer foams, confirming its validity at both temperatures and foam densities. The root-mean-square error (RMSE) between the theoretical and experimental λ_{wet} was below 1.93 over the entire RH range tested at both 295 and 314 K. The motivation behind this attempt was the much lower water vapor resistance factor of the CNF–polyoxamer foams (0.1–1 at 295–314 K) than common building materials such wood and concrete, showing the different moisture uptake mechanism. Furthermore, λ_{wet} depends more strongly on wet density for low-density materials such as the CNF–polyoxamer foams.

5.3 Thermal Conductivity and Moisture Resistance of CNF and Al-MIL-53 Aerogels (Paper V)

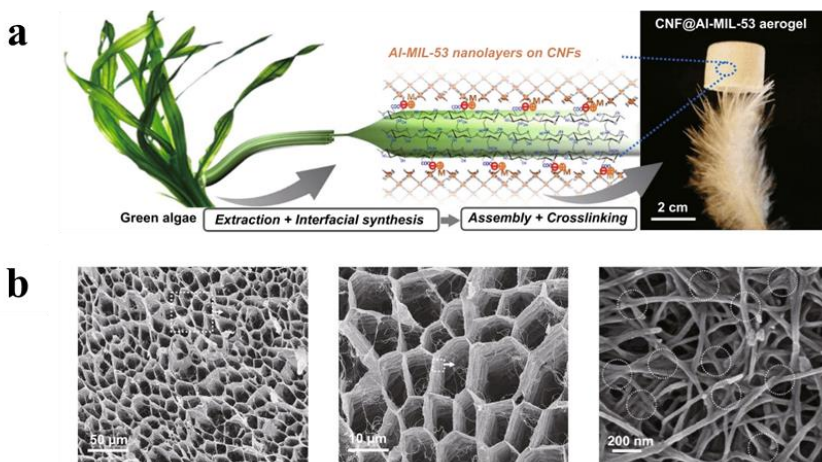


Figure 31. CAM aerogels. (a) CNF extracted from *Cladophora* cellulose to prepare dry CAM foams following an interfacial synthesis, freeze-drying, and crosslinking route. (b) The hierarchical porous structure of CAM aerogels displayed in SEM images at different lengthscales. Images taken from Zhou et al. 2020⁶⁹.

Low-density CAM aerogels ($\approx 3 \text{ kg m}^{-3}$) were prepared by TCNF extracted from *Cladophora cellulose* and Al-MIL-53 (Figure 31a), an aluminum-based MOF, by an interfacial synthesis, freeze-drying and crosslinking to obtain a CAM aerogel containing 30 wt% Al-MIL-53. The foams featured hierarchical structure combining interconnected macropores, micropores and mesopores (Figure 30b).

The thermal conductivity of the CAM aerogels was investigated in the Hot Disk 2500 thermal constants analyzer at 295 K and 5–80 % *RH* (Figure 32a). At 5% *RH* and 295 K, the thermal conductivity of pure AL-MIL-53 pellets was more than five times the thermal conductivity of the pure CNF or the CAM aerogel. Furthermore, the difference between the CNF and CAM aerogels was negligible, with the CAM aerogel reaching the value of $41 \text{ mW m}^{-1} \text{ K}^{-1}$ (Figure 32a).

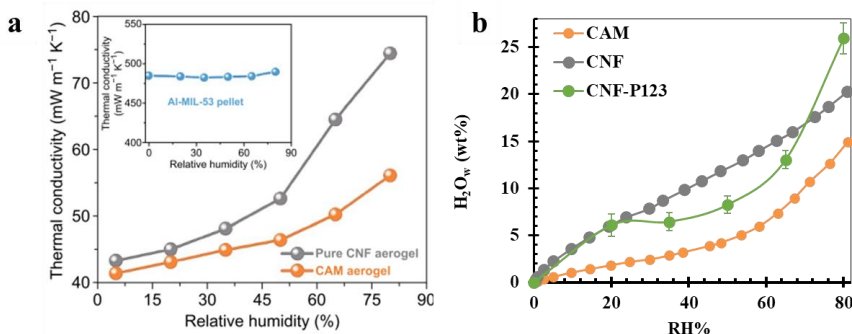


Figure 32. Thermal conductivity and moisture resilience of CAM aerogels. (a) Thermal conductivity of pure CNF and CAM aerogels as a function of *RH* at 295 K. (b) Moisture uptake of CAM, CNF and CNF-P123 aerogels between 0 and 80% *RH* at 295 K. Images modified from Zhou et al. 2020⁶⁹ and Apostolopoulou-Kalkavoura et al. 2018¹¹⁴.

The CAM aerogels exhibit 11% lower thermal conductivity than the CNF–polyoxamer foams, probably due to the CAM’s hierarchical porous structure and the hydrophobic nature of the AL-MIL-53. At 295 K, the thermal conductivity of the CAM aerogel increased with *RH*, reaching a value of $55 \text{ mW m}^{-1} \text{ K}^{-1}$ at 80% *RH*, a 34% increase compared to 5% *RH* (Figure 32a). The increase in thermal conductivity with *RH* was much lower in CAM aerogels than in the pure CNF aerogel, whose thermal conductivity rose 72%

from 5 to 80% *RH*. Similarly, the thermal conductivity of the CNF–polyoxamer foams increased 87% from 5 to 80% *RH* at 295 K. Figure 32b confirms that the CAM aerogels adsorbed 27% less moisture than pure CNF aerogels and 43% less moisture than the CNF–polyoxamer foams at 80% *RH* and 295 K.

5.4 Conclusions

The thermal conductivity of isotropic CNF–polyoxamer foams showed a small temperature dependence for temperatures between 261 and 314 K but increased more than 87% from 5 to 80% *RH* at 295 K and close to 200% from 2 to 80% *RH* at 314 K. The strong exponential increase in the thermal conductivity was linked to the high hygroscopicity of the CNF–polyoxamer foams, which absorbed 26 and 22 wt% moisture at 80% *RH* and 295 K and 314 K respectively. Furthermore, the low moisture resistance or high water vapor permeability contributed to reaching this high moisture equilibrium. The thermal conductivity of CNF–polyoxamer foams was empirically modelled by a modified Künzel’s model which took into consideration the water content by mass as the wet density is a critical parameter for low-density insulation materials that have water vapor resistance factors lower than 1.

The CAM aerogels, which were made from hydrophobic AL-MIL-53 MOF and *Cladophora* cellulose, took up 42% less moisture than the CNF–polyoxamer foams. Their thermal conductivity was around 11% lower at 5% *RH* and 295 K and 36% lower at 80% *RH* and 295 K. Interestingly, the CAM aerogels possessed hierarchical porous structure consisting of macro-, meso- and micropores whereas the CNF–polyoxamer foams mostly had closed macropores. The presence of meso- and micropores is suggested to reduce the gaseous conduction contribution but also to inhibit the penetration of water. Commercial EPS foams exhibited a thermal conductivity of 38 mW m⁻¹ K⁻¹ which is 7% lower than the thermal conductivity of CAM aerogels and 17% lower than the thermal conductivity of CNF–polyoxamer foams. Although the CAM aerogels and the CNF–polyoxamer foams are not super-insulating, they can be good packaging alternatives.

6 Outlook (Paper VI)

The transition towards a fossil-free society with low carbon footprint in the field of thermal insulation could be achieved with the introduction of biobased super-insulating materials. There are many recent studies crowning nanocellulose as a potential raw material for thermal insulation. Most of these studies include isotropic materials, but studies including anisotropic materials are emerging. Taking into consideration the strong intrinsic anisotropy of cellulose, several studies^{38,67,71,89,90,108,111,113,196} have reported the preparation of anisotropic materials which can be used not only in thermal insulation but also in thermal management. Exploiting the intrinsic anisotropy of cellulose offers the possibility to minimise the thermal conductivity perpendicular to the CNM direction even if the pore sizes are not always as small as in case of isotropic foams. Diffuse phonon scattering becomes dominant in nanofibrillar materials with small diameters and large density of interfaces which is responsible for the super-insulating properties. Paper VI also underlines that multiscale materials consisting of cellulose/CNM and other additives contribute to reducing the solid conduction contribution due to phonon mismatch between the different interfaces. The gaseous contribution can be controlled by tuning the pore sizes which of course depends on the foam processing. Foams made by supercritical drying usually display small pores, but supercritical drying is time-consuming and expensive. Processing of multiscale and composite foams and aerogels can also result in small pore sizes with low gas conduction.

As an outlook for future work, the temperature dependence of the thermal conductivity in anisotropic foams can be further investigated in accordance with the temperature-dependent moisture uptake. The development of more environmentally friendly processes to produce super-insulating biobased foams are essential. Crosslinking and hydrophobization could be useful to obtain dry foams by evaporative drying especially in case of anisotropic foams. The effect of different additives on the solid conduction contribution of anisotropic CNM-based foams and aerogels are also of interest. Enhancing the fire-retardancy and mechanical robustness of CNM foams is also imperative and necessary in case of upscaling. Finally, this work included some engineering modelling approaches that can be useful for the research community, but extended modelling of thermal conductivity based on the basic contributions is necessary in predicting the thermal conductivity.

Sammanfattning

Biobaserade superisoleringsmaterial kan bidra till att lindra klimatförändringen genom att minimera användningen av petroleumbaserade material, skapa konstgjorda kolsänkor och minimera den energi som behövs för att bibehålla trevlig inre miljö.

Cellulosananomaterial (CNM) som produceras från rikligt tillgängliga cellulosakällor är mångsidiga, anisotropa råvaror med flexibel ytkemi och hög styrka. I denna avhandling utvärderas värmeledningsförmågan hos isotropa och anisotropa CNM-baserade skum och aerogeler samt analyseras de dominerande värmeledningmekanismerna.

Vi har anpassat en mätcell för bestämning av värmeledningsförmågan hos hygroskopiska skum vid noggrannt kontrollerad relativ luftfuktighet och temperatur. Anisotropa cellulosananofibrerna (CNF) med varierande diametrar uppvisade ett superisolerande beteende vinkelrätt mot nanofibrerriktningen (radiellt), som varierade icke-linjärt med den relativa fuktigheten (RH) och skumdensiteten. Molekylära simuleringar avslöjade att den mycket låga värmeledningsförmågan är relaterad till fononspridning, och ökningen av det interfibrillära separationsavståndet med ökande RH resulterade i en sexfaldig minskning av den termiska gränsskiktsledningsförmågan. Den fuktinducerade minskningen av den termiska gränsskiktsledningsförmågan överstiger värmeledningsförhöjningen på grund av vattenupptaget vid låg och mellanliggande RH och resulterar i en värmeledningsförmåga på endast $14 \text{ mW m}^{-1} \text{ K}^{-1}$ vid 35% RH och 295 K för CNF-skum baserade på de tunnaste nanofibrerna.

Volymvägd modellering av solid- och gasvärmeledningsförmågan hos cellulosananokristall (CNC)-baserade skum med densiteter mellan 25 till 129 kg m^{-3} avslöjade att fononspridning var viktig för att förklara den låga värmeledningsförmåga radiellt; men både ersättning av luft med vatten och Knudsen-effekten relaterade till nanoporositeten i skumväggarna var av mindre betydelse. CNC-skum med mellandensitet (34 kg m^{-3}) uppvisade en radiell värmeledningsförmåga på $24 \text{ mW m}^{-1} \text{ K}^{-1}$ vid 295 K och 20% RH, vilket är lägre än det för luft.

Fuktupptaget av CNM skum med olika grad av kristallinitet och ytmodifikationer minskade betydligt med ökande kristallinitet och temperatur.

Molekylära simuleringar visade att den smala porstorleksfördelningen och den relativt låga adsorptionen av vattenmolekyler i hydreringscellen runt karboxylgruppens syre spelar en viktig roll för fuktupptagningen av amorfa och kristallina CNM-baserade material.

Isotropa CNF- och polyoxamerbaserade skum samt CNF–AL-MIL-53 (ett aluminiumbaserat metal–organic framework) var båda måttligt isolerande ($>40 \text{ mW m}^{-1} \text{ K}^{-1}$) och jämförbara med kommersiell expanderad polystyren. Värmeledningsförmågan hos CNF och polyoxamerskum visade ett mycket starkt RH-beroende som kunde modelleras med en modifierad Künzelmodell. Närvaron av hydrofob AL-MIL-53 minskade fuktupptagningen av CNF–AL-MIL-53 aerogeler med 42% jämfört med CNF-polyoxamerskum.

Värmeledningen (konduktionen) i de fasta materialen och i gasfasen är de viktigaste värmeöverföringsmekanismerna i hygroskopiska nanofibrillära skum och aerogeler, och dessa bidrag kan modereras med gränsytefononspridning, Knudsen-effekten och vattenupptaget. Det är viktigt att värmeledningsmätningar av hygroskopiska CNM-baserade skum och aerogeler bestäms vid kontrollerad RH och att parametrar som temperatur, densitet, nanoporositet, fibrildimensioner och orientering karakteriseras och kontrolleras för systematisk utveckling och uppskalning av biobaserade skum avseende för t.ex. byggnadsisolering och förpackningar.

Περίληψη

Η χρήση υπερ-θερμομονωτικών βιοϋλικών μπορεί να συμβάλλει στο περιορισμό της κλιματικής αλλαγής δημιουργώντας τεχνητές δεξαμενές άνθρακα και μειώνοντας την χρήση υλικών προερχόμενων από το πετρέλαιο και την κατανάλωση ενέργειας με σκοπό τη διατήρηση κατάλληλων συνθηκών σε εσωτερικούς χώρους. Τα νανοϋλικά κυτταρίνης (CNM), τα οποία παράγονται από άφθονα διαθέσιμους φυσικούς πόρους κυτταρίνης, αποτελούν εξαιρετικά ανισότροπες πρώτες ύλες που διαθέτουν ρυθμιζόμενη επιφανειακή χημεία και υψηλή αντοχή. Η παρούσα διατριβή περιλαμβάνει την αξιολόγηση της θερμικής αγωγιμότητας ισότροπων και ανισότροπων αφρών και αεροπηκτωμάτων παρασκευασμένων από νανοϋλικά κυτταρίνης και την ανάλυση των κυρίαρχων μηχανισμών μεταφοράς θερμότητας.

Κατασκευάσαμε μία προσαρμοσμένη περίφρακτη διάταξη για μετρήσεις θερμικής αγωγιμότητας υγροσκοπικών υλικών στην οποία η σχετική υγρασία και η θερμοκρασία ρυθμίζονταν με προσοχή κατά τη διάρκεια των μετρήσεων θερμικής αγωγιμότητας. Οι ανισότροποι αφροί από νανοΐνες κυτταρίνης (CNF) με μεταβαλλόμενες διαμέτρους παρουσίασαν υπερ-θερμομονωτική συμπεριφορά, κάθετα στην κατεύθυνση των νανοΐνων, η οποία ήταν μη γραμμικά εξαρτώμενη από τη σχετική υγρασία (RH) και την πυκνότητα των αφρών. Η εφαρμογή μοριακών προσομοιώσεων έδειξε ότι η πολύ χαμηλή θερμική αγωγιμότητα αυξανομένης της σχετικής υγρασίας οφείλεται στη σκέδαση των φωνονίων λόγω της αύξησης της απόστασης μεταξύ των γειτονικών νανοΐνων η οποία οδήγησε σε εξαπλάσια θερμική αγωγιμότητα διεπαφής. Η διόγκωση που προκαλείται από την υγρασία υπερβαίνει την αύξηση της θερμικής αγωγιμότητας λόγω της πρόσληψης νερού σε χαμηλές και ενδιάμεσες σχετικές υγρασίες με αποτέλεσμα την επίτευξη της ελάχιστης θερμικής αγωγιμότητας, $14 \text{ mW m}^{-1} \text{ K}^{-1}$, σε συνθήκες 35% RH και 295 K για τους αφρούς που παράχθηκαν από τις νανοΐνες με τη μικρότερη διάμετρο.

Επιπροσθέτως μελετήθηκε η θερμική αγωγιμότητα ως συνάρτηση της πυκνότητας αφρών από νανοκρυστάλλους κυτταρίνης (CNC) με πυκνότητες από 25 έως 129 kg m^{-3} . Η χρήση ενός ογκο-σταθμισμένου μοντέλου των συνεισφορών της θερμικής αγωγιμότητας με αγωγή στα στερεά και στα αέρια έδειξε ότι η σκέδαση των φωνονίων είναι απαραίτητη στην επεξήγηση της χαμηλής θερμικής αγωγιμότητας κάθετα στην κατεύθυνση των νανοκρυστάλλων, ενώ η αντικατάσταση του αέρα με νερό καθώς και το

φαινόμενο Knudsen στους νανοπόρους στα τοιχώματα των αφρών παρουσίασαν μικρή επίδραση στη συνολική θερμική αγωγιμότητα. Οι αφροί νανοκρυστάλλων κυτταρίνης ενδιάμεσης πυκνότητας (34 kg m^{-3}) παρουσίασαν θερμική αγωγιμότητα κάθετα στη κατεύθυνση των νανοκρυστάλλων ίση με $24 \text{ mW m}^{-1} \text{ K}^{-1}$, σε συνθήκες σχετικής υγρασίας 20% στους 295 K, η οποία είναι μικρότερη της θερμικής αγωγιμότητας του αέρα.

Η πρόσληψη υγρασίας των αφρών από νανοσωματίδια κυτταρίνης με διαφορετικό βαθμό κρυσταλλικότητας και ποικίλες επιφανειακές χημικές τροποποιήσεις μειώθηκε σημαντικά με την αύξηση της κρυσταλλικότητας των νανοσωματιδίων και της θερμοκρασίας. Η εφαρμογή μοριακών προσομοιώσεων έδειξε ότι η περιορισμένη κατανομή του μεγέθους των πόρων στις άμορφες μεμβράνες κυτταρίνης και η σχετικά χαμηλή προσρόφηση νερού γύρω από οξυγόνο της καρβοξυλομάδας παίζουν καθοριστικό ρόλο στο μηχανισμό πρόσληψης υγρασίας άμορφων και κρυσταλλικών υλικών από νανοσωματίδια κυτταρίνης.

Η μελέτη ισότροπων αφρών νανοϊνών κυτταρίνης και πολοξαμερούς καθώς και αεροπηκτώματων νανοϊνών κυτταρίνης σε συνδυασμό με το AL-MIL-53 (ένα πορώδες μέταλλο-οργανικό υλικό, MOF, με βάση το αλουμίνιο) έδειξε ότι είχαν μέτριες θερμομονωτικές ιδιότητες ($>40 \text{ mW m}^{-1} \text{ K}^{-1}$) αλλά ήταν σε συγκρίσιμα επίπεδα με τις τιμές των εμπορικά διαθέσιμων αφρών διογκωμένου πολυστυρενίου. Η θερμική αγωγιμότητα των αφρών νανοϊνών κυτταρίνης και πολοξαμερούς παρουσίασε ισχυρή εξάρτηση από τη σχετική υγρασία η οποία μοντελοποιήθηκε με ένα τροποποιημένο μοντέλο Künzel. Η παρουσία του υδρόφοβου AL-MIL-53 μείωσε τη πρόσληψη υγρασίας των αεροπηκτώματων από νανοϊνες κυτταρίνης και AL-MIL-53 κατά 42% σε σύγκριση με τους αφρούς νανοϊνών κυτταρίνης και πολοξαμερούς.

Η μεταφορά θερμότητας με αγωγή τόσο στα στερεά όσο και στα αέρια είναι ο βασικός τρόπος μεταφοράς θερμότητας σε υγροσκοπικούς αφρούς και αεροπηκτώματα νανοσωματιδίων και εξαρτάται από τη σκέδαση διεπαφής των φωνονίων, το φαινόμενο Knudsen και τη πρόσληψη υγρασίας. Τέλος είναι απαραίτητη η σωστή διεξαγωγή των μετρήσεων θερμικής αγωγιμότητας σε ρυθμιζόμενο περιβάλλον σχετικής υγρασίας καθώς και ο έλεγχος διαφόρων παραμέτρων όπως η θερμοκρασία, η πυκνότητα, το νανοπορώδες, οι διαστάσεις και η ανισότροπη ευθυγράμμιση των νανοσωματιδίων για την επίτευξη της συστηματικής ανάπτυξης και την αναβάθμιση των βιο-αφρών για εφαρμογή σε θερμομόνωση κτηρίων και συσκευασίες προϊόντων.

Acknowledgements

For me doing a PhD was a dream which would not have been completed without the support of many people during this 5-year period.

I would like first to thank my supervisor *Lennart Bergström* for selecting me in the first place and giving me the opportunity to be a part of his group. I also want to thank him for his continuous support and for the scientific discussions which improved my personal and scientific skills. I highly appreciate his support to apply for international conferences and many other scientific occasions such as the Marcus Wallenberg Prize for young researchers) but also his trust on my presentation skills. Last but not least, I want to thank him for his numerous and long feedback meetings which improved my writing skills and my critical thinking even if they seemed endless.

I want also to thank my co-supervisor *Aji Mathew* for supporting my research and *Niklas Hedin* for his support and for selecting me as Teacher Assistant in his course Porous Materials.

I want to give a big thank you to *Nathalie Lavoine*, my devoted friend, collaborator, and excellent teacher. Her presence at Stockholm University facilitated my research in all aspects, practical and theoretical. Without her true support, patience, guidance and help my evolution as a scientist would have been much slower than it was. Even the times that she was not a part of Stockholm University, Nathalie helped me to solve many of my problems and she was present during my entire PhD journey.

I would like to thank Professor *Junichiro Shiomi* for our excellent collaboration, his useful scientific advice, and his trust on me. Furthermore, I want to thank Professor *Igor Zozoulenko* who has been an excellent collaborator. I want also to thank Professor *Eva Malmström* for her support on me and my research and her initiation for enhancing collaboration. Lastly, I want to thank Professor *Shu-Hong Yu* and Dr. *Chao Xu* for collaborating with me and for trusting my research.

The next person who deserves a great appreciation is *Korneliya Gordeyeva* who guided me in all my first steps at Stockholm University while she

remained a devoted friend who patiently heard all my personal and scientific concerns during the first three years of my PhD education.

I want to thank *Pierre*, my officemate, lab-mate, and great friend for all the countless days we spent chatting in the office, in the lab or digitally. I enjoyed all the altruistic help from your side but also our fruitful collaborations throughout the years during our PhD education. I appreciate that you have been always present for me, patiently hearing my concerns and trying to solve all problems.

Konstantin and *Martin* completed our final four team and I want to thank both of you for your scientific support when I was asking your help. Without you the PhD years would have been only stressful and boring. Your good friendship was very important for me and I missed you a lot during this unexpected pandemic which made us see each other less. I also thank *Fredrik* with whom we met the first day of my PhD. We were both teacher assistants in porous materials course and had always great discussions and memorable experiences and remained a loyal friend through the years.

I want to specifically thank *Daniela* who has been my office mate during my first year, great lifelong friend and a very good scientific advisor. I want to thank *Yulia* for being good friend and supportive and *Alisa* for her scientific help. I also thank *Andreas* who was my first mentor and helped me initiate my PhD research. Furthermore, I thank *Tamara* for all the careful linguistic feedback and for including me in her project. I would like to thank all my co-authors and particularly *Mohit Garg*, *Shengyang Zhou*, *Tahani Kaldéus*, *Mathieu Linares* and *Zhi-Long Yu* for their scientific cooperation.

I want to thank *Linda Fogelström* and *Paul Gatenholm* for their support and help in the WWSC network which helped me gain additional scientific skills and experiences. I want also to thank *Josefin Illergård* for selecting me to participate in the Treesearch movie which created memorable moments from my PhD years.

I would like to thank all the current and former members of our group, *Yingxin*, *Hugo*, *Jens*, *Karin*, *Michiel*, *Bernd*, *Misha*, *Arnaud*, *Zhong-Peng*, *Felicitas*, *Lukasz*, *Maria*, *Aygül*, *Veit*, *Melanie*, *Andi*, *Carina*, *Ehsan*, with whom I had the chance to exchange valuable scientific opinions and great memorable moments.

I would like to additionally thank all professors and scientists that they offered me help and support (*Gunnar, Mats, Ulrich, Mika, Jekabs, Mirva, Cheuk-Wai, Kjell, Zoltan, Arnold, German*) and all the administration members (*Helmi, Ann, Tatiana, Elisabeth, Camilla, Daniel, Lilian, Rolf*) who helped numerous times with upcoming issues. I want to give special thanks to Pelle who patiently assisted many times with workshop questions and issues, and he contributed significantly to manufacture my special measurement cell which made this PhD research go forward.

I want to thank all MMK colleagues that cheered up every moment (*Paulo, Vahid, Xia, Dimitris, Luis, Przemek, Andrea, Natalia, Sadaf, Blanca, Atefeh, Erik, Jon, Mylad, Aditya, Valentina, Tetyana, Sahar*).

I want to give my special thanks to all my friends in Sweden who made all those years wonderful (*Mercy, Henrik, Anne-Liv, Henry, Lisa, Eva, Manos, Alexandros, Pelle, Niloo, Donato, Pouyan, Sadaf, Nanta, Silvia, Efthymios, Gerasimos, Anna, Konstantin, Linnea, Lina, Malin*).

I want to thank my family for their supreme support not only during my PhD studies but during my entire education. I am thankful to my mother, *Anastasia*, and my father, *Fotis*, who both strongly motivated my education giving me useful suggestions for my future career. My mom has always been a role model with strong personality, great ambitions and capabilities that initiated my desire to become an Engineer. My dad has been my mentor who always helped me make the right decisions and believed in my academic qualifications. Their help has been always undebatable, generous, and altruistic. I cannot properly express my immense gratitude to their continuous contribution and their wise advices all the times I needed to make important decisions or when I was confused and disappointed. Furthermore, I thank my younger brother, *Konstantinos*, who despite our big age difference has been always close to me. His great intelligence and his choice of selecting similar scientific paths with me gave us the opportunity to be truthful inspiration for each other while exchanging scientific ideas.

I cannot find the proper words to thank my ultimate buddy, my friend, my love, my husband *Panos* who has been supporting me almost half of my life selflessly. I thank Panos for motivating me when I was let down, for supporting me when I was in front of new challenges and for always believing in my capabilities. I also thank him for being patient when I was angry and tired and for doing all he could to facilitate my PhD years. Our common

education instead of creating conflicts, helped us move forward and he helped me numerous times to find solutions in my scientific problems. His success as a PhD student and his great disputation inspired me to continue fighting. Lastly, I want to thank my 2.5 years old son, *Harry*, who made the last 2-3 years of my PhD life more wonderful even if it was definitely more challenging. Having Harry made me more persistent and organized to become better in all aspects so he can be proud of me.

References

- (1) Dean, B., Dulac, J., Petrichenko, K., and Graham, P. *Towards a Zero-Emission, Efficient, and Resilient Buildings and Construction Sector*; 2016.
- (2) Building, M.; Codes, E. Energy Codes. *ASHRAE J.* **2013**, *55* (August).
- (3) International Energy Agency. *Global Alliance for Buildings and Construction, 2018 Global Status Report*; 2018. <https://doi.org/https://doi.org/10.1038/s41370-017-0014-9>.
- (4) International Energy Agency. *Transition to Sustainable Buildings*; Paris, 2013.
- (5) Churkina, G.; Organschi, A.; Reyer, C. P. O.; Ruff, A.; Vinke, K.; Liu, Z.; Reck, B. K.; Graedel, T. E.; Schellnhuber, H. J. Buildings as a Global Carbon Sink. *Nat. Sustain.* **2020**, *3* (4), 269–276. <https://doi.org/10.1038/s41893-019-0462-4>.
- (6) FAO. *Global Forest Resources Assessment 2020*; 2020. <https://doi.org/10.4060/ca9825en>.
- (7) Jelle, B. P. Traditional, State-of-the-Art and Future Thermal Building Insulation Materials and Solutions - Properties, Requirements and Possibilities. *Energy Build.* **2011**, *43* (10), 2549–2563. <https://doi.org/10.1016/j.enbuild.2011.05.015>.
- (8) Budtova, T. Bio-Based Aerogels: A New Generation of Thermal Superinsulating Materials. In *Cellulose Science and Technology: Chemistry, Analysis, and Applications, First Edition*; 2019; pp 371–392.
- (9) Cuce, E.; Cuce, P. M.; Wood, C. J.; Riffat, S. B. Toward Aerogel Based Thermal Superinsulation in Buildings: A Comprehensive Review. *Renew. Sustain. Energy Rev.* **2014**, *34*, 273–299. <https://doi.org/10.1016/j.rser.2014.03.017>.
- (10) Kumar, A.; Suman, B. M. Experimental Evaluation of Insulation Materials for Walls and Roofs and Their Impact on Indoor Thermal Comfort under Composite Climate. *Build. Environ.* **2013**, *59*, 635–643. <https://doi.org/10.1016/j.buildenv.2012.09.023>.
- (11) Glicksman, L. Heat Transfer in Foams. *Low density Cell. Plast.* **1994**, 104–152.
- (12) Collishaw, P. G.; Evans, J. R. G. An Assessment of Expressions for the Apparent Thermal-Conductivity of Cellular Materials. *J. Mater. Sci.* **1994**, *29* (9), 2261–2273. <https://doi.org/10.1007/BF00363413>.

- (13) Haghi, A. K. *Heat & Mass Transfer in Textiles*; WSEAS Press: Montreal, 2011.
- (14) Guo, J. F.; Tang, G. H. A Theoretical Model for Gas-Contributed Thermal Conductivity in Nanoporous Aerogels. *Int. J. Heat Mass Transf.* **2019**, *137*, 64–73. <https://doi.org/10.1016/j.ijheatmasstransfer.2019.03.106>.
- (15) Lu, X.; Arduini-Schuster, M. C.; Kuhn, J.; Nilsson, O.; Fricke, J.; Pekala, R. W. Thermal Conductivity of Monolithic Organic Aerogels. *Science* (80-.). **1992**, *255* (5047), 971–972. <https://doi.org/10.1126/science.255.5047.971>.
- (16) Apostolopoulou-Kalkavoura, V.; Munier, P.; Bergström, L. Thermally Insulating Nanocellulose-Based Materials. *Adv. Mater.* **2020**, *2001839*, 1–17. <https://doi.org/10.1002/adma.202001839>.
- (17) Kreith, F.; Black, W. Z. *Basic Heat Transfer*; Harper & Row, Ed.; 1980; Vol. 45. <https://doi.org/10.1201/9780203755570-15>.
- (18) Uetani, K.; Hatori, K. Thermal Conductivity Analysis and Applications of Nanocellulose Materials. *Sci. Technol. Adv. Mater.* **2017**, *18* (1), 1–16. <https://doi.org/10.1080/14686996.2017.1390692>.
- (19) Dri, F. L.; Shang, S.; Jr, L. G. H.; Saxe, P.; Liu, Z.; Moon, R. J.; Zavattieri, P. D. Anisotropy and Temperature Dependence of Structural , Thermodynamic, and Elastic Properties of Crystalline Cellulose Iβ : A First-Principles Investigation. *Model. Simul. Mater. Sci. Eng.* **2014**, *22* (085012), 1–28. <https://doi.org/10.1088/0965-0393/22/8/085012>.
- (20) Cahill, D. G.; Goodson, K. E.; Majumdar, A. Thermometry and Thermal Transport in Micro/Nanoscale Solid-State Devices and Structures. *J. Heat Transfer* **2002**, *124* (2), 223. <https://doi.org/10.1115/1.1454111>.
- (21) Losego, M. D.; Grady, M. E.; Sottos, N. R.; Cahill, D. G.; Braun, P. V. Effects of Chemical Bonding on Heat Transport across Interfaces. *Nat. Mater.* **2012**, *11* (6), 502–506. <https://doi.org/10.1038/nmat3303>.
- (22) Chernatynskiy, A.; Clarke, D. R.; Phillpot, S. R. *Thermal Transport in Nanostructured Materials*; 2012. <https://doi.org/10.1201/b11930-24>.
- (23) Kim, G.-H.; Lee, D.; Shanker, A.; Shao, L.; Kwon, M. S.; Gidley, D.; Kim, J.; Pipe, K. P. High Thermal Conductivity in Amorphous Polymer Blends by Engineered Interchain Interactions. *Nat. Mater.* **2015**, *14* (3), 295–300. <https://doi.org/10.1038/nmat4141>.
- (24) Li, D.; Mcgaughey, A. J. H. Phonon Dynamics at Surfaces and Interfaces and Its Implications in Energy Transport in Nanostructured Materials — An Opinion Paper. *Nanoscale Microscale Thermophys.*

- (25) Henry, A.; Chen, G.; Plimpton, S.; Thompson, A. 1D-to-3D Transition of Phonon Heat Conduction in Polyethylene Using Molecular Dynamics Simulations. *Phys. Rev. B* **2010**, 82, 144308. <https://doi.org/10.1103/PhysRevB.82.144308>.
- (26) Zhang, L.; Ruesch, M.; Zhang, X.; Bai, Z.; Liu, L. Tuning Thermal Conductivity of Crystalline Polymer Nanofibers by Interchain Hydrogen Bonding. *RSC Adv.* **2015**, 5 (107), 87981–87986. <https://doi.org/10.1039/C5RA18519J>.
- (27) Machrafi, H.; Lebon, G. Size and Porosity Effects on Thermal Conductivity of Nanoporous Material with an Extension to Nanoporous Particles Embedded in a Host Matrix. *Phys. Lett. Sect. A Gen. At. Solid State Phys.* **2015**, 379 (12–13), 968–973. <https://doi.org/10.1016/j.physleta.2015.01.027>.
- (28) Bi, C.; Tang, G. H.; Hu, Z. J.; Yang, H. L.; Li, J. N. Coupling Model for Heat Transfer between Solid and Gas Phases in Aerogel and Experimental Investigation. *Int. J. Heat Mass Transf.* **2014**, 79, 126–136. <https://doi.org/10.1016/j.ijheatmasstransfer.2014.07.098>.
- (29) Wei, G.; Liu, Y.; Zhang, X.; Yu, F.; Du, X. Thermal Conductivities Study on Silica Aerogel and Its Composite Insulation Materials. *Int. J. Heat Mass Transf.* **2011**, 54 (11–12), 2355–2366. <https://doi.org/10.1016/j.ijheatmasstransfer.2011.02.026>.
- (30) Obori, M.; Suh, D.; Yamasaki, S.; Kodama, T.; Saito, T.; Isogai, A.; Shiomi, J. Parametric Model to Analyze the Components of the Thermal Conductivity of a Cellulose-Nanofibril Aerogel. *Phys. Rev. Appl.* **2019**, 11 (2), 1. <https://doi.org/10.1103/PhysRevApplied.11.024044>.
- (31) Lu, X.; Caps, R.; Fricke, J.; Alviso, C. T.; Pekala, R. W. Correlation between Structure and Thermal Conductivity of Organic Aerogels. *J. Non. Cryst. Solids* **1995**, 188 (3), 226–234. [https://doi.org/10.1016/0022-3093\(95\)00191-3](https://doi.org/10.1016/0022-3093(95)00191-3).
- (32) Zhu, C. Y.; Li, Z. Y. Modeling of the Apparent Solid Thermal Conductivity of Aerogel. *Int. J. Heat Mass Transf.* **2018**, 120, 724–730. <https://doi.org/10.1016/j.ijheatmasstransfer.2017.12.076>.
- (33) Chen, G. Phonon Heat Conduction in Nanostructures. *Int. J. Therm. Sci.* **2000**, 39 (4), 471–480. [https://doi.org/10.1016/S1290-0729\(00\)00202-7](https://doi.org/10.1016/S1290-0729(00)00202-7).
- (34) Regner, K. T.; Sellan, D. P.; Su, Z.; Amon, C. H.; McGaughey, A. J. H.; Malen, J. Broadband Phonon Mean Free Path Contributions to

- Thermal Conductivity Measured Using Frequency Domain Thermoreflectance. *Nat. Commun.* **2013**, *4*, 1640. <https://doi.org/10.1038/ncomms2630>.
- (35) Cahill, D. G.; Braun, P. V.; Chen, G.; Clarke, D. R.; Fan, S.; Goodson, K. E.; Keblinski, P.; King, W. P.; Mahan, G. D.; Majumdar, A.; Maris, H. J.; Phillpot, S. R.; Pop, E.; Shi, L. Nanoscale Thermal Transport. II. *Appl. Phys. Rev.* **2014**, *1* (1), 1–45. <https://doi.org/10.1063/1.4832615>.
 - (36) Xie, Y.; Xu, S.; Xu, Z.; Wu, H.; Deng, C.; Wang, X. Interface-Mediated Extremely Low Thermal Conductivity of Graphene Aerogel. *Carbon N. Y.* **2016**, *98*, 381–390. <https://doi.org/10.1016/j.carbon.2015.11.033>.
 - (37) Coquard, R.; Baillis, D. Thermal Conductivity of Kelvin Cell Cellulosic Aerogels: Analytical and Monte Carlo Approaches. *J. Mater. Sci.* **2017**, *52* (19), 11135–11145. <https://doi.org/10.1007/s10853-017-0982-0>.
 - (38) Wicklein, B.; Kocjan, A.; Salazar-Alvarez, G.; Carosio, F.; Camino, G.; Antonietti, M.; Bergström, L. Thermally Insulating and Fire-Retardant Lightweight Anisotropic Foams Based on Nanocellulose and Graphene Oxide. *Nat. Nanotechnol.* **2015**, *10* (3), 277–283. <https://doi.org/10.1038/nnano.2014.248>.
 - (39) Kapitza, P. L. The Study of Heat Transfer in Helium II. *J. Phys.* **1941**, *4*, 181–210. <https://doi.org/10.1016/b978-0-08-015816-7.50014-6>.
 - (40) Yu, Z.-L.; Yang, N.; Apostolopoulou-Kalkavoura, V.; Qin, B.; Ma, Z.-Y.; Xing, W.-Y.; Qiao, C.; Bergström, L.; Antonietta, M.; Yu, S.-H. Fire-Retardant and Thermally Insulating Phenolic-Silica Aerogels. *Angew. Chemie Int. Ed.* **2018**, *57* (17), 4538–4542. <https://doi.org/10.1002/anie.201711717>.
 - (41) Kaganer, M. Thermal Insulation in Cryogenic Engineering. *Isr. Progr. Sci. Transl.* **1969**.
 - (42) Malek, K.; Coppens, M. O. Knudsen Self- and Fickian Diffusion in Rough Nanoporous Media. *J. Chem. Phys.* **2003**, *119* (5), 2801–2811. <https://doi.org/10.1063/1.1584652>.
 - (43) Zeng, S. Q.; Hunt, A.; Greif, R. Transport Properties of Gas in Silica Aerogel. *J. Non. Cryst. Solids* **1995**, *186*, 264–270. [https://doi.org/10.1016/0022-3093\(95\)00052-6](https://doi.org/10.1016/0022-3093(95)00052-6).
 - (44) Baetens, R.; Jelle, B. P.; Gustavsen, A. Review: Aerogel Insulation for Building Applications: A State-of-the-Art Review. *Energy Build.* **2011**, *43* (4), 761–769. <https://doi.org/10.1016/j.enbuild.2010.12.012>.
 - (45) Duong, H. M.; Nguyen, S. T. Chapter 15 Nanocellulose Aerogels as Thermal Insulation Materials. In *Nano and Biotech Based Materials*

for *Energy Building Efficiency*; SpringerNature, 2016; pp 97–124.
<https://doi.org/10.1007/978-3-319-27505-5>.

- (46) Reichenauer, G.; Heinemann, U.; Ebert, H. P. Relationship between Pore Size and the Gas Pressure Dependence of the Gaseous Thermal Conductivity. *Colloids Surfaces A Physicochem. Eng. Asp.* **2007**, *300* (1-2 SPEC. ISS.), 204–210.
<https://doi.org/10.1016/j.colsurfa.2007.01.020>.
- (47) Kaganer, M. Thermal Insulation in Cryogenic Engineering. *Isr. Progr. Sci. Transl.* **1969**.
- (48) Swimm, K.; Reichenauer, G.; Vidi, S.; Ebert, H. P. Gas Pressure Dependence of the Heat Transport in Porous Solids with Pores Smaller than 10µm. *Int. J. Thermophys.* **2009**, *30* (4), 1329–1342.
<https://doi.org/10.1007/s10765-009-0617-z>.
- (49) Raed, K. *Investigation of a Knudsen and Gas-Atmosphere Effects on Effective Thermal Conductivity of Porous Media*; 2013.
- (50) Comsol. *The Heat Transfer Module User's Guide - 4.4*; 2012.
- (51) Haghi, A. K. *Heat and Mass Transfer in Textiles*; Haghi, A. K., Ed.; WSEAS Press, 2011.
- (52) Jelle, B. P. Traditional, State-of-the-Art and Future Thermal Building Insulation Materials and Solutions - Properties, Requirements and Possibilities. *Energy Build.* **2011**, *43* (10), 2549–2563.
<https://doi.org/10.1016/j.enbuild.2011.05.015>.
- (53) Jarfelt, U.; Ramnäs, O. Thermal Conductivity of Polyurethane Foam - Best Performance. In *10th International Symposium on District Heating and Cooling*; Göteborg, 2006; p 12.
- (54) Federation of European Rigid Polyurethane Foam Association. *Thermal Insulation Materials Made of Rigid Polyurethane Foam (PUR/PIR)*; 2006.
- (55) Winterling, H.; Sonntag, N. *Rigid Polystyrene Foam (EPS, XPS)*; 2011; Vol. 101.
- (56) Jerman, M.; Černý, R. Effect of Moisture Content on Heat and Moisture Transport and Storage Properties of Thermal Insulation Materials. *Energy Build.* **2012**, *53*, 39–46.
<https://doi.org/10.1016/j.enbuild.2012.07.002>.
- (57) Berge, A.; Johansson, P. *Literature Review of High Performance Thermal Insulation*; Gothenburg, Chalmers University of Technology, 2012.
- (58) Baetens, R.; Jelle, B. P.; Gustavsen, A. Aerogel Insulation for Building Applications: A State-of-the-Art Review. *Energy Build.* **2011**, *43* (4),

- 761–769. <https://doi.org/10.1016/j.enbuild.2010.12.012>.
- (59) Lavoine, N.; Bergström, L. Nanocellulose-Based Foams and Aerogels: Processing, Properties, and Applications. *J. Mater. Chem. A* **2017**, *5*, 16105–16117. <https://doi.org/10.1039/c7ta02807e>.
 - (60) Illera, D.; Mesa, J.; Gomez, H.; Maury, H. Cellulose Aerogels for Thermal Insulation in Buildings: Trends and Challenges. *Coatings* **2018**, *345*, 1–13. <https://doi.org/10.3390/coatings8100345>.
 - (61) Lavoine, N.; Bergström, L. Nanocellulose-Based Foams and Aerogels: Processing, Properties, and Applications. *J. Mater. Chem. A* **2017**, *5* (2009), 16105–16117. <https://doi.org/10.1039/c7ta02807e>.
 - (62) Sakai, K.; Kobayashi, Y.; Saito, T.; Isogai, A. Partitioned Airls at Microscale and Nanoscale: Thermal Diffusivity in Ultrahigh Porosity Solids of Nanocellulose. *Sci. Rep.* **2016**, *6* (February), 20434. <https://doi.org/10.1038/srep20434>.
 - (63) Kobayashi, Y.; Saito, T.; Isogai, A. Aerogels with 3D Ordered Nanofiber Skeletons of Liquid-Crystalline Nanocellulose Derivatives as Tough and Transparent Insulators. *Angew. Chem. Int. Ed. Engl.* **2014**, *53* (39), 10394–10397. <https://doi.org/10.1002/anie.201405123>.
 - (64) Jaxel, J.; Markevicius, G.; Rigacci, A.; Budtova, T. Thermal Superinsulating Silica Aerogels Reinforced with Short Man-Made Cellulose Fibers. *Compos. Part A* **2017**, *103*, 113–121. <https://doi.org/10.1016/j.compositesa.2017.09.018>.
 - (65) Seantier, B.; Bendahou, D.; Bendahou, A.; Grohens, Y.; Kaddami, H. Multi-Scale Cellulose Based New Bio-Aerogel Composites with Thermal Super-Insulating and Tunable Mechanical Properties. *Carbohydr. Polym.* **2016**, *138*, 335–348. <https://doi.org/10.1016/j.carbpol.2015.11.032>.
 - (66) Jimenez-Saelices, C.; Seantier, B.; Cathala, B.; Grohens, Y. Spray Freeze-Dried Nanofibrillated Cellulose Aerogels with Thermal Superinsulating Properties. *Carbohydr. Polym.* **2017**, *157*, 105–113. <https://doi.org/10.1016/j.carbpol.2016.09.068>.
 - (67) Jiménez-saelices, C. Effect of Freeze-Drying Parameters on the Microstructure and Thermal Insulating Properties of Nanofibrillated Cellulose Aerogels. *J. Sol-Gel Sci. Technol.* **2017**, 475–485. <https://doi.org/10.1007/s10971-017-4451-7>.
 - (68) Bendahou, D.; Bendahou, A.; Seantier, B.; Grohens, Y.; Kaddami, H. Nano-Fibrillated Cellulose-Zeolites Based New Hybrid Composites Aerogels with Super Thermal Insulating Properties. *Ind. Crops Prod.* **2015**, *65*, 374–382. <https://doi.org/10.1016/j.indcrop.2014.11.012>.
 - (69) Zhou, S.; Apostolopoulou-Kalkavoura, V.; Tavares da Costa, M. V.;

- Bergström, L.; Strømme, M.; Xu, C. Elastic Aerogels of Cellulose Nanofibers@Metal–Organic Frameworks for Thermal Insulation and Fire Retardancy. *Nano-Micro Lett.* **2020**, *12* (1), 1–13. <https://doi.org/10.1007/s40820-019-0343-4>.
- (70) Munier, P.; Gordeyeva, K.; Bergström, L.; Fall, A. B. Directional Freezing of Nanocellulose Dispersions Aligns the Rod-Like Particles and Produces Low-Density and Robust Particle Networks. *Biomacromolecules* **2016**, *17* (5), 1875–1881. <https://doi.org/10.1021/acs.biomac.6b00304>.
- (71) Apostolopoulou-Kalkavoura, V.; Hu, S.; Lavoine, N.; Garg, M.; Linares, M.; Munier, P.; Zozoulenko, I.; Shiomi, J.; Bergström, L. Humidity-Dependent Thermal Boundary Conductance Controls Heat Transport of Super-Insulating Nanofibrillar Foams Humidity-Dependent Thermal Boundary Conductance Controls Heat Transport of Super-Insulating Nanofibrillar Foams. *Matter* **2021**, *4*, 1–14. <https://doi.org/10.1016/j.matt.2020.11.007>.
- (72) Faruk, O.; Bledzki, A. K.; Matuana, L. M. Microcellular Foamed Wood-Plastic Composites by Different Processes: A Review. *Macromol. Mater. Eng.* **2007**, *292* (2), 113–127. <https://doi.org/10.1002/mame.200600406>.
- (73) Bikerman, J. J. The Unit of Foaminess. *Trans. Faraday Soc.* **1938**, *34* (634), 634–638.
- (74) Miles, G. D.; Ross, J. Foam Stability of Solutions of Soaps of Pure Fatty Acids. *J. Phys. Chem.* **1944**, *48* (5), 280–290. <https://doi.org/10.1021/j150437a006>.
- (75) Gordeyeva, K. S.; Fall, A. B.; Hall, S.; Wicklein, B.; Bergström, L. Stabilizing Nanocellulose-Nonionic Surfactant Composite Foams by Delayed Ca-Induced Gelation. *J. Colloid Interface Sci.* **2016**, *472*, 44–51. <https://doi.org/10.1016/j.jcis.2016.03.031>.
- (76) Cervin, N. T.; Johansson, E.; Larsson, P. A.; Wågberg, L. Strong, Water-Durable, and Wet-Resilient Cellulose Nanofibril-Stabilized Foams from Oven Drying. *ACS Appl. Mater. Interfaces* **2016**, *8* (18), 11682–11689. <https://doi.org/10.1021/acsami.6b00924>.
- (77) Jiménez-Saelices, C.; Seantier, B.; Grohens, Y.; Capron, I. Thermal Superinsulating Materials Made from Nanofibrillated Cellulose-Stabilized Pickering Emulsions. *ACS Appl. Mater. Interfaces* **2018**, *10* (18), 16193–16202. <https://doi.org/10.1021/acsami.8b02418>.
- (78) Markevicius, G.; Ladj, R.; Niemeyer, P.; Budtova, T.; Rigacci, A. Ambient-Dried Thermal Superinsulating Monolithic Silica-Based Aerogels with Short Cellulosic Fibers. *J. Mater. Sci.* **2017**, *52* (4), 2210–2221. <https://doi.org/10.1007/s10853-016-0514-3>.

- (79) Li, T.; Du, A.; Zhang, T.; Ding, W.; Liu, M.; Shen, J.; Zhang, Z.; Zhou, B. Efficient Preparation of Crack-Free, Low-Density and Transparent Polymethylsilsesquioxane Aerogels: Via Ambient Pressure Drying and Surface Modification. *RSC Adv.* **2018**, 8 (32), 17967–17975. <https://doi.org/10.1039/c8ra03061h>.
- (80) Hayase, G.; Kanamori, K.; Abe, K.; Yano, H.; Maeno, A.; Kaji, H.; Nakanishi, K. Polymethylsilsesquioxane-Cellulose Nanofiber Biocomposite Aerogels with High Thermal Insulation, Bendability, and Superhydrophobicity. *ACS Appl. Mater. Interfaces* **2014**, 6 (12), 9466–9471. <https://doi.org/10.1021/am501822y>.
- (81) Wong, J. C. H.; Kaymak, H.; Tingaut, P.; Brunner, S.; Koebel, M. M. Mechanical and Thermal Properties of Nanofibrillated Cellulose Reinforced Silica Aerogel Composites. *Microporous Mesoporous Mater.* **2015**, 217, 150–158. <https://doi.org/10.1016/j.micromeso.2015.06.025>.
- (82) Demilecamps, A.; Alves, M.; Rigacci, A.; Reichenauer, G.; Budtova, T. Nanostructured Interpenetrated Organic-Inorganic Aerogels with Thermal Superinsulating Properties. *J. Non. Cryst. Solids* **2016**, 452, 259–265. <https://doi.org/10.1016/j.jnoncrysol.2016.09.003>.
- (83) Demilecamps, A.; Beauger, C.; Hildenbrand, C.; Rigacci, A.; Budtova, T. Cellulose-Silica Aerogels. *Carbohydr. Polym.* **2015**, 122, 293–300. <https://doi.org/10.1016/j.carbpol.2015.01.022>.
- (84) Cai, J.; Liu, S.; Feng, J.; Kimura, S.; Wada, M.; Kuga, S.; Zhang, L. Cellulose – Silica Nanocomposite Aerogels by In Situ Formation of Silica in Cellulose Gel. *Angew. Chem. Int. Ed.* **2012**, 1, 2076–2079. <https://doi.org/10.1002/anie.201105730>.
- (85) Fu, J.; Wang, S.; He, C.; Lu, Z.; Huang, J.; Chen, Z. Facilitated Fabrication of High Strength Silica Aerogels Using Cellulose Nanofibrils as Scaffold. *Carbohydr. Polym.* **2016**, 147, 89–96. <https://doi.org/10.1016/j.carbpol.2016.03.048>.
- (86) Zhao, S.; Zhang, Z.; Sèbe, G.; Wu, R.; Virtudazo, R. V. R.; Tingaut, P.; Koebel, M. M. Multiscale Assembly of Superinsulating Silica Aerogels Within Silylated Nanocellulosic Scaffolds: Improved Mechanical Properties Promoted by Nanoscale Chemical Compatibilization. *Adv. Funct. Mater.* **2015**, 25, 2326–2334. <https://doi.org/10.1002/adfm.201404368>.
- (87) Jiménez-Saelices, C.; Seantier, B.; Cathala, B.; Grohens, Y. Spray Freeze-Dried Nanofibrillated Cellulose Aerogels with Thermal Superinsulating Properties. *Carbohydr. Polym.* **2017**, 157, 105–113. <https://doi.org/10.1016/j.carbpol.2016.09.068>.
- (88) Chen, W.; Li, Q.; Wang, Y.; Yi, X.; Zeng, J.; Yu, H. Comparative

Study of Aerogels Obtained from Differently Prepared Nanocellulose Fibers. *ChemSusChem* **2014**, 230026, 154–161. <https://doi.org/10.1002/cssc.201300950>.

- (89) Kriechbaum, K.; Munier, P.; Apostolopoulou-Kalkavoura, V.; Lavoine, N. Analysis of the Porous Architecture and Properties of Anisotropic Nanocellulose Foams: A Novel Approach to Assess the Quality of Cellulose Nanofibrils (CNFs). *ACS Sustain. Chem. Eng.* **2018**, 6 (9), 11959–11967. <https://doi.org/10.1021/acssuschemeng.8b02278>.
- (90) Li, T.; Song, J.; Zhao, X.; Yang, Z.; Pastel, G.; Xu, S.; Jia, C.; Dai, J.; Chen, C.; Gong, A.; Jiang, F.; Yao, Y.; Fan, T.; Yang, B.; Wågberg, L.; Yang, R.; Hu, L. Anisotropic, Lightweight, Strong, and Super Thermally Insulating Nanowood with Naturally Aligned Nanocellulose. *Sci. Adv.* **2018**, 4 (3), 1–10. <https://doi.org/10.1126/sciadv.aar3724>.
- (91) Yüksel, N. Methods and Techniques for Measuring the Thermal Conductivity of Insulation Materials. *Intech open Sci.* **2016**, 115–123.
- (92) Al-Ajlan, S. A. Measurements of Thermal Properties of Insulation Materials by Using Transient Plane Source Technique. *Appl. Therm. Eng.* **2006**, 26 (17–18), 2184–2191. <https://doi.org/10.1016/j.applthermaleng.2006.04.006>.
- (93) Zhao, D.; Qian, X.; Gu, X.; Jajja, S. A.; Yang, R. Measurement Techniques for Thermal Conductivity and Interfacial Thermal Conductance of Bulk and Thin Film Materials. *J. Electron. Packag. Trans. ASME* **2016**, 138 (4), 1–64. <https://doi.org/10.1115/1.4034605>.
- (94) Shi, J.; Lu, L.; Guo, W.; Sun, Y.; Cao, Y. An Environment-Friendly Thermal Insulation Material from Cellulose and Plasma Modification. *J. Appl. Polym. Sci.* **2013**, 130 (5), 3652–3658. <https://doi.org/10.1002/app.39615>.
- (95) Blomfeldt, T. O.; Nilsson, F.; Holgate, T.; Xu, J.; Johansson, E.; Hedenqvist, M. S. Thermal Conductivity and Combustion Properties of Wheat Gluten Foams. *ACS Appl. Mater. Interfaces.* **2012**, 4 (1944–8252 (Electronic)), 1629–1635. <https://doi.org/10.1021/am2017877>.
- (96) Silva, M. C.; Takahashi, J. A.; Chaussy, D.; Belgacem, M. N.; Silva, G. G. Composites of Rigid Polyurethane Foam and Cellulose Fiber Residue. *J. Appl. Polym. Sci.* **2010**, 117, 3665–3672.
- (97) Künzle, H. M. *Simultaneous Heat and Moisture Transport in Building Components One- and Two-Dimensional Calculation Using Simple Parameters*; Fraunhofer Institute of Building Physics: Stuttgart, 1995; Vol. 1995. [https://doi.org/ISBN v.3-8167-4103-7](https://doi.org/ISBN%203-8167-4103-7).

- (98) Shi, J.; Lu, L.; Guo, W.; Zhang, J.; Cao, Y. Heat Insulation Performance, Mechanics and Hydrophobic Modification of Cellulose-SiO₂ Composite Aerogels. *Carbohydr. Polym.* **2013**, *98* (1), 282–289. <https://doi.org/10.1016/j.carbpol.2013.05.082>.
- (99) Abdou, A.; Budaiwi, I. The Variation of Thermal Conductivity of Fibrous Insulation Materials under Different Levels of Moisture Content. *Constr. Build. Mater.* **2013**, *43*, 533–544. <https://doi.org/10.1016/j.conbuildmat.2013.02.058>.
- (100) Budaiwi, I.; Abdou, A. The Impact of Thermal Conductivity Change of Moist Fibrous Insulation on Energy Performance of Buildings under Hot-Humid Conditions. *Energy Build.* **2013**, *60*, 388–399. <https://doi.org/10.1016/j.enbuild.2013.01.035>.
- (101) Mi, Q.; Yu, J.; He, J.; Zhang, J. Flexible and Transparent Cellulose Aerogels with Uniform Nanoporous Structure by a Controlled Regeneration Process. *ACS Sustain. Chem. Eng.* **2016**, *4*, 656–660. <https://doi.org/10.1021/acssuschemeng.5b01079>.
- (102) Fischer, F.; Rigacci, A.; Pirard, R.; Berthon-Fabry, S.; Achard, P. Cellulose-Based Aerogels. *Polymer (Guildf)*. **2006**, *47* (22), 7636–7645. <https://doi.org/10.1016/j.polymer.2006.09.004>.
- (103) Ohmura, T.; Tsuboi, M.; Tomimura, T. Estimation of the Mean Thermal Conductivity of Anisotropic Materials. *Int. J.* **2002**, *23* (3), 843–853. <https://doi.org/10.1023/A:1015423708823>.
- (104) Rudaz, C.; Courson, R.; Bonnet, L.; Calas-Etienne, S.; Sallée, H.; Budtova, T. Aeropectin: Fully Biomass-Based Mechanically Strong and Thermal Superinsulating Aerogel. *Biomacromolecules* **2014**, *15* (6), 2188–2195. <https://doi.org/10.1021/bm500345u>.
- (105) Jansson, R. Measurement of Thermal Properties at Elevated Temperatures-Brandforsk Project 328-031. *SP Rep.* **2004**.
- (106) Muthuraj, R.; Sachan, A.; Castro, M.; Feller, J.; Seantier, B.; Grohens, Y. Vapor and Pressure Sensors Based on Cellulose Nanofibers and Carbon Nanotubes Aerogel with Thermoelectric Properties. **2018**, *6* (3), 277–287. <https://doi.org/10.7569/JRM.2017.634182>.
- (107) Gustafsson, S. E.; Karawacki, E.; Khan, M. N. Transient Hot-Strip Method for Simultaneously Measuring Thermal Conductivity and Thermal Diffusivity of Solids and Fluids. *J. Phys. D. Appl. Phys.* **1979**, *12* (9), 1411–1421. <https://doi.org/10.1088/0022-3727/12/9/003>.
- (108) Gupta, P.; Singh, B.; Agrawal, A. K.; Maji, P. K. Low Density and High Strength Nanofibrillated Cellulose Aerogel for Thermal Insulation Application. *Mater. Des.* **2018**, *158*, 224–236. <https://doi.org/10.1016/j.matdes.2018.08.031>.

- (109) Lagüela, S.; Bison, P.; Peron, F.; Romagnoni, P. Thermal Conductivity Measurements on Wood Materials with Transient Plane Source Technique. *Thermochim. Acta* **2015**, *600*, 45–51. <https://doi.org/10.1016/j.tca.2014.11.021>.
- (110) Javadi, A.; Zheng, Q.; Payen, F.; Javadi, A.; Altin, Y.; Cai, Z.; Sabo, R.; Gong, S. Polyvinyl Alcohol-Cellulose Nanofibrils-Graphene Oxide Hybrid Organic Aerogels. *ACS Appl. Mater. Interfaces* **2013**, *5* (13), 5969–5975. <https://doi.org/10.1021/am400171y>.
- (111) Chen, B.; Zheng, Q.; Zhu, J.; Li, J.; Cai, Z.; Chen, L.; Gong, S. Mechanically Strong Fully Biobased Anisotropic Cellulose Aerogels. *RSC Adv.* **2016**, *6*, 96518–96526. <https://doi.org/10.1039/c6ra19280g>.
- (112) Gbewonyo, S.; Carpenter, A. W.; Gause, C. B.; Reddy, N.; Zhang, L. Low Thermal Conductivity Carbon Fibrous Composite Nanomaterial Enabled by Multi-Scale Porous Structure. *Mater. Des.* **2017**, *134*, 218–225. <https://doi.org/10.1016/j.matdes.2017.08.050>.
- (113) Munier, P.; Apostolopoulou-Kalkavoura, V.; Persson, M.; Bergström, L. Strong Silica-Nanocellulose Anisotropic Composite Foams Combine Low Thermal Conductivity and Low Moisture Uptake. *Cellulose* **2019**, 1–12. <https://doi.org/10.1007/s10570-019-02912-0>.
- (114) Apostolopoulou-Kalkavoura, V.; Gordeyeva, K.; Lavoine, N.; Bergström, L. Thermal Conductivity of Hygroscopic Foams Based on Cellulose Nanofibrils and a Nonionic Polyoxamer. *Cellulose* **2018**, *25* (2), 1117–1126. <https://doi.org/10.1007/s10570-017-1633-y>.
- (115) Guo, L.; Chen, Z.; Lyu, S.; Fu, F.; Wang, S. Highly Flexible Cross-Linked Cellulose Nanofibril Sponge-like Aerogels with Improved Mechanical Property and Enhanced Flame Retardancy. *Carbohydr. Polym.* **2018**, *179* (July 2017), 333–340. <https://doi.org/10.1016/j.carbpol.2017.09.084>.
- (116) Bai, J.; Li, Y.; Ren, L.; Mao, M.; Zeng, M.; Zhao, X. Thermal Insulation Monolith of Aluminum Tobermorite Nanosheets Prepared from Fly Ash. *ACS Sustain. Chem. Eng.* **2015**, *3* (11), 2866–2873. <https://doi.org/10.1021/acssuschemeng.5b00808>.
- (117) Karadagli, I.; Schulz, B.; Schestakow, M.; Milow, B.; Gries, T.; Ratke, L. Production of Porous Cellulose Aerogel Fibers by an Extrusion Process. *J. Supercrit. Fluids* **2015**, *106*, 105–114. <https://doi.org/10.1016/j.supflu.2015.06.011>.
- (118) Gustafsson, S. E. Transient Plane Source Techniques for Thermal Conductivity and Thermal Diffusivity Measurements of Solid Materials. *Rev. Sci. Instrum.* **1991**, *62* (3), 797–804. <https://doi.org/10.1063/1.1142087>.

- (119) Chen, J.; Huang, X.; Zhu, Y.; Jiang, P. Cellulose Nanofiber Supported 3D Interconnected BN Nanosheets for Epoxy Nanocomposites with Ultrahigh Thermal Management Capability. *Adv. Funct. Mater.* **2017**, 27 (5), 1–9. <https://doi.org/10.1002/adfm.201604754>.
- (120) Song, N.; Jiao, D.; Ding, P.; Cui, S.; Tang, S.; Shi, L. Anisotropic Thermally Conductive Flexible Films Based on Nanofibrillated Cellulose and Aligned Graphene Nanosheets. *J. Mater. Chem. C* **2016**, 4 (2), 305–314. <https://doi.org/10.1039/C5TC02194D>.
- (121) Qiu, L.; Wang, X.; Su, G.; Tang, D.; Zheng, X.; Zhu, J.; Wang, Z.; Norris, P. M.; Bradford, P. D.; Zhu, Y. Remarkably Enhanced Thermal Transport Based on a Flexible Horizontally-Aligned Carbon Nanotube Array Film. *Sci. Rep.* **2016**, 6 (October 2015), 1–14. <https://doi.org/10.1038/srep21014>.
- (122) Gesele, G.; Linsmeier, J.; Drach, V.; Fricke, J. Temperature-Dependent Thermal Conductivity of Porous Silicon. *J. Phys. D* **1997**, 2911.
- (123) Putnam, S. A.; Cahill, D. G.; Ash, B. J.; Schadler, L. S. High-Precision Thermal Conductivity Measurements as a Probe of Polymer/Nanoparticle Interfaces. *J. Appl. Phys.* **2003**, 94 (10), 6785–6788. <https://doi.org/10.1063/1.1619202>.
- (124) Wang, X.; Ho, V.; Segalman, R. A.; Cahill, D. G. Thermal Conductivity of High-Modulus Polymer Fibers. *Macromolecules* **2013**, 46 (12), 4937–4943. <https://doi.org/10.1021/ma400612y>.
- (125) Hung, S. W.; Kikugawa, G.; Shiomi, J. Mechanism of Temperature Dependent Thermal Transport across the Interface between Self-Assembled Monolayer and Water. *J. Phys. Chem. C* **2016**, 120 (47), 26678–26685. <https://doi.org/10.1021/acs.jpcc.6b09516>.
- (126) Hori, R.; Wada, M. The Thermal Expansion of Wood Cellulose Crystals. *Cellulose* **2005**, 12 (5), 479–484. <https://doi.org/10.1007/s10570-005-5967-5>.
- (127) Atalla, R. H.; Vanderhart, D. L. Native Cellulose: A Composite of Two Distinct Crystalline Forms. *Science (80-.)*. **1984**, 223 (4633), 283–285. <https://doi.org/10.1126/science.223.4633.283>.
- (128) VanderHart, D. L.; Atalla, R. H. Studies of Microstructure in Native Celluloses Using Solid-State ¹³C NMR. *Macromolecules* **1984**, 17 (8), 1465–1472. <https://doi.org/10.1021/ma00138a009>.
- (129) Wada, M. Lateral Thermal Expansion of Cellulose I β and IIII Polymorphs. *J. Polym. Sci. Part B Polym. Phys.* **2002**, 40 (11), 1095–1102. <https://doi.org/10.1002/polb.10166>.
- (130) Zhou, S.; Nyholm, L.; Strømme, M.; Wang, Z. Cladophora Cellulose:

Unique Biopolymer Nanofibrils for Emerging Energy, Environmental, and Life Science Applications. *Acc. Chem. Res.* **2019**, *52* (8), 2232–2243. <https://doi.org/10.1021/acs.accounts.9b00215>.

- (131) Moon, R. J.; Martini, A.; Nairn, J.; Simonsen, J.; Youngblood, J. Cellulose Nanomaterials Review: Structure, Properties and Nanocomposites. *Chem. Soc. Rev.* **2011**, *40* (7), 3941–3994. <https://doi.org/10.1039/c0cs00108b>.
- (132) Nishiyama, Y.; Sugiyama, J.; Chanzy, H.; Langan, P. Crystal Structure and Hydrogen Bonding System in Cellulose I α from Synchrotron X-Ray and Neutron Fiber Diffraction. *J. Am. Chem. Soc.* **2003**, *125* (47), 14300–14306. <https://doi.org/10.1021/ja037055w>.
- (133) Nishiyama, Y.; Langan, P.; Chanzy, H. Crystal Structure and Hydrogen-Bonding System in Cellulose I β from Synchrotron X-Ray and Neutron Fiber Diffraction. *J. Am. Chem. Soc.* **2002**, *124* (31), 9074–9082. <https://doi.org/10.1021/ja0257319>.
- (134) Moon, R. J.; Martini, A.; Nairn, J.; Simonsen, J.; Youngblood, J. Cellulose Nanomaterials Review: Structure, Properties and Nanocomposites. *Chem. Soc. Rev.* **2011**, *40* (7), 3941. <https://doi.org/10.1039/c0cs00108b>.
- (135) Hori, R.; Wada, M. The Thermal Expansion of Cellulose II and IIIIcrystals. *Cellulose* **2006**, *13* (3), 281–290. <https://doi.org/10.1007/s10570-005-9038-8>.
- (136) Klemm, D.; Kramer, F.; Moritz, S.; Lindstr??m, T.; Ankerfors, M.; Gray, D.; Dorris, A.; Habibi, Y.; Lucia, L. a; Rojas, O. J. Cellulose Nanocrystals: Chemistry, Self-Assembly, and Applications. *Angew. Chemie - Int. Ed.* **2009**, *50* (24), 5438–5466. <https://doi.org/10.1021/cr900339w>.
- (137) Lee, C. M.; Kubicki, J. D.; Fan, B.; Zhong, L.; Jarvis, M. C.; Kim, S. H. Hydrogen-Bonding Network and OH Stretch Vibration of Cellulose: Comparison of Computational Modeling with Polarized IR and SFG Spectra. *J. Phys. Chem. B* **2015**, *119* (49), 15138–15149. <https://doi.org/10.1021/acs.jpcc.5b08015>.
- (138) Altaner, C. M.; Horikawa, Y.; Sugiyama, J.; Jarvis, M. C. Cellulose I β Investigated by IR-Spectroscopy at Low Temperatures. *Cellulose* **2014**, 3171–3179. <https://doi.org/10.1007/s10570-014-0360-x>.
- (139) Isogai, A. Wood Nanocelluloses: Fundamentals and Applications as New Bio-Based Nanomaterials. *J. Wood Sci.* **2013**, *59* (6), 449–459. <https://doi.org/10.1007/s10086-013-1365-z>.
- (140) Isogai, A.; Saito, T.; Fukuzumi, H. TEMPO-Oxidized Cellulose Nanofibers. *Nanoscale* **2011**, *3* (1), 71–85.

<https://doi.org/10.1039/c0nr00583e>.

- (141) Wågberg, L.; Winter, L.; Ödberg, L.; Lindström, T. On the Charge Stoichiometry upon Adsorption of a Cationic Polyelectrolyte on Cellulosic Materials. *Colloids and Surfaces* **1987**, 27 (1–3), 163–173. [https://doi.org/10.1016/0166-6622\(87\)80335-9](https://doi.org/10.1016/0166-6622(87)80335-9).
- (142) Reid, M. S.; Villalobos, M.; Cranston, E. D. Benchmarking Cellulose Nanocrystals: From the Laboratory to Industrial Production. **2017**. <https://doi.org/10.1021/acs.langmuir.6b03765>.
- (143) Tanaka, R.; Saito, T.; Hondo, H.; Isogai, A. Influence of Flexibility and Dimensions of Nanocelluloses on the Flow Properties of Their Aqueous Dispersions. *Biomacromolecules* **2015**, 16 (7), 2127–2131. <https://doi.org/10.1021/acs.biomac.5b00539>.
- (144) Schu, C.; Agthe, M.; Fall, A. B.; Gordeyeva, K.; Guccini, V.; Salajkova, M.; Plivelic, S.; Lagerwall, J. P. F.; Salazar-alvarez, G.; Bergstro, L. Rod Packing in Chiral Nematic Cellulose Nanocrystal Dispersions Studied by Small-Angle X - Ray Scattering and Laser Diffraction. **2015**. <https://doi.org/10.1021/acs.langmuir.5b00924>.
- (145) Diaz, J. A.; Ye, Z.; Wu, X.; Moore, A. L.; Moon, R. J.; Martini, A.; Boday, D. J.; Youngblood, J. P. Thermal Conductivity in Nanostructured Films: From Single Cellulose Nanocrystals to Bulk Films. *Biomacromolecules* **2014**, 15 (11), 4096–4101. <https://doi.org/10.1021/bm501131a>.
- (146) Li, D.; McGaughey, A. J. H. Phonon Dynamics at Surfaces and Interfaces and Its Implications in Energy Transport in Nanostructured Materials – An Opinion Paper. *Nanoscale Microscale Thermophys. Eng.* **2015**, 7265 (May), 150411043300009. <https://doi.org/10.1080/15567265.2015.1035199>.
- (147) Ota, A.; Ohnishi, M.; Oshima, H.; Shiga, T.; Kodama, T.; Shiomi, J. Enhancing Thermal Boundary Conductance of Graphite–Metal Interface by Triazine-Based Molecular Bonding. *ACS Appl. Mater. Interfaces* **2019**, 11, 37295–37301. <https://doi.org/10.1021/acsami.9b11951>.
- (148) Zhang, T.; Luo, T. Role of Chain Morphology and Stiffness in Thermal Conductivity of Amorphous Polymers. *J. Phys. Chem. B* **2016**, 120 (4), 803–812. <https://doi.org/10.1021/acs.jpcc.5b09955>.
- (149) Rashidi, V.; Coyle, E. J.; Sebeck, K.; Kieffer, J.; Pipe, K. P. Thermal Conductance in Cross-Linked Polymers: Effects of Non-Bonding Interactions. *J. Phys. Chem. B* **2017**, 121 (17), 4600–4609. <https://doi.org/10.1021/acs.jpcc.7b01377>.
- (150) Jain, A.; McGaughey, A. J. H. Strongly Anisotropic In-Plane Thermal

- Transport in Single-Layer Black Phosphorene. *Sci. Rep.* **2015**, *5*, 8501. <https://doi.org/10.1038/srep08501>.
- (151) Henry, A.; Chen, G.; Plimpton, S. J.; Thompson, A. 1D-to-3D Transition of Phonon Heat Conduction in Polyethylene Using Molecular Dynamics Simulations. *Phys. Rev. B - Condens. Matter Mater. Phys.* **2010**, *82* (14), 1–5. <https://doi.org/10.1103/PhysRevB.82.144308>.
- (152) Kulasinski, K. Effects of Water Adsorption in Hydrophilic Polymers. *Polym. Sci. Res. Adv. Pract. Appl. Educ. Asp.* **2016**, No. September, 217–223.
- (153) Suleiman, B. M.; Larfeldt, J.; Leckner, B.; Gustavsson, M. Thermal Conductivity and Diffusivity of Wood. *Wood Sci. Technol.* **1999**, *33* (6), 465–473. <https://doi.org/10.1007/s002260050130>.
- (154) Eitelberger, J.; Hofstetter, K. Prediction of Transport Properties of Wood below the Fiber Saturation Point - A Multiscale Homogenization Approach and Its Experimental Validation. Part I: Thermal Conductivity. *Compos. Sci. Technol.* **2011**, *71* (2), 134–144. <https://doi.org/10.1016/j.compscitech.2010.11.007>.
- (155) Diaz, J. A.; Ye, Z.; Wu, X.; Moore, A. L.; Moon, R. J.; Martini, A.; Boday, D. J.; Youngblood, J. P. Thermal Conductivity in Nanostructured Films: From Single Cellulose Nanocrystals to Bulk Films. *Biomacromolecules* **2014**, *15* (11), 4096–4101. <https://doi.org/10.1021/bm501131a>.
- (156) Uetani, K.; Okada, T.; Oyama, H. T. Crystallite Size Effect on Thermal Conductive Properties of Nonwoven Nanocellulose Sheets. *Biomacromolecules* **2015**, *16*, 2220–2227. <https://doi.org/10.1021/acs.biomac.5b00617>.
- (157) Shimazaki, Y.; Miyazaki, Y.; Takezawa, Y.; Nogi, M.; Abe, K.; Ifuku, S.; Yano, H. Excellent Thermal Conductivity of Transparent Cellulose Nanofiber/Epoxy Resin Nanocomposites. *Biomacromolecules* **2007**, *8* (9), 2976–2978. <https://doi.org/10.1021/bm7004998>.
- (158) Saito, T.; Isogai, A. TEMPO-Mediated Oxidation of Native Cellulose. The Effect of Oxidation Conditions on Chemical and Crystal Structures of the Water-Insoluble Fractions. *Biomacromolecules* **2004**, *5* (5), 1983–1989. <https://doi.org/10.1021/bm0497769>.
- (159) Saito, T.; Isogai, A. Introduction of Aldehyde Groups on Surfaces of Native Cellulose Fibers by TEMPO-Mediated Oxidation. *Colloids Surfaces A Physicochem. Eng. Asp.* **2006**, *289* (1–3), 219–225. <https://doi.org/10.1016/j.colsurfa.2006.04.038>.
- (160) Wågberg, L.; Decher, G.; Norgren, M.; Lindström, T.; Ankerfors, M.;

- Axnäs, K. The Build-up of Polyelectrolyte Multilayers of Microfibrillated Cellulose and Cationic Polyelectrolytes. *Langmuir* **2008**, *24* (3), 784–795. <https://doi.org/10.1021/la702481v>.
- (161) Kaldéus, T.; Larsson, P. T.; Boujemaoui, A.; Malmström, E. One-Pot Preparation of Bi-Functional Cellulose Nanofibrils. *Cellulose* **2018**, *25* (12), 7031–7042. <https://doi.org/10.1007/s10570-018-2066-y>.
- (162) Zhou, S.; Strømme, M.; Xu, C. Highly Transparent, Flexible, and Mechanically Strong Nanopapers of Cellulose Nanofibers @Metal–Organic Frameworks. *Chem. - A Eur. J.* **2019**, *25* (14), 3515–3520. <https://doi.org/10.1002/chem.201806417>.
- (163) Ocklind, A. Humidifier P-series <http://www.cellkraft.se/downloads/P-Series.pdf>.
- (164) Zhang, H.; Li, Y. M.; Tao, W. Q. Theoretical Accuracy of Anisotropic Thermal Conductivity Determined by Transient Plane Source Method. *Int. J. Heat Mass Transf.* **2017**, *108*, 1634–1644. <https://doi.org/10.1016/j.ijheatmasstransfer.2017.01.025>.
- (165) Trofimov, A. A.; Atchley, J.; Shrestha, S. S.; Desjarlais, A. O.; Wang, H. Evaluation of Measuring Thermal Conductivity of Isotropic and Anisotropic Thermally Insulating Materials by Transient Plane Source (Hot Disk) Technique. *J. Porous Mater.* **2020**, *27* (6), 1791–1800. <https://doi.org/10.1007/s10934-020-00956-3>.
- (166) Angayarkanni, S. A.; Sunny, V.; Philip, J. Effect of Nanoparticle Size, Morphology and Concentration on Specific Heat Capacity and Thermal Conductivity of Nanofluids. *J. Nanofluids* **2015**, *4* (3), 302–309. <https://doi.org/10.1166/jon.2015.1167>.
- (167) Qiu, L.; Zhu, N.; Feng, Y.; Michaelides, E. E.; Żyła, G.; Jing, D.; Zhang, X.; Norris, P. M.; Markides, C. N.; Mahian, O. A Review of Recent Advances in Thermophysical Properties at the Nanoscale: From Solid State to Colloids. *Phys. Rep.* **2020**, *843*, 1–81. <https://doi.org/10.1016/j.physrep.2019.12.001>.
- (168) ASTM International. Standard Test Methods for Water Vapor Transmission of Materials 1, 2002. <https://doi.org/10.1520/E0096>.
- (169) Bedane, A. H.; Eic, M.; Farmahini-Farahani, M.; Xiao, H. Theoretical Modeling of Water Vapor Transport in Cellulose-Based Materials. *Cellulose* **2016**, *23*, 1537–1552. <https://doi.org/10.1007/s10570-016-0917-y>.
- (170) Richter, J.; Stan, K. Measurements of Water Vapour Permeability – Tightness of Fibreglass Cups and Different Sealants and Comparison of μ -Value of Gypsum Plaster Boards. **2016**, *151*, 277–283. <https://doi.org/10.1016/j.proeng.2016.07.377>.

- (171) Brunauer, S.; Emmett, P. H.; Teller, E. Adsorption of Gases in Multimolecular Layers. *J. Am. Chem. Soc.* **1938**, *60* (2), 309–319. <https://doi.org/10.1021/ja01269a023>.
- (172) Barrett, E. P.; Joyner, L. G.; Halenda, P. P. The Determination of Pore Volume and Area Distributions in Porous Substances. I. Computations from Nitrogen Isotherms. *J. Am. Chem. Soc.* **1951**, *73* (1), 373–380. <https://doi.org/10.1021/ja01145a126>.
- (173) Rezakhanliha, R.; Agianniotis, A.; Schrauwen, J. T. C.; Griffa, A.; Sage, D.; Bouten, C. V. C.; Van De Vosse, F. N.; Unser, M.; Stergiopulos, N. Experimental Investigation of Collagen Waviness and Orientation in the Arterial Adventitia Using Confocal Laser Scanning Microscopy. *Biomech. Model. Mechanobiol.* **2012**, *11* (3–4), 461–473. <https://doi.org/10.1007/s10237-011-0325-z>.
- (174) Scandinavian pulp paper and board testing committee. *Total Acidic Group Content*; 2002; pp 1–4.
- (175) Beck, S.; Méthot, M.; Bouchard, J. General Procedure for Determining Cellulose Nanocrystal Sulfate Half-Ester Content by Conductometric Titration. *Cellulose* **2015**, *22* (1), 101–116. <https://doi.org/10.1007/s10570-014-0513-y>.
- (176) Varanasi, S.; He, R.; Batchelor, W. Estimation of Cellulose Nanofibre Aspect Ratio from Measurements of Fibre Suspension Gel Point. *Cellulose* **2013**, *20* (4), 1885–1896. <https://doi.org/10.1007/s10570-013-9972-9>.
- (177) Onyianta, A. J.; Williams, R. The Use of Sedimentation for the Estimation of Aspect Ratios of Charged Cellulose Nanofibrils. In *Advances in Natural Fibre Composites*; 2018; pp 195–203.
- (178) Segal, L.; Creely, J. J.; Martin, A. E.; Conrad, C. M. An Empirical Method for Estimating the Degree of Crystallinity of Native Cellulose Using the X-Ray Diffractometer. *Text. Res. J.* **1959**, *29* (10), 786–794. <https://doi.org/10.1177/004051755902901003>.
- (179) Sehaqui, H.; Ezekiel Mushi, N.; Morimune, S.; Salajkova, M.; Nishino, T.; Berglund, L. A. Cellulose Nanofiber Orientation in Nanopaper and Nanocomposites by Cold Drawing. *ACS Appl. Mater. Interfaces* **2012**, *4* (2), 1043–1049. <https://doi.org/10.1021/am2016766>.
- (180) Sehaqui, H. *Nanofiber Networks, Aerogels and Biocomposites Based on Nanofibrillated Cellulose from Wood*; 2011.
- (181) Balandin, A. A. Thermal Properties of Graphene and Nanostructured Carbon Materials. *Nat. Mater.* **2011**, *10* (8), 569–581. <https://doi.org/10.1038/nmat3064>.

- (182) Luo, T.; Lloyd, J. R. Enhancement of Thermal Energy Transport across Graphene/Graphite and Polymer Interfaces: A Molecular Dynamics Study. *Adv. Funct. Mater.* **2012**, *22* (12), 2495–2502. <https://doi.org/10.1002/adfm.201103048>.
- (183) Deville, S. Freeze-Casting of Porous Biomaterials: Structure, Properties and Opportunities. *Materials (Basel)*. **2010**, *3* (3), 1913–1927. <https://doi.org/10.3390/ma3031913>.
- (184) Deville, S. The Lure of Ice-Templating Recent Trends and Opportunities for Porous Materials. *Scr. Mater.* **2018**, *147*, 119–124.
- (185) Li, C.; Shi, G. Three-Dimensional Graphene Architectures. *Nanoscale* **2012**, *4* (18), 5549. <https://doi.org/10.1039/c2nr31467c>.
- (186) Anderson, A. M.; Worster, M. G. Periodic Ice Banding in Freezing Colloidal Dispersions. *Langmuir* **2012**, *28* (48), 16512–16523. <https://doi.org/10.1021/la303458m>.
- (187) Kulasinski, K.; Guyer, R.; Derome, D.; Carmeliet, J. Water Adsorption in Wood Microfibril-Hemicellulose System: Role of the Crystalline-Amorphous Interface. *Biomacromolecules* **2015**, *16* (9), 2972–2978. <https://doi.org/10.1021/acs.biomac.5b00878>.
- (188) Ochs, F.; Heidemann, W.; Müller-Steinhagen, H. Effective Thermal Conductivity of Moistened Insulation Materials as a Function of Temperature. *Int. J. Heat Mass Transf.* **2008**, *51* (3–4), 539–552. <https://doi.org/10.1016/j.ijheatmasstransfer.2007.05.005>.
- (189) Algaer, E. Thermal Conductivity of Polymer Materials Reverse Nonequilibrium Molecular Dynamics Simulation, Technische Universität Darmstadt, 2010.
- (190) Künzel, H. M.; Kiessl, K. Calculation of Heat and Moisture Transfer in Exposed Building Components. *International Journal of Heat and Mass Transfer*. 1996, pp 159–167. [https://doi.org/10.1016/S0017-9310\(96\)00084-1](https://doi.org/10.1016/S0017-9310(96)00084-1).
- (191) Hansen, M. H. Estimation of Transfer Coefficients in Models for Coupled Heat and Moisture Transfer in Porous Media, Building Materials Laboratory, Technical University of Denmark, Lyngby, 1993.
- (192) Belbekhouche, S.; Bras, J.; Siqueira, G.; Chappey, C.; Lebrun, L.; Khelifi, B.; Marais, S.; Dufresne, A. Water Sorption Behavior and Gas Barrier Properties of Cellulose Whiskers and Microfibrils Films. *Carbohydr. Polym.* **2011**, *83* (4), 1740–1748. <https://doi.org/10.1016/j.carbpol.2010.10.036>.
- (193) Aguirre-loredo, R. Y.; Rodriguez-hernandez, A. I.; Velazquez, G. Modelling the Effect of Temperature on the Water Sorption Isotherms

- of Chitosan Films. *Food Sci. Technol* **2017**, *37* (1), 112–118.
<https://doi.org/DOI:10.1590/1678-457X.09416>.
- (194) Al-Muhtaseb, A. H.; McMinn, W. A. M.; Magee, T. R. A. Water Sorption Isotherms of Starch Powders: Part 1: Mathematical Description of Experimental Data. *J. Food Eng.* **2004**, *61* (3), 297–307. [https://doi.org/10.1016/S0260-8774\(03\)00133-X](https://doi.org/10.1016/S0260-8774(03)00133-X).
- (195) Wang, N. Moisture Sorption Isotherm Characteristics of Potatoes at Four Temperatures. **1991**, *14*, 269–287.
- (196) Zhang, R.; Chen, Q.; Zhen, Z.; Jiang, X.; Zhong, M.; Zhu, H. Cellulose-Templated Graphene Monoliths with Anisotropic Mechanical, Thermal, and Electrical Properties. *ACS Appl. Mater. Interfaces* **2015**, *7* (34), 19145–19152. <https://doi.org/10.1021/acsami.5b04808>.